Dóra Papp

# Variational determination of resonance states of weakly-bound molecular complexes

PhD Thesis

**Supervisors:**

Prof. Dr. Attila G. Császár, DSc
Professor of Chemistry, Eötvös Loránd University

Dr. Tamás Szidarovszky, PhD
Research Associate, Eötvös Loránd University

**Chemistry Doctoral School**
Head of Doctoral School: Prof. Dr. Attila G. Császár

**Theoretical and Physical Chemistry, Structural Chemistry**
Head of Doctoral Program: Prof. Dr. Péter R. Surján

Eötvös Loránd University
Budapest, 2017

# Contents

# Chapter 1

# Introduction

During the course of my PhD research I have developed and applied computational nuclear motion tools which make possible the variational determination of rovibrational resonance sates of polyatomic molecules. Resonance, or quasi-bound, states of a molecule are metastable states that have energy higher than the dissociation limit, therefore the molecule can break up into subsystems, resulting in finite lifetimes of these states.[1] Resonance states play an important role in molecular spectroscopy[2–6] and scattering processes,[7–12] and they often mediate complex chemical reactions.[13–17] Their experimental and theoretical investigation has been a hot topic in recent years;[3–18] however, only scattering theory could offer computational techniques to determine resonance states of molecules containing more than three atoms.[6;10–12] In contrast to the indirect techniques of scattering computations, variational determination of resonances results directly in their energies and lifetimes.

During my PhD years I have developed a general variational code,[19] which is capable of computing resonance energies and lifetimes, along with the visualization of the resonance wave functions, without any constraint regarding the number of atoms in the given molecule. The newly-developed code, named GENIUSH-CAP, utilizes the bound states obtained from GENIUSH,[20;21] a general rovibrational bound-state computing program developed previously in our group, this way exploiting all the advantages of GENIUSH. I have successfully applied GENIUSH-CAP and studied the resonance states of three weakly-bound systems: $Ar{\cdot}NO^+$,[22] $H_2He^+$,[19;23] and $H_2{\cdot}CO$,[19]

$H_2$·CO being the first four-atomic complex subjected to non-Hermitian variational resonance computation. With the help of GENIUSH-CAP, the detailed comprehensive analysis of these systems has been carried out, providing valuable information about the nature of their resonance states.

As an additional project, during the time of my PhD work I was also working on the theoretical characterization of the four possible types of ion-aromatic ring interactions, of wide biochemical interest, using sophisticated electronic structure methods. However, this research does not form part of this thesis, in order to preserve the thesis's uniformity. Interested readers of this thesis are asked to read the corresponding scientific paper.[24]

In what follows, first, I give a brief introduction to the theory of nuclear motions, particularly to the variational techniques used for determining rovibrational bound and resonance states of molecules. After this, the details of the method development I have carried out are presented, followed by the application of the new code to the weakly-bound complexes Ar·$NO^+$, $H_2He^+$, and $H_2$·CO. Finally, a summary of the thesis and my PhD work along with the main conclusions is given.

# Chapter 2

# Nuclear motion theory

## 2.1 Theoretical background

### 2.1.1 General aspects

Quantum chemistry is defined as the application of quantum mechanics to problems of chemical interest. It has two major branches, electronic structure theory and nuclear motion theory. This separation is possible due to the Born–Oppenheimer approximation,[25] which states that, since the mass of the electrons is at least three orders of magnitude smaller than that of the nuclei, the faster motion of the electrons can be separated from the much slower motion of the nuclei. Thus, the electrons move in the field of steady nuclei, and nuclei see an average distribution of the electrons. This approximation provides the concept of the potential energy surface (PES), which can be obtained by solving the Schrödinger equation of electronic motion at many different configurations of the nuclei, and fitting a functional form to these computed energy points. The PES obtained governs the motion of the nuclei. Using this procedure other so-called property surfaces, such as dipole moment surfaces, can be obtained, as well.

The time-dependent Schrödinger equation (TDSE), the fundamental equation of non-relativistic quantum mechanics, describes the behavior of a quantum system over

time. However, in many applications only stationary solutions are sought, which can be obtained by solving the time-independent Schrödinger equation (TISE) after separating the time and space variables of TDSE. In most of the electronic structure problems, only the lowest stationary states are of interest, since in general only a few excited electronic states of a system play a role in chemical processes. In contrast, in nuclear motion theory many rotational-vibrational-electronic (rovibronic) stationary states should be determined, *e.g.* to decipher infrared or microwave molecular spectra. Nevertheless, several chemical problems of wide interest are also addressed through the time-dependent approach, such as strong field interactions[26–30] or reactive scattering.[31–34]

In nuclear motion theory stationary states can be viewed from two basically different aspects. Spectroscopy treats these states as eigenstates of the system's Hamiltonian supported by the given PES. The simplest form of such a PES is a quadratic surface, which is assumed in the framework of the harmonic oscillator model (detailed below). However, real molecules feature anharmonic PESs and one or more dissociation asymptotes. Another way to think of stationary states of a molecule in motion is the dynamical point of view of scattering theory, which primarily characterizes stationary states by their asymptotic behavior. Even without taking time dependence into account, based only on propagation in space, the approach considering two colliding moieties can yield stationary states of weakly-bound complexes if suitable boundary conditions are imposed for the coupled differential equations of scattering theory. This approach, however, does not work well for strongly bound systems, where the potential well is surrounded by steep barriers. Nevertheless, in the case of "intermediate" systems featuring a shallow potential well along one dissociation channel, both of the above approaches can provide accurate solutions. Weakly-bound van der Waals complexes fit perfectly into this category and can be studied by both time-independent scattering and spectroscopic methods, as it will be shown later in this thesis. Several methods of time-dependent quantum dynamics[35–38] have also been developed and are widely used for investigating molecular motions; however, these are out of the scope of this thesis.

Analytic solution of the TISE of real atoms, ions, and molecules without any approximation can only be obtained for the H-atom, whereas highly accurate numerical

solutions were provided for a few other systems: He,[39] $H_2^+$,[39;40] $H_2$,[41] $HeH^+$,[42] $H_3^+$,[43] and their isotopologues. Thus, introducing approximations is essential for studying even few-atomic chemically interesting systems. Besides the above outlined cornerstone of quantum chemistry, the Born–Oppenheimer approximation, other approximations should also be applied to solve the TISE for both the electronic and the nuclear motions.

Regarding the internal motions of a molecule, *i.e.*, its vibrations and rotations, two simple models have been emerged from the very beginning for the interpretation of molecular spectra. One is the harmonic oscillator (HO) approximation, where an $N$-atomic nonlinear(linear) molecule is considered as a multidimensional harmonic oscillator, leading to the decoupled problem of $3N-6(3N-5)$ individual oscillators, with the 3(2) rotational and the 3 translational degrees of freedom separated and the $3N-6(3N-5)$ normal coordinates introduced. Along the normal coordinates the atoms of the molecule vibrate harmonically, *i.e.*, with the same frequency and the same phase, but with different amplitudes. These vibrations are called normal vibrations. Normal coordinates can be obtained by applying a unitary transformation on mass-weighted Cartesian atomic displacement coordinates so that the transformation matrix contains the eigenvectors of the mass-weighted Hesse matrix. The other basic model concerns rotations and is called the rigid rotor (RR) approximation. Within the RR model, since molecular rotations are much slower than vibrations, the molecule is treated as a rigid body during rotation, with the rigid structure corresponding to a vibrationally averaged geometry of the molecule.

However, the vibrations of a real molecule are far from being harmonic. Thus, more accurate models had to be developed to investigate molecular motions. Within the above sketched "static" approach involving the determination of the eigenstates of the system's Hamiltonian, two basic paths have been paved: variational or perturbation theories. The essence of the former is that the energy levels of a system are searched by means of the variational principle, which states that they are equal to the exact energy only in the case of using the exact wave functions corresponding to the chosen Hamiltonian; otherwise, the calculated energy values are upper bounds to the real (exact) ones. The perturbative approach is based on the assumption that the system of interest is only slightly different from an already known one, for which the solutions of

the TISE are available; thus, the energy levels of the perturbed system can be obtained by adding a correction term to the Hamiltonian of the known system. Increasing the orders of the perturbation can be considered, which provide more and more accurate energy levels, if the series of correction terms converges. In contrast to the variational method, this procedure does not necessarily provide an upper bound to the energy levels when the order of the perturbation is increased.

Perturbation-based methods are of course available to determine rovibrational bound energy levels; however, they provide results only of limited accuracy. The most popular of them is the method of vibrational perturbation theory carried out to second order (VPT2).[44;45] This method employs quartic force fields and normal coordinates. Nevertheless, if one wants to determine first-principles (rotational-)vibrational energy levels of molecules with high accuracy, the use of methods based on the variational principle becomes necessary.

During my PhD research I have developed and employed tools of variational nuclear motion theory, in order to determine resonance, or quasi-bound, states of polyatomic systems, located above the first dissociation threshold. In the framework of the technique I worked with the computation of all the bound eigenstates of the system is necessary. Therefore, in the forthcoming sections the fundamentals of the variational determination of rovibrational bound and resonance states will be presented, along with a brief introduction to close-coupling scattering theory, since its results had been compared to my variational ones.

### 2.1.2 Variational nuclear motion computations

The basic idea behind the variational determination of energy levels is the expansion of the exact wave function ($\psi$) in a suitable basis set $\{\phi_i\}$:

$$\psi \cong \sum_{i}^{N} c_i \phi_i, \tag{2.1}$$

where $c_i$ are linear combination coefficients. Then, the TISE,

$$\hat{H}\psi = (\hat{K} + \hat{V})\psi = E\psi, \tag{2.2}$$

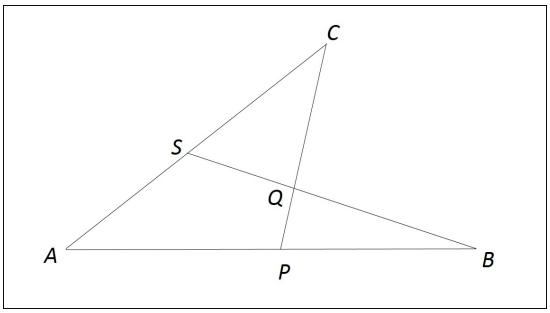


Figure 2.1: Generalized internal coordinates of the three-particle systems proposed by Sutcliffe and Tennyson,[46] with $A$, $B$, and $C$ denoting the particles. $S$, $P$, and $Q$ are defined in the text, below Eq. 2.4.

where $\hat{H}$ denotes the Hamiltonian of the system, $\hat{K}$ and $\hat{V}$ are the kinetic and the potential energy operators, respectively, $\psi$ is the exact wave function, and $E$ is the exact energy, results in the following matrix equation (assuming that $\phi_i$ form an orthonormal set):

$$\mathbf{Hc} = E\mathbf{c}, \quad \text{where} \quad H_{ij} = \langle \phi_i | \, \hat{H} \, | \phi_j \rangle \tag{2.3}$$

In order to apply variational nuclear motion theory to a rotating and vibrating molecular system, tho following should be considered: (1) the choice of the most suitable coordinate system for describing the nuclear motions, (2) building the kinetic energy operator in the chosen coordinate system, (3) determination of the PES, (4) the optimal choice of the basis set in which the rovibrational wave functions are expanded, (5) the method of evaluating the matrix elements of the **H** Hamilton matrix in the chosen basis set, and (6) the diagonalization of **H** to obtain the required eigenpairs.

To treat the vibrational problem, it is usual to employ internal coordinates, whereby, after the exact separation of the three translational degrees of freedom, the vibrational motion can be described by $3N$–6(5) coordinates in the case of an $N$-atomic nonlinear(linear) molecule. If the rotational motion is not separated, a body-fixed frame has to be attached to the molecule. As rotational coordinates, usually the three so-called Euler angles[47] are applied, describing the orientation of the body-fixed frame with respect to the laboratory-fixed frame. The internal coordinate system is always chosen to properly describe the vibrational motions of the system, and for this, chemical intuition is often necessary. A frequently used coordinate system for triatomic molecules and complexes are the orthogonal Jacobi coordinates,[48] which can be derived from the general coordinate system of triatomic molecules, proposed by Sutcliffe

and Tennyson,[46] sketched in Figure 2.1. The Jacobi coordinate system forms, when

$$g_1 = \frac{m_B}{m_A + m_B} \quad \text{and} \quad g_2 = 0, \tag{2.4}$$

where, $m_A$ and $m_B$ are the masses of the particles $A$ and $B$, respectively, $g_1 = (A - P)/(A - B)$ and $g_2 = (A - S)/(A - C)$. The definition of Jacobi coordinates is $r = B - S$, $R = C - P$, and $\theta = BQC$. The Jacobi coordinate system can also be generalized to more than three atoms. Other coordinate systems for triatomics can be derived from the Sutcliffe–Tennyson coordinates, as well, such as the orthogonal Radau,[49] or the non-orthogonal valence bond coordinates. Further internal coordinate systems, based on chemical intuition, can also be applied for the vibrational problem, *e.g.*, normal coordinates.

The kinetic energy operator $\hat{T}$ of the system then should be expressed in terms of the chosen coordinates. This can be easily done in Cartesian coordinates; however, in internal coordinates $\hat{T}$ usually has a rather complicated form. Derivation of the exact kinetic energy operators in terms of various coordinates for several types of systems is often a research project in itself, for which many examples can be found in the literature.[46;50–53]

The potential energy operator of a molecule cannot be given exactly, the PES is represented by an analytic function fitted to electronic energy points computed at many different nuclear configurations. Since the converged variational results of the nuclear motion problem are the numerically "exact" solutions corresponding to the given PES, the accuracy of the PES has a major effect on the accuracy of the computed rovibrational energy levels. Similarly to the derivation of kinetic energy operators, developing a PES often forms a distinct research topic.

As expressed in Eq. (2.1), a basis set is used to expand the exact vibrational wave function. If the problem is multidimensional, a multidimensional basis should be employed, which can be a direct product of one-dimensional basis functions, or a non-direct-product basis, *e.g.* when coupled one-dimensional functions are considered. In vibrational problems, usually orthogonal polynomials (with appropriate damping functions assuring square integrability) are chosen as basis functions, such as Legendre,

Laguerre, or Hermite polynomials. For rotations, usually the rigid rotor eigenfunctions of the symmetric top or their symmetry adapted versions are employed.

The next challenging task is to determine the matrix elements of the Hamiltonian in the chosen basis, see Eq. (2.3). For this, there are various options. For example, the variational basis representation (VBR) might be used, which determines all the integrals defining the matrix elements analytically. In the finite basis representation (FBR) these integrals are not exact, but are calculated numerically, *e.g.*, employing the Gaussian-quadrature technique.[54] Grid techniques are also frequently employed in nuclear motion theory, a particularly favored technique is the discrete variable representation (DVR).[55–58] To apply DVR, one possible choice is to take an orthonormal basis set, usually orthogonal polynomials, and build the ($\mathbf{Q}$) coordinate matrix in this basis. Then, the diagonalization of this matrix, by solving

$$\mathbf{QT} = \mathbf{Tq} \tag{2.5}$$

provides the so-called transformation matrix, $\mathbf{T}$, and the diagonal $\mathbf{q}$ matrix containing the quadrature points, which are the roots of the $n^{th}$ polynomial in the case of using $n$ standard orthogonal polynomials indexed as $0, 1, 2, ..., n-1$. By transforming the kinetic and the potential energy matrices, built in FBR, with the transformation matrix, one obtains the DVR of the Hamiltonian:

$$\mathbf{H}^{\mathrm{DVR}} = \mathbf{T}^{\mathrm{T}}\mathbf{K}^{\mathrm{FBR}}\mathbf{T} + \mathbf{V}^{\mathrm{diag}}, \tag{2.6}$$

A major advantage of using DVR is that in DVR the matrix of the potential energy operator, or that of any operator depending only on the coordinates, can be approximated to be diagonal.[55] This is an essential feature of DVR, because it makes it possible to apply arbitrary forms of potential energy functions. It can be proven,[56] since the eigenvalues of $\mathbf{Q}$ are the Gaussian quadrature points, that the eigenvalues of the Hamilton matrix are the same as if they are determined with the Guassian-quadrature method in FBR; whereas the eigenvectors in DVR are the unitary transforms of the ones obtained in FBR. It has been shown that the above described, so-called transformation method gives matrix elements of Gaussian quadrature accuracy even in the case of general bases.[59]

The final step of a variational method is the computation of the requested eigenvalues and eigenfunctions of the Hamilton matrix. This can be done by different methods. Direct diagonalization techniques can be used if the computation of all the eigenvalues is possible and desirable. Two disadvantages of these techniques are that the elements of the Hamilton matrix have to be stored, which could require a considerable amount of memory and that the computational cost of direct diagonalization methods increase rapidly with the increasing dimension of the Hamilton matrix. Thus, for the diagonalization of rovibrational Hamilton matrices, often having extremely large dimensions, such direct methods cannot be applied. However, since we do not need to compute all the eigenvalues of these matrices, iterative diagonalization methods can be applied efficiently. These techniques require the evaluation of a limited number of matrix-vector products; thus, they have lower computational cost. In rovibrational computations the Lanczos iterative eigensolver[60] is the most widely used method, which is capable of computing thousands of eigenpairs efficiently. If only a few eigenpairs need to be determined, the Davidson algorithm,[61] widely employed in electronic structure theory, can be applied.

Eigenvalues and eigenstates of a rotating-vibrating molecule cannot only be determined variationally below the first dissociation threshold, but even (high) above this energy. For this, several procedures have been developed, their introduction will be the subject of the following sections. Nonetheless, before that let us take a brief detour towards scattering theory.

### 2.1.3 Close-coupling scattering theory

One way to treat the problem of two colliding "particles", *e.g.*, an atom scattered on a molecule, or the collision of two small molecules, is to solve the so-called close-coupled equations of scattering theory.[62–66] This technique, being somewhat off-topic from the methods used in the present thesis, is introduced because some of my results are compared to those obtained from close-coupling computations.

In the close-coupling procedure the scattering wave function is expanded in a complete set of internal states of the system, usually constructed as direct products of

the internal states of one (or both) fragments, multiplied by angular functions which describe the rotation of one collision partner with respect to the other. The internal states are called channels, referring to the possible starting points and outcomes of the scattering process. Substitution of the expanded wave function into the TISE results in a set of coupled ordinary differential equations. These equations are solved by propagation along the intermolecular distance, which can be the $R$ Jacobi coordinate in an atom-diatom scattering process, starting from small $R$ values at the interaction region of the potential to values of $R$ so large that the potential becomes negligible. This has to be done at many values of the $J$ quantum number characterizing the total angular momentum of the system, until the centrifugal potential keeps the colliding particles beyond the range of the interaction potential. The solution yields the so-called scattering matrix, from which differential and integral cross sections can be computed at all values of $J$. State-to-state cross sections, corresponding to given initial and final states, can also be obtained from the scattering matrix.

## 2.2 Variational determination of rovibrational bound states

### 2.2.1 Different protocols

Based on the previously outlined pivots of the variational determination of rovibrational bound states of a system, various types of concrete computational algorithms can be derived. Indeed, many different variational nuclear motion algorithms and corresponding computer codes have been developed in the past few decades. In contrast to the softwares available for electronic structure computations, nuclear motion codes are much less black-box type. Since the kinetic energy operator should be expressed in different sets of internal coordinates for each system studied and basis functions should also be adapted to the various types of internal coordinates, traditionally variational nuclear motion codes have been constructed specifically for the chosen systems and coordinates.

There are two major groups of variational nuclear motion codes: the first involves programs based on rectilinear coordinates, while the members of the other group use curvilinear internal coordinates. The second group is much more suitable for describing large-amplitude motions, and therefore only such codes are employed in the case of weakly-bound, flexible molecules or complexes.

Representatives of the first branch are as follows: the MULTIMODE code, developed by Carter and co-workers,[67] and the DEWE code developed in our group.[68] Both codes use Eckart–Watson-type Hamiltonians expressed in normal coordinates. MULTIMODE employs a FBR of the rovibrational Hamiltonian, and approximates the PES in a so-called $N$-mode representation. In contrast, DEWE uses the DVR technique to represent the vibrational Hamiltonian and hence the PES can be invoked without approximations. Both codes are general in a sense that they can be applied, in principle, without any constraint regarding the number of atoms; however, they cannot efficiently treat floppy molecules and those having a PES with multiple minima.

Several variational rovibrational codes employing curvilinear coordinates for describing the molecular vibrations, mainly those having large amplitudes, have been developed. Many of these use tailor-made Hamiltonians, *i.e.*, Hamiltonians expressed analytically in a given internal coordinate system, such Jacobi or Radau coordinates. Triatomic codes of this kind are DVR3D, developed by Tennyson and co-workers,[69;70] and DOPI[71] or D$^2$FOPI[72] from our group. Similar codes for molecules containing more than three atoms are also available.[73–77]

Since results obtained with the D$^2$FOPI program will be presented later in this thesis, let us briefly outline the important features of this code. It employs the Sutcliffe–Tennyson Hamiltonian in orthogonal curvilinear internal coordinates, (Figure 2.1). It uses DVR in case of the radial coordinates, and FBR for the angular coordinate. (Unlike DOPI, which uses DVR for all three coordinates.) The Hamiltonian is represented in a direct product basis for the vibrational problem; however, when molecular rotations are present, associated Legendre polynomials are used on the vibrational angular coordinate, which are coupled to the symmetric rigid rotor eigenfunctions describing the rotational motion. The eigenpairs of the resulting Hamilton matrix are computed employing a Lanczos iterative eigensolver.

A general protocol to determine accurate rovibrational energy levels of floppy molecules would allow to choose arbitrary coordinate systems, *i.e.*, the most appropriate ones to represent the vibrational motions of the molecule of interest. Several attempts have been made to develop such codes, *e.g.* by Luckhaus and co-workers,[78–81] Lauvergnat et al.,[82;83] Yurchenko et al.,[84] and Makarewicz.[85] It is obvious that only this class of nuclear motion codes can possibly be developed into black-box-type programs, similar to the highly successful electronic structure codes. In the following section, a general algorithm of this type will be introduced, which I employed during my rovibrational bound-state computations. It is named GENIUSH and was developed in our group.[20;21].

### 2.2.2 GENIUSH

GENIUSH[20;21;86] is a general (GE) protocol to determine rovibrational states by numerically (N) representing the kinetic energy operator of the system in internal coordinates (I), and using an iterative Lanczos eigensolver to determine the eigenpairs of the user-specified Hamiltonian (USH). This code does not involve any explicit constraints regarding the number of atoms in the molecule.

In GENIUSH the rovibrational Hamiltonian $\hat{H}^{\mathrm{rv}}$ of an $N$-atomic molecule, after the separation of the translational motion, is represented by the following formula, the so-called Podolsky form,[87] where $D \leq 3N-6$ coordinates describe the vibrational motions of the system:

$$\hat{H}^{\mathrm{rv}} = \frac{1}{2} \sum_{k,l=1}^{D+3} \tilde{g}^{-1/4} \hat{p}_k G_{kl} \tilde{g}^{1/2} \hat{p}_l \tilde{g}^{-1/4} + \hat{V}, \tag{2.7}$$

where $\hat{V}$ is the potential energy operator, $\tilde{g} = \det \mathbf{g}$, $\mathbf{G} = \mathbf{g}^{-1}$ and $\mathbf{g}$ is the rotational-vibrational metric tensor

$$g_{kl} = \sum_{i=1}^{N} m_i \frac{\partial \mathbf{X}_i^{\mathrm{T}}}{\partial q_k} \frac{\partial \mathbf{X}_i}{\partial q_l}, \quad k,l = 1,2,\ldots,D+3, \tag{2.8}$$

$m_i$ are the atomic masses, $\mathbf{X}_i$ refers to the $3N-3$ rectilinear laboratory-fixed Cartesian coordinates (the translational motion is separated), and $q_k$ denotes the $D$ internal

coordinates. The body-fixed Cartesian coordinates of the $i^{th}$ nucleus, $x_{ia}$, can be derived from $X_{i\mathrm{a}}$ using

$$X_{i\mathrm{a}} = \sum_{a} C_{\mathrm{a}a} x_{ia}, \tag{2.9}$$

where $\mathrm{a} = \mathrm{X}, \mathrm{Y}, \mathrm{Z}$ the axes of the laboratory-fixed frame, $a = x, y, z$ are those of the body-fixed frame and $C_{\mathrm{a}a}$ is the orthogonal direction cosine matrix between the laboratory-fixed and the body-fixed frames.

The momentum, $\hat{p}_k$, conjugate to $\hat{q}_k$, has the form

$$\hat{p}_k = -\mathrm{i}\hbar \frac{\partial}{\partial q_k}, \quad k = 1, 2, \ldots, D, \quad \text{and} \tag{2.10}$$

$$\hat{p}_{D+1} = \hat{J}_x = -\mathrm{i}\hbar \frac{\partial}{\partial \alpha}, \quad \hat{p}_{D+2} = \hat{J}_y = -\mathrm{i}\hbar \frac{\partial}{\partial \beta}, \quad \hat{p}_{D+3} = \hat{J}_z = -\mathrm{i}\hbar \frac{\partial}{\partial \gamma}, \tag{2.11}$$

where i is the imaginary unit, $\hat{J}_a$ with $a = x, y, z$ are related to the projection of the total angular momentum operator, $\hat{J}$, on axis $a$ of the body-fixed frame, and $\alpha, \beta$, and $\gamma$ denote the angles characterizing the instantaneous orientation of the body-fixed frame with respect to the laboratory-fixed frame, thereby describing the rotation of the molecule.

For the numerical construction of the kinetic energy operator the so-called **t**-vector formalism is employed, which requires the computation of the first derivatives of the body-fixed Cartesian coordinates in terms of the internal coordinates, $\partial x_{ia}/\partial q_k$. The **t**-vectors are constructed as[20;21]

$$t_{iak} = \frac{\partial x_{ia}}{\partial q_k}, \quad k = 1, 2, \ldots, D, \quad \text{and} \tag{2.12}$$

$$t_{iaj+D} = (\mathbf{e}_j \times \mathbf{x}_i)_a, \qquad j = 1(x), 2(y), 3(z), \tag{2.13}$$

where $\mathbf{e}_j$ denotes the unit vector pointing along the $j^{th}$ axis of the body-fixed frame and $\mathbf{x}_i$ refers to the body-fixed Cartesian coordinates of the $i^{th}$ nucleus. Elements of the **g** matrix can then be given in terms of the **t**-vectors as follows:

$$g_{kl} = \sum_{i=1}^{N} m_i \sum_{a} t_{iak} t_{ial} = \sum_{i=1}^{N} m_i \mathbf{t}_{ik}^{\mathrm{T}} \mathbf{t}_{il}. \tag{2.14}$$

The rotational-vibrational coupling elements of the $\mathbf{g}$ matrix can be given as

$$g_{k,j+D} = \sum_{i=1}^{N} m_i \frac{\partial \mathbf{x}_i^{\mathrm{T}}}{\partial q_k} (\mathbf{e}_j \times \mathbf{x}_i), \quad \text{where} \quad k = 1, 2, .., D, \text{ and } j = 1, 2, 3. \tag{2.15}$$

Reduced-dimensional models can be straightforwardly introduced by constraining some of the internal coordinates to a constant, usually their equilibrium values. This means that the corresponding rows and columns of the $\mathbf{g}$ matrix vanish. In order to get energy levels independent of the chosen coordinate system one must introduce the constraints for the internal coordinates before inverting the $\mathbf{g}$ matrix, thereby fixing them "physically", instead of reducing the $\mathbf{G}$ matrix, which would refer to constraints for the momenta. For the case of reduced-dimensional models I have made it possible in GENIUSH to carry out the relaxation of the PES, *i.e.*, finding the optimal value of the inactive coordinate(s) corresponding to the lowest potential energy, while the other (otherwise active) coordinates are held frozen. This feature is available for one- and two-dimensional constraints.

To represent the Hamiltonian of the system of interest, DVR is used, employing orthogonal polynomials, such as Laguerre, Hermite or Legendre polynomials or Fourier-DVR basis functions, *e.g.*, for torsional motions. Due to the use of DVR, every quantity in the Hamiltonian operator depending only on the coordinates, most importantly the PES, is represented by a diagonal matrix. As rotational basis, the $2J+1$ orthonormal Wang-functions[47] are used, which are the symmetrized versions of the symmetric-top rigid rotor eigenfunctions.

Finally, to obtain numerous eigenpairs of the rovibrational Hamiltonian, an effective Lanczos iterative eigensolver is used. It is developed so that the explicit construction of the Hamilton matrix built in the large direct-product basis is avoided.

## 2.3 Introduction to resonance states

### 2.3.1 The resonance phenomenon

Resonance, or quasi-bound, states are defined as metastable states of a system that has sufficient energy to break up into its subsystems.[1] However, the resonance phenomenon can also be approached from the dynamical point of view indicated in Section 2.1. Within this approach resonance states can be defined as states of a target-particle system having lifetimes longer than that of a direct collision process.[1] In this case resonances can be observed as a sudden increase in the collisional cross Section occurring at a certain energy. A characteristic feature of resonance states is that they decay exponentially in time. Theory of resonances was first derived by Gamow in 1928 concerning the case of the $\alpha$-decay of heavy nuclei.[88]

Besides their prominent role in spectroscopy[2–6] and scattering processes,[7–12] resonances are also closely related to reaction dynamics. They are essential in mediating complex chemical reactions,[13–17] and are also of importance for unimolecular reactions[89–91] as well as in photodissociation processes.[29;92;93] It has recently been shown that monitoring a quantum scattering resonance in an ionization reaction allows for quantifying the anisotropy of an atom-molecule collision.[18]

In molecular physics, usually two types of resonances are distinguished. One type occurs *e.g.* when a particle is temporarily trapped by a potential barrier, and its decay rate is determined by the shape of this potential and the mass of the particle.[1] These resonance states are called shape-type resonances. In such a case, the lifetime of the resonance state is defined by the height and width of the barrier. Occurrence of a shape resonance is a purely quantum mechanical phenomenon, *e.g.* it is based on tunneling through the potential barrier. A simple example is when the potential barrier appears due to the rotational excitation of the molecule. Another example for a shape resonance is radioactive decay.

The other, so-called Feshbach-type resonances usually occur for many-particle systems (or for a single particle in a more-than-one-dimensional potential).[1] A Feshbach-

type resonance can be described as a bound state of an unperturbed Hamiltonian, embedded in its continuum, which becomes metastable due to the coupling (perturbation) with the continuum.[1] (Such a state resembles a bound state, because it is localized in the interaction region of the potential.) In other words, for such a resonance the excess energy is stored in a non-dissociative degree of freedom. If the subsystems are divided, that is when dissociation occurs, the coupling potential vanishes. Within the scattering approach such a resonance state can be treated as a bound state of a closed channel of the many-particle scattering target, which becomes open due to the coupling with the scattered particle/system. Examples of Feshbach-type resonances are those occurring during autoionization following photo-excitation.[1;94]

Overall, resonances play an important role in molecular spectroscopy and in scattering phenomena, as well as in the dynamics of chemical reactions. They can be observed in several cases via spectroscopic means;[2–6] however, the experimental work need to be augmented with theoretical interpretations and predictions. During the past decades various methods have been developed to determine resonance states, both within the time-dependent[17;95] and in the time-independent[5;96–98] framework of quantum mechanics. Some of the time-independent methods will be presented in what follows, after introducing resonance states on a mathematical ground.

### 2.3.2 Derivation of resonance states

To interpret resonance states in the framework of a physical-mathematical approach,[1;99;100] let us consider first the time-dependent Schrödinger equation of a free particle scattered in a central potential $V(r)$, *i.e.*, a potential only depending on the distance $r$ from the origin (*e.g.*, the Coulomb potential):

$$\mathrm{i}\hbar\frac{\partial\Psi(\mathbf{r},t)}{\partial t} = \hat{H}\Psi(\mathbf{r},t), \tag{2.16}$$

where i is the imaginary unit, $\hbar$ is the reduced Planck constant, $m$ is the mass of the particle, and the wave function has the form

$$\Psi(\mathbf{r},t) = \psi(\mathbf{r})\exp((-\mathrm{i}/\hbar)Et), \tag{2.17}$$

where $\psi(\mathbf{r})$ is the eigenfunction of the time-independent Schrödinger equation:

$$\left(-\frac{\hbar^2}{2m}\Delta + V(r)\right)\psi(\mathbf{r}) = E\psi(\mathbf{r}). \tag{2.18}$$

Eq. (2.18) can be given in a rearranged form, after introducing the variables $k^2 = (2m/\hbar^2)E$ and $U(r) = (2m/\hbar^2)V(r)$

$$\Delta\psi(\mathbf{r}) + (k^2 - U(r))\psi(\mathbf{r}) = 0, \tag{2.19}$$

where $\Delta$ is the Laplacian and $\mathbf{r}$ refers to the coordinates of the particle. Since a central potential is considered, it is advantageous to use spherical polar coordinates, where the wave function can be searched for in the following form

$$\psi(\mathbf{r}) = R(r)Y(\phi, \theta), \tag{2.20}$$

where $\phi$ and $\theta$ are the polar angles. After this separation of variables, one comes to the problem of several one-dimensional differential equations for the radial part of the wave function, corresponding to different $l$ values, which characterize the angular momentum of the system:

$$\frac{\partial^2\chi_l(r)}{\partial r^2} + \left(k^2 - U(r) - \frac{l(l+1)}{r^2}\right)\chi_l(r) = 0, \quad l = 0, 1, 2, .... \tag{2.21}$$

The stationary wave function, corresponding to a given $l$ value, has the form

$$\psi_l(\mathbf{r}) = \frac{1}{r}\chi_l(r)Y_l^m(\phi, \theta), \tag{2.22}$$

where $Y_l^m(\phi, \theta)$ are the spherical harmonics. In the scattering problem, the asymptotic, *i.e.*, $r \to \infty$, form of Eq. (2.21) is of interest, since in experiments the detection of a scattered particle takes place far from the scattering center. This asymptotic form can be written as

$$\frac{\partial^2\chi_l^{\mathrm{as}}(r)}{\partial r^2} + k^2\chi_l^{\mathrm{as}}(r) = 0, \quad l = 0, 1, 2, .... \tag{2.23}$$

At such large distances the interaction potential becomes negligible, and the particle behaves like a free particle, with the corresponding general solution of the Schrödinger

equation:

$$\chi_l^{\mathrm{as}}(r) = A_l(k)\exp(\mathrm{i}kr) + B_l(k)\exp(-\mathrm{i}kr). \tag{2.24}$$

The $\chi_l$ functions are characterized by a given $l$ value, and consist of an outgoing (first term) and an incoming (second term) wave. Based on Eq. (2.24) three different cases can be derived, due to different boundary conditions imposed to the problem:

(1) If one intends to obtain the bound states of the system, one should impose boundary conditions that ensure $\chi_l$ to be square integrable ($\in L^2$), and therefore be in the Hilbert space. For such a function space, the Hermitian Hamiltonian will have real eigenvalues. This holds if $E < 0$, where $E = 0$ is the threshold energy of dissociation, therefore $k$ is pure imaginary and can be written as $k = \mathrm{i}\lambda$, if $\lambda \neq 0$. This way, only the first (let us consider $\lambda > 0$) term can be non-zero, otherwise the wave function would diverge at infinity. Thus, the wave function of a bound state decays exponentially at the asymptotic region, and has the form

$$\chi_l^{\mathrm{as}}(r) = A_l(k)\exp(-\lambda r). \tag{2.25}$$

(2) Scattering or continuum states are not square integrable; therefore they are not members of the Hilbert-space. However, for their analogous treatment another normalization condition can be introduced, the so-called Dirac-delta normalization, which demands the wave function to be finite at infinity. For this, the boundary conditions must be met with $E > 0$, and thus the terms in Eq. (2.24) will be incoming and outgoing waves.

(3) In the case of resonance states, the boundary conditions imposed must be consistent with a system decaying in time into its subsystems. This can be achieved if the wave function has no incoming parts. To describe the exponential decay of resonances in time, from Eq. (2.17) it follows that $E$ must be complex. Consequently, the eigenfunctions of the Hamiltonian will not be members of the Hilbert space, whose asymptotic form can be given as

$$\chi_l^{\mathrm{as}} = A_l(k)\exp(\mathrm{i}kr) \tag{2.26}$$

Since initially we assumed a particle scattered by a central potential, the so-called scattering $S$ matrix is worth introducing, which connects the initial and final states of asymptotically free particle(s) that undergo a scattering process. $S(k)$ can be defined as the ratio between the amplitude of the outgoing and the incoming wave:[100]

$$S(k) = A_l(k)/B_l(k) \tag{2.27}$$

In our model case $S(k)$ is only one dimensional. A general form of $S(k)$ can be given as:[1]

$$S(k) = \exp(\mathrm{i}2\delta(k)), \tag{2.28}$$

where $\delta(k)$ is termed the phase shift of the unitary $S$ matrix, which is the phase change induced by the interaction potential in the asymptotic regions of the scattering wave function, and is a central quantity in studying scattering processes.[62] $S(k)$ can have poles in the following cases:[100] (1) If $A_l(k)$ has a pole, but these are independent of the potential, and exist even when the potential becomes negligible; thus, these are "false" poles. (2) If the amplitude, $B_l(k)$, of the incoming wave vanishes. If these poles are on the positive imaginary axis of the complex $k$-plane (*i.e.*, on the negative real axis of the complex energy-plane), they are associated with bound states, while the poles embedded in the fourth-quadrant of the $k$-plane ($\mathrm{Re}(k) > 0$ and $\mathrm{Im}(k) < 0$) correspond to resonance states. Branch cuts of the $S$ matrix can be associated with the opening of new scattering channels.[62]

Near the $n^{th}$ isolated pole, $S(k)$ can be written as[100]

$$S(k) \propto \frac{1}{(k - k_n)} \quad \text{and} \quad \frac{\mathrm{dln}S(k)}{\mathrm{dk}} = \frac{-1}{(k - k_n)}. \tag{2.29}$$

It can be shown[100] that a closed contour integration of this derivative on the complex $k$-plane provides the number of the poles, $N$, in the fourth-quadrant of the $k$-plane. Then, the density of states, $\rho = \mathrm{d}N/\mathrm{d}E$, can also be determined. The local maxima of the density of states, having a Lorentzian shape, is obtained as[100]

$$\rho_{\max}(k = \mathrm{Re}(k_n)) = (-2\pi\mathrm{Im}(E_n))^{-1} \tag{2.30}$$

and the full-width half-maximum of the $n^{\mathrm{th}}$ Lorentzian peak, which gives the inverse

of the lifetime of the resonance state, $\Gamma_n$, is

$$\Gamma_n = -2\mathrm{Im}(E_n) \tag{2.31}$$

Thus, the complex eigenvalue corresponding to a resonance state is

$$E_{\mathrm{res}} = E_n - \mathrm{i}\frac{\Gamma_n}{2}, \tag{2.32}$$

where $E_n$ is called the resonance energy, or "position", and $\hbar/\Gamma$ is the lifetime of the given resonance state.

The complete asymptotic form of the resonance wave function of our model problem, corresponding to one pole of the $S$-matrix, can be given as[100]

$$\begin{gathered}\Psi_l^{\mathrm{as}} = \frac{1}{r}\chi_l^{\mathrm{as}}(r)Y_l^m(\phi,\theta)\exp\left(-\frac{\mathrm{i}}{\hbar}Et\right) = \\ Y_l^m(\phi,\theta)\frac{A_l(k)}{r}\exp(\mathrm{i}ar)\exp(br)\exp\left(-\frac{\mathrm{i}}{\hbar}\left(E_n - \mathrm{i}\frac{\Gamma_n}{2}\right)t\right) = \\ Y_l^m(\phi,\theta)\frac{A_l(k)}{r}\exp\left(\mathrm{i}\left(ar - \frac{E_n}{\hbar}t\right)\right)\exp(br)\exp\left(-\frac{\Gamma_n}{2\hbar}t\right),\end{gathered} \tag{2.33}$$

where

$$\begin{gathered}a = \left(\frac{2m}{\hbar^2}\right)^{1/2}\left(E_n^2 + \left(\frac{\Gamma_n}{2}\right)^2\right)^{1/4}\cos(\zeta) \\ b = a\tan(\zeta) \\ \zeta = \frac{1}{2}\arctan\left(\frac{\Gamma_n}{2E_n}\right)\end{gathered}$$

It is transparent from Eq. (2.33) that $\Gamma_n$ is the inverse lifetime of the $n^{th}$ resonance state, and $\Gamma > 0$ ensures the characteristic exponential decay in time. $E_n > 0$ also holds (resonances have higher energy then the dissociation threshold), which forces $b > 0$, meaning that the resonance wave function diverges along the $r$ coordinate.

This derivation of resonance states can be generalized to multiple dimensions as one chooses the dissociation or reaction coordinate, along which the decay proceeds, as $r$.

## 2.4 Computation of resonance states

In this Section different time-independent approaches will be presented, which are widely used for determining resonance energies and lifetimes. After a brief outline of such techniques in scattering theory, three variational methods are introduced, two non-Hermitian procedures, *i.e.*, the complex coordinate scaling and the complex absorbing potential technique, and a Hermitian one, the stabilization method. Time-dependent methods also exist to identify resonance states,[17;95] although such techniques are beyond the scope of this thesis.

### 2.4.1 Scattering techniques

Scattering resonance-computing codes, based directly on the determination of the scattering matrix, provide collisional cross sections as a function of energy, in which resonance states are indicated by peaks at certain energies, including several values of $J$, the total angular momentum quantum number of the system. The contribution of different state-to-state cross sections, characterized by transitions between states unambiguously labeled by different quantum numbers, to the total cross section, can also be obtained. For example, in a three-dimensional problem, *i.e.*, in the case of an atom-diatom collision, these labels can be $l$ and $j$ values, with $|j-l| \leq J \leq j+l$, where the $l$ quantum number characterizes the relative orientation of the colliding fragments, while $j$ is related to the rotation of the diatomic molecule. Total cross sections can also be decomposed to so-called partial waves, characterized by a given $J$ value.

Peaks in the cross sections can then be approximated with Lorentzian-type functions, *e.g.*, the Breit-Wigner formula,[62] from which resonance energies and lifetimes can be extracted. Lifetimes of resonance states can also be determined by computing the eigenvalues of the so-called Smith lifetime matrix.[101] Also, the phase shift of the scattering matrix, introduced in Eq. (2.28), plotted against the energy can be used to obtain resonance positions and widths, since it changes by $\pi$ when the energy of the system coincides with the resonance position. In the case of asymmetric line shapes in the cross sections, the Feshbach–Fano[102] formula can be applied to extract resonance

properties.

### 2.4.2 Complex coordinate scaling

Resonance wave functions, as shown in Eq. (2.33), diverge at infinity and as such, they are not the member of the $L^2$ Hilbert space. However, by applying a transformation on the TISE, these functions can be transformed to be square-integrable functions, with the complication that the new Hamiltonian, of which the transformed states are the eigenfunctions, will be complex. Following such a procedure, one can obtain the complex eigenvalues of resonance states, with corresponding square-integrable eigenfunctions.

One way to make the resonance wave functions square integrable is to apply a similarity transformation on the Hamiltonian.[1;100] Such a transformation can be chosen as the following, so-called complex scaling operator:

$$\hat{S}_\vartheta = \exp\left(\mathrm{i}\vartheta r \frac{\partial}{\partial r}\right), \tag{2.34}$$

which rotates the argument of the function, *i.e.* the dissociation coordinate, on which it is applied by $\vartheta$ on the complex plane.

Let us give some mathematical insight into this so-called complex coordinate scaling (CCS) procedure. We start from the TISE of the system,

$$\hat{H}\Psi_{\mathrm{res}} = E_{\mathrm{res}}\Psi_{\mathrm{res}}, \tag{2.35}$$

with $\Psi_{\mathrm{res}}$ diverging at infinity and $E_{\mathrm{res}}$ being the exact (complex) resonance eigenvalue. Let the Schrödinger equation be the subject of the above defined similarity transformation, performed by the invertible $\hat{S}$ operator:

$$\hat{S}\hat{H}\hat{S}^{-1}\hat{S}\Psi_{\mathrm{res}} = E_{\mathrm{res}}\hat{S}\Psi_{\mathrm{res}}. \tag{2.36}$$

It can be shown that $\hat{S}\Psi_{\mathrm{res}}$ will be square integrable for certain values of $\vartheta$. It is also known that continuum states are rotated by $2\vartheta$ under such a transformation.[100] From

an illustrative point of view, the complex scaling of the dissociation coordinate makes the poles of the scattering-matrix, embedded in the fourth quadrant of the complex plane, "visible". If a new scattering channel opens, *i.e.*, at a certain energy, continuum states above this energy become rotated by $2\vartheta$, thereby revealing the poles (resonances) above the new channel.

The new complex Hamiltonian, $\hat{S}\hat{H}\hat{S}^{-1}$, with square integrable eigenfunctions, is then suitable be built in an $L^2$ basis, and then diagonalized, providing the complex resonance eigenvalues located between the real axis and the rotated continuum. This procedure should be carried out for several values of $\vartheta$ while so-called $\vartheta$ trajectories form on the complex plane, in which stationary points reflect the resonance eigenvalues.

Modified versions of the complex coordinate scaling also exist,[1;100] such as the so-called exterior complex scaling, useful for non-analytical potentials. This technique involves the rotation of the dissociation coordinate in external regions of the PES where it is negligible, or can be approximated by an analytic function. The so-called smooth exterior scaling smooths out the transition from a non-scaled region to the scaled region.

After the generalization of the inner product and the variational principle to the complex non-Hermitian formalism,[1] one can use the conventional computational methods that were originally developed for Hermitian problems. It is noted that the complex generalized variational principle provides an upper bound neither for the real nor for the imaginary part of the resonance eigenvalue when these are computed using a trial wave function.

### 2.4.3 The complex absorbing potential technique

The complex absorbing potential (CAP) method[98;103–105] is also based on making the original rovibrational Hamiltonian complex, having square-integrable eigenfunctions and complex eigenvalues, which can be associated with the resonance energies and inverse lifetimes. The reason for such a transformation, as outlined in Section 2.2, is that several types of well-developed variational bound-state-computing codes are available, based on standard $L^2$ techniques, and one prefers to stay on the ground

of such standard methods.

In the CAP technique the transformation of the resonance eigenfunctions into square-integrable functions is achieved by adding a complex potential to the original Hamiltonian, $\hat{H}$:

$$\hat{H}'(\eta) = \hat{H} - \mathrm{i}\eta\hat{W}(R), \tag{2.37}$$

where $W$ is a real valued function of the $R$ dissociation coordinate assuming nonzero values at the asymptotic region of the PES, and $\eta$ is the so-called strength parameter of the CAP. Adding the CAP to the Hamiltonian makes the resonance eigenfunctions damped at the asymptotic region of the PES; thus, they become similar to square-integrable functions. The new Hamiltonian, $\hat{H}'(\eta)$ will be complex, like in the case of the CCS technique, and its eigenvalues will approximate the resonance eigenvalues.

Damping the resonance wave function allows for its expansion in an $L^2$ basis, which consists usually of the eigenfunctions of the original Hamiltonian. After building the complex symmetric Hamiltonian in this basis, it is diagonalized providing the required resonance eigenpairs. The obtained eigenvalues (along with the eigenfunctions) are approximate, as, of course, the addition of the CAP changes the exact resonance eigenvalues. This effect can be described as a power series in $\eta$:[103]

$$E(\eta) = E_{\mathrm{res}} + c_1\eta + c_2\eta^2 + \dots \tag{2.38}$$

If we used an infinite basis to expand the resonance wave function, this would be the only difference with respect to the exact eigenvalues. However, in real computations one employs a finite basis, which also causes an error with respect to the exact resonance eigenvalues. This error is also a complex valued function of $\eta$.[103] If the $\eta$ strength parameter is increased, the first error occurring due to the CAP, also increases, as seen from the power series in Eq. 2.38. In contrast, the second error decreases with increasing $\eta$, since if we use a stronger CAP to damp the wave function, it will be more resemblant to a square-integrable function, thus will be more suitable to an $L^2$ expansion, which manifests in a smaller basis set error.

Thus, in practice, one should build and diagonalize the complex Hamilton matrix at many different values of $\eta$, starting from a large value, where the first error dominates,

to a sufficiently small value, where the basis set error will be large. Then, a trajectory forms on the complex plane corresponding to each eigenvalue, where each point of the trajectory belongs to one $\eta$ value. Based on the above discussion, there must be an optimal value for $\eta$, where the total error is minimal. This point is called a stability point, and it manifests as a higher density region of eigenvalues. At this point a cusp in the trajectory also occurs, which can be explained by the fact that the two complex valued errors have different phases, and thus approach the stability point from different directions.[103] Consequently, this stability point provides the best approximation to the exact resonance eigenvalue.[103]

In applications for real systems it may be necessary to take more than one dissociation paths into account; in this case multiple dissociation coordinates can be introduced and treated with the CAP method separately.

It has been shown[100;106] that the complex absorbing potential method is closely related to the exterior or smooth exterior complex scaling techniques.

The major advantage of the CAP technique lies in its straightforward generalizability. As seen above, the complex coordinate scaling method requires the rotation of the dissociation coordinate in the complex plane, thereby modifying all the terms in the original Hamiltonian that depend on this coordinate. In contrast, the complex absorbing potential does not even require the knowledge of the Hamiltonian in an analytic form, which makes it particularly advantageous for general algorithms, mentioned in Sections 2.2.1 and 2.2.2, which construct the kinetic energy part of the Hamiltonian numerically, this way being capable of treating arbitrary coordinate systems. Linking this technique to such a general code makes the transition to larger systems possible, since deriving the analytical form of the Hamiltonians of large systems becomes increasingly difficult. During my PhD work, I have linked the CAP method to the GENIUSH bound-state-computing program and successfully applied it for weakly-bound complexes, among which,to the best of my knowledge, $H_2$·CO was the first four-atomic system subjected to a non-Hermitian variational resonance computation.

### 2.4.4 The stabilization method

It is shown in detail in Ref. 1 that a resonance state, within the Hermitian formalism of quantum mechanics, is associated with a collection of continuum states (or a wave packet) and not with a single stationary solution of the Schrödinger equation. Those continuum states are identified as a resonance state, whose energy, $E$, is within the range $E_{\rm res} - \Gamma/2 < E < E_{\rm res} + \Gamma/2$. These states are shown to be localized in the interaction region of the potential, and appear more and more densely, as their energy approaches $E_{\rm res}$. This approach works best for narrow resonances, *i.e.*, those having long lifetimes.

The stabilization method is based on the high density of continuum states around a resonance energy. It has been noticed,[96;100;107] that the eigenenergies of the system's Hamiltonian, determined variationally depending on a certain parameter, are changed when this parameter is varied, but remain stable in the vicinity of a resonance energy. This can be visualized by discretizing the continuum energies by constraining the corresponding wave functions into a box, with length $L$. In such a case, since the states that have an energy close to the resonance energy are localized in the interaction region, they are affected only minimally as the size of the box varies. In contrast, the delocalized continuum states oscillating with a large amplitude, along with the corresponding (now discrete) energy levels are strongly affected by the variation of the $L$ parameter. Thus, if we plot the energies of the variational solutions of the Hamiltonian at certain values of $L$, crossing of energy levels is expected to be observed.[1] However, these levels will not cross in most cases due to the identical symmetry of the corresponding states, hence one observes avoided crossings close to the resonance energies.[1] If a sufficiently large basis is used for the variational computations, the lifetime of a given resonance state can be determined from the variation of the energies in the vicinity of such avoided crossings.

The concrete procedure of the stabilization method[96;107;108] thus involves the monitoring of the eigenvalues obtained from several (ro)vibrational bound state computations above the first dissociation asymptote, while the range along the dissociation coordinate is extended. The resonance eigenvalues can be made converged with respect

to changing the basis set size and the extension along the dissociation coordinate[107].

Based on the above discussion, in the vicinity of resonance energies an accumulation of energy levels, obtained from computations performed with different maximal extensions along the dissociation coordinate, is observed. Resonances are therefore associated with energies that are adopted by several eigenvalues while the range along the dissociation coordinate is changed. This increased density of energy levels can be made clearly visible when shown on a histogram based on binning, whereby those eigenvalues, computed by using different $R$ ranges, are counted that adopt an energy value within the given bin.

During the course of my PhD research I have identified several resonance states with the help of the stabilization method, complementing the results obtained from non-Hermitian computations.

# Chapter 3

# GENIUSH-CAP

## 3.1 The algorithm and its implementation

During my PhD research I have augmented the toolbox of the GENIUSH rovibrational bound-state computing code[20;21;86;109] with the CAP technique,[98;103–105] to allow the determination of resonance states of flexible, polyatomic molecules. The newly developed code is called GENIUSH-CAP, and is written in C++ language.

GENIUSH, as mentioned, computes the (ro)vibrational bound eigenvectors, which are used as a basis set in the GENIUSH-CAP computations. This allows one to exploit all the advantages of GENIUSH. the use of arbitrary coordinate systems for, in principle, molecules or complexes of arbitrary size. Weakly-bound systems featuring large-amplitude motions, the target molecules of my investigations, can also be treated efficiently in this protocol. Furthermore, the simple definitions of reduced-dimensional models, where the non-active internal coordinates are fixed to certain, usually their equilibrium, values are also possible.

The CAP method, as mentioned above, involves the perturbation of the original rovibrational Hamiltonian of GENIUSH with a complex potential, which damps the resonance eigenfunctions of the system in the asymptotic region of the PES. As intro-

duced in Eq. (2.37), the modified Hamiltonian can be written as

$$\hat{H}'(\eta) = \hat{H} - \mathrm{i}\eta\hat{W}(R), \tag{3.1}$$

where i is the imaginary unit, and $\hat{W}(R)$ is a real valued function of the $R$ dissociation coordinate. As a consequence of the addition of the CAP, as discussed above, the resonance wave functions become resemblant to square-integrable functions. This makes it possible to use the $L^2$ eigenvectors obtained from solving the eigenvalue problem of the original real symmetric Hamiltonian as basis functions during the resonance computations. Thus, the resonance states are searched in the form

$$\Psi_{\mathrm{res}} = \sum_{i=1} a_i \Phi_{\mathrm{GEN},i}, \tag{3.2}$$

where $a_i \in \mathbb{C}$, $\Psi_{\mathrm{res}}$ is the resonance wave function, and $\Phi_{\mathrm{GEN},i}$ is the $i^{\mathrm{th}}$ eigenvector with an eigenenergy either below or above the first dissociation asymptote, computed with GENIUSH. Despite having no real physical meaning, $\Phi_{\mathrm{GEN},i}$ with energies above the first dissociation limit serve well as $L^2$ basis functions for expanding the resonance wave functions and covering the desired energy range of resonance states to be identified.

In GENIUSH, rovibrational eigenstates are obtained as linear combinations of the direct products of DVR vibrational basis functions and rotational basis functions:

$$\begin{gathered}\Phi_{\mathrm{GEN},i}(q^{(1)}, q^{(2)}, ..., q^{(N)}, \alpha, \beta, \gamma) = \\ \sum_{kl...m} \sum_{K=-J}^{J} c^{i}_{kl...m,K}\ \chi^{(1)}_k(q^{(1)})\chi^{(2)}_l(q^{(2)})...\chi^{(N)}_m(q^{(N)})C_{JKM}(\alpha, \beta, \gamma),\end{gathered} \tag{3.3}$$

where $q^{(1)}, q^{(2)}, ..., q^{(N)}$ refer to the $N$ active coordinates used in the given computation, and $\chi^{(1)}_k, \chi^{(2)}_l, ..., \chi^{(N)}_m$ denote the DVR functions on each active coordinate. $C_{JKM}(\alpha, \beta, \gamma)$ refer to the $2J + 1$ ($J$ is the rotational quantum number) orthonormal Wang functions used as rotational basis functions[21;47] depending on the $\alpha, \beta, \gamma$ angles which describe the rotations around the axes of the body-fixed frame. $K = -J, ..., J$ is related to the projection of the total angular momentum $\hat{J}$ of the system onto the body-fixed z axis, and $M = -J, ..., J$ is the projection of $\hat{J}$ onto the space-fixed Z-axis. In the GENIUSH-CAP program we assume that $M = 0$. The matrix elements of the new complex Hamiltonian represented in the $\{\Phi_{\mathrm{GEN},i}\}$ basis can be obtained as follows:

$$H^{'}(\eta)_{ij} = \langle \Phi_{\mathrm{GEN},i} | \, \hat{H}^{'}(\eta) \, | \Phi_{\mathrm{GEN},j} \rangle = E_i \delta_{ij} - \mathrm{i}\eta \, \langle \Phi_{\mathrm{GEN},i} | \, \hat{W} \, | \Phi_{\mathrm{GEN},j} \rangle \, , \tag{3.4}$$

where $E_i$ is the $i^{\mathrm{th}}$ eigenvalue of the original Hamiltonian. Exploiting the orthogonality of the GENIUSH eigenvectors, one only needs to determine the matrix elements of the complex potential in the basis of these vectors:

$$\begin{gathered} W_{ij} = \int_{q_{min}^{(1)}}^{q_{max}^{(1)}} \int_{q_{min}^{(2)}}^{q_{max}^{(2)}} ... \int_{q_{min}^{(N)}}^{q_{max}^{(N)}} \sum_{kl...m} \sum_{k'l'...m'} \sum_{K=-J}^{J} c^{i}_{kl...m,K} c^{j}_{k'l'...m',K} \\ \chi_k^{(1)}(q^{(1)}) \chi_l^{(2)}(q^{(2)}) ... \chi_m^{(N)}(q^{(N)}) \hat{W} \; \chi_{m'}^{(N)}(q^{(N)}) ... \chi_{l'}^{(2)}(q^{(2)}) \chi_{k'}^{(1)}(q^{(1)}) \\ dq^{(1)} dq^{(2)} ... dq^{(N)} \xi(q^{(1)} q^{(2)} ... q^{(N)}). \end{gathered} \tag{3.5}$$

Since $\hat{W}$ is independent of the $\alpha, \beta, \gamma$ angles, the integration over these variables can be performed trivially, and due to the orthonormality of the Wang functions[47] this results in $\delta_{KK'}$, where $\delta$ is the Kronecker delta symbol. $\xi(q^{(1)} q^{(2)} ... q^{(N)})$ refers to the volume element of the integration. To evaluate this integral we employ the Gaussian quadrature method using the $q_a^{(1)}, q_b^{(2)}, ..., q_c^{(N)}$ DVR grid points as quadrature points. Thus, we transform this integral to a sum, where advantages of the DVR technique can be exploited:

$$\begin{gathered} W_{ij} = \sum_{ab...c} \sum_{kl...m} \sum_{k'l'...m'} \sum_{K=-J}^{J} w_a w_b ... w_c \; c^{i}_{kl...m,K} c^{j}_{k'l'...m',K} \\ \chi_k^{(1)}(q_a^{(1)}) \chi_l^{(2)}(q_b^{(2)}) ... \chi_m^{(N)}(q_c^{(N)}) W(q_a, q_b, ... q_c) \chi_{m'}^{(N)}(q_c^{(N)}) ... \chi_{l'}^{(2)}(q_b^{(2)}) \chi_{k'}^{(1)}(q_a^{(1)}), \end{gathered} \tag{3.6}$$

where the $w_a w_b ... w_c$ are the quadrature weights. Using the DVR of the original Hamilton matrix implies that[58]

$$\chi_k(q_a) = w_a^{-1/2} \delta_{ka}. \tag{3.7}$$

Due to Eq. (3.7), the following simple formula is obtained for the elements of the complex Hamilton matrix:

$$H^{'}(\eta)_{ij} = E_i \delta_{ij} - \mathrm{i}\eta \sum_{ab...c} \sum_{K=-J}^{J} c^{i}_{ab...c,K} c^{j}_{ab...c,K} W(q_a, q_b, ... q_c). \tag{3.8}$$

After building the complex Hamilton matrix, it is diagonalized with a direct diagonalization method, invoked from the Lapack++ package.[110] Avoiding the use of an iterative eigensolver is possible due to the relatively small dimension of the matrix.

One should diagonalize the complex matrix at many values of $\eta$, and plot these eigenvalues, having the form $E - \mathrm{i}\Gamma/2$, on the complex plane. Then, a visual analysis follows, in which one identifies cusps in the eigenvalue trajectories, and associates them with resonance energies and lifetimes.

To gain further information of a resonance state determined with the GENIUSH-CAP procedure, I have developed a tool, a code also written in C++, to visualize the resonance wave functions. For this, Eqs. (3.2) and (3.3) are used, and the square of the absolute value of the complex $\Psi_{\mathrm{res}}$ vector corresponding to the cusp $\eta$ value, $\sum_{K=-J}^{J} |\sum_i a_i c^i_{ab\ldots c,K}|^2$, is plotted along two selected coordinates (the other coordinates are held fixed at given, usually their equilibrium, values). Such a visualization of the resonance eigenvectors can provide a qualitative understanding of the studied resonance phenomenon, since the nodal structures of the resonance wave functions reveal valuable information for the given state.

The newly developed GENIUSH-CAP code has been tested and validated by comparing its results, using the $H_2He^+$ molecule as a test system, to resonance energies and lifetimes obtained from complex coordinate scaling computations, which utilized the D$^2$FOPI-CCS program, developed previously in our group.[5] These results are presented later in this thesis, in Section 5.3, put in the context of the resonance-structure of $H_2He^+$.

## 3.2 Parameters of the GENIUSH-CAP computations

To obtain the desired resonance eigenvalues from GENIUSH-CAP computations, one can change and optimize several parameters:

- The range where the CAP is turned on, *i.e.*, the length of the so-called CAP-active interval along the dissociation coordinate, which is a sensitive parameter for finding certain resonance states, depending on their nature of delocalization.
- The functional form of the CAP.

- The interval of the $\eta$ parameter, which usually covers many orders of magnitude, depending on the given system.
- The number of $\eta$ values used in one computation, thereby setting the "resolution" of the eigenvalue trajectories.
- The number of GENIUSH eigenvectors as basis functions.

In what fallows, the choice of these parameters will be detailed in each case of a system studied. Here, just a few remarks are made regarding the technical details of the GENIUSH-CAP computations:

(1) The functional form of the CAP has been chosen to be a polynomial with an order of $1, 2, 3$ or $5$, optimized by Poirier and Carrington.[111] Employing different functional forms during test computations usually proved to have only a minimal effect on the results; thus, the results presented throughout this thesis were usually obtained by using the highest-order polynomial of Ref. 111.

(2) In GENIUSH-CAP the $\eta$ CAP-strength parameter is distributed according to the following exponential[112] function within a given interval:

$$\eta_j(\eta_{\min}, \eta_{\max}, n, j) = \eta_{\min} - 1 + \exp[\log((\eta_{\max} - \eta_{\min}) + 1)j/(n-1)], \tag{3.9}$$

where $\eta_{\mathrm{j}}$ is the $j^{\mathrm{th}}$ value of $\eta$, $n$ is the number of $\eta$ values, and $\eta_{\min}$ and $\eta_{\max}$ are the minimum and maximum values of the given $\eta$ interval, respectively.

(3) In the case of resonance computations on weakly-bound systems an advantage is that it is sufficient to compute a low number of bound states. However, in the case of more strongly bound molecules, it might be possible to exclude a number of low-energy bound eigenvectors from the basis used for the CAP computation. It is also necessary to compute a sufficient number of GENIUSH eigenvectors above the first dissociation limit to fully describe the energy range of the resonance states sought. Such eigenstates have no real physical meaning; this might be the reason why it can sometimes be a challenging task to converge them with the iterative Lanczos algorithm.

# Chapter 4

# The nuclear dynamics of the $Ar{\cdot}NO^+$ complex below and above dissociation

## 4.1 Importance of the $Ar{\cdot}NO^+$ complex

Weakly-bound triatomic systems involving a strongly-bound diatomic, AB, and a rare gas atom (Rg = He, Ne, Ar, Kr) loosely attached to it[113–117] represent ideal benchmark systems to study van der Waals interactions. Due to their weakly-bound nature, Rg·AB complexes are excellent subjects to study the dynamical consequences of the adiabatic separation of the diatomic vibrational degree of freedom. In the case of Rg·AB systems the fundamental frequency of the diatomic fragment is much higher than the first dissociation energy of the complex, which is often only a few tens of $cm^{-1}$. The shallow potential well of Rg·AB complexes also provides a good chance to obtain results bridging molecular scattering and spectroscopy. Molecules and complexes involving rare gases are also of interest in the study of cold collisions,[118] as well as in astrophysics.[119–121]

There are many possible variants of the diatomic molecule involved in Rg·AB complexes. For example, AB can be neutral or charged. As examples of neutral complexes the He·CN,[122] He·CO,[123] He·HF,[124] Ne·$H_2$,[125] Ar·NO,[126–128] and the Rg·halogen[129–131]

systems can be mentioned. If AB has a positive charge, the bonding to Rg, through stronger polarization, may become relatively strong and the first dissociation energy drastically increases, up to several hundred $cm^{-1}$. This leads to a relatively large number of bound rotational-vibrational states for the ground electronic state and perhaps more interesting and involved dynamical behavior.[132;133] The charged molecular species investigated include, for example, $Ar{\cdot}NO^+$,[134–145] $Ar_mH^+$,[146] and $Ar_mHCl^+$.[147;148]

During my PhD research I have studied the nuclear dynamics of the relatively strongly bound $Ar{\cdot}NO^+$ complex both below and well above the first dissociation asymptote.

This investigation offers several challenges:

- Because of the shallow potential well and the low barrier to end-over-end hindered internal rotation of the monomers, Rg·AB van der Waals complexes are particularly floppy and exhibit large amplitude motions upon excitation. This invalidates the use of anharmonic force fields[149] and standard vibrational perturbation theory[44;45] treatments for dynamical studies; for this class of systems variational treatments on accurate global PESs are mandatory.
- Bound vibrational energy levels have been obtained for $Ar{\cdot}NO^+$ in experimental studies.[134;141] These low-resolution results call for a theoretical interpretation based on energies and wave functions obtained from variational computations.
- Rovibrational resonance states have neither been computed nor measured for $Ar{\cdot}NO^+$. However, as it will be shown shortly, these states highlight very interesting physical phenomena.

Besides investigating the rovibrational bound-states of $Ar{\cdot}NO^+$, the main emphasis in this thesis is on the study of its resonance states above the first dissociation asymptote, $NO^+(X^1\Sigma^+)$ + Ar, using both Hermitian and non-Hermitian variational techniques. Results are also compared to those obtained with molecular scattering methods, and experiments, where possible.

## 4.2 Computation of bound and resonance states

### 4.2.1 The potential energy surface

An accurate 3D PES developed in Ref. 145 for the ground electronic state of $Ar{\cdot}NO^+$ was employed to study the dynamics of the $Ar{\cdot}NO^+$ complex. The equilibrium structure of $Ar{\cdot}NO^+$ on this PES can be conveniently represented by the standard Jacobi coordinates, $r$, $R$, and $\theta$, which are also used to describe the vibrational motions of the complex: $r$ denotes the distance between the N and O atoms, $R$ is the distance of Ar from the center of mass of the $NO^+$ unit, and the $\theta$ angular coordinate is the included angle of the two vectors. $Ar{\cdot}NO^+$ is an approximately T-shaped molecule with the Ar atom lying on the N side. The precise equilibrium structural parameters of the $Ar{\cdot}NO^+$ complex, calculated from the 3D PES,[145] are $r_e = 2.013377$ bohr, $R_e = 5.858267$ bohr, and $\theta_e = 66.6638°$. The pure electronic dissociation energy corresponding to this PES is $D_e = 980.35$ cm$^{-1}$ , while the corresponding $D_0$ is 887.00 cm$^{-1}$ .

### 4.2.2 Scattering computations

Details about the close coupling (CC) computations, performed by Professor Thierry Stoecklin and utilizing the code called Newmat,[150] can be found in Ref. 145. A few details of the computation of both the bound and resonance states are given below. The Newmat code uses the so-called log derivative propagator.[151] During the study of $Ar{\cdot}NO^+$ a step size of 0.01 bohr along the $R$ dissociation coordinate was employed. The minimum and maximum propagation distances were 4.0 and 50.0 bohr, respectively. With the CC technique, (ro)vibrational ($J = 0, 1$, and 2) bound states and vibrational ($J = 0$) resonance states have been obtained.

It must be noted that $Ar{\cdot}NO^+$ has a very complex resonance structure; thus, performing the partial wave expansion of the cross sections obtained from CC computations would have been tedious. Therefore, resonance positions and widths were not extracted this way from the CC computations but rather the profile of the cross sections

was compared with the positions of the resonances obtained with GENIUSH-CAP. Nevertheless, the eigenvalues of the so-called close-coupling Smith lifetime matrix[101] were also determined following the method of Ref. 152 and compared to the lifetime values obtained from GENIUSH-CAP computations.

### 4.2.3 GENIUSH bound-state computations

Bound rovibrational energy levels of Ar·$NO^+$ were obtained with the GENIUSH code by using 20 and 100 Laguerre-DVR grid points for the $r$ and $R$ coordinates scaled to the ranges of $[1.68, 2.64]$ bohr and $[4.0, 40.0]$ bohr, respectively. For the angular coordinate 40 unscaled Legendre-DVR grid points are employed for $J = 0$. Due to the use of Legendre-DVR on the angular coordinate even in the $J > 0$ case, which is not coupled to the rotational basis, for $J > 0$ an increased number, 110, of Legendre-DVR points had to be used. For the $J > 0$ rovibrational computations the $R$ embedding and a basis extended with $2J + 1$ orthonormal Wang functions is used. One- (fixed $R$ and $\theta$) and two- (fixed $r$) dimensional models were also applied to explore the coupling of the vibrational degrees of freedom in the Ar·$NO^+$ complex. The inactive coordinates were fixed at their equilibrium values. The rovibrational states were then characterized by counting the nodes of the computed wave functions, obtained from GENIUSH.

### 4.2.4 GENIUSH-CAP parameters

To variationally determine numerous resonance states of the Ar·$NO^+$ complex, the GENIUSH-CAP code was employed. During the GENIUSH-CAP computations, the range of the $R$ dissociation coordinate where the CAP was switched on was varied between 15-50 bohr, by increasing the starting value of the interval with a step size of 5 bohr. Choosing the appropriate CAP-active range of the dissociation coordinate is very important to get all the resonances in a given energy interval, even those having a wave function localized at the asymptotic region of the PES; in such a case the resonance wave function should be damped only in a very small interval near the end of the $R$-range. The functional form of the CAP was chosen as the highest order polynomial of Ref. 111. The $\eta$ CAP-strength parameter covered a range of $10^{-2} - 10^{-9}$,

divided into different (sometimes overlapping) intervals usually covering three orders of magnitude. Within these intervals the $\eta$ parameter was distributed according to Eq. 3.9.

The GENIUSH computations utilized 15 and 100 DVR grid points along the $r$ and $\theta$ coordinates, respectively, and $100-250$ grid points along $R$ to test the convergence of the computations of the resonance states. $300-500$ GENIUSH eigenvectors were used as basis for the CAP computations. Resonance energies are expected to be accurate to better than 0.1 $cm^{-1}$, while lifetimes are thought to be computed within 5-10% of their exact values.

### 4.2.5 Stabilization computations

The eigenstates beyond the first dissociation threshold of the $Ar{\cdot}NO^+$ complex have also been analyzed with a Hermitian variational technique, the stabilization method.[96;107;108;153;154] 12 000 eigenstates were obtained in a series of 25 standard GENIUSH computations to identify certain long-lived vibrational resonances of $Ar{\cdot}NO^+$. We used this technique in its simplest form and observed the stabilization of eigenenergies by employing histogram binning with a bin size of 0.001 $cm^{-1}$. During the stabilization computations the number of DVR basis functions on the $R$ dissociation coordinate was changed between 80 and 120, proportionally with the end of the coordinate range which covered the interval between 30 and 50 bohr.

In order to have a direct comparison with the other two techniques used to identify resonance states, the focus was placed on the 20 $cm^{-1}$ window above $D_0$. A stabilization histogram was also generated in this interval from the computations described above, with a bin size of 0.01 $cm^{-1}$.

Table 4.1: Comparison of the first and last 15 bound vibrational ($J = 0$) and rovibrational ($J = 1$ and 2) energy levels, given in $cm^{-1}$, of the $Ar{\cdot}NO^+$ complex computed in full (3D vibrational and 6D rovibrational) and reduced-dimensional models (2D and 5D), where the $r$ coordinate is held fixed at its equilibrium value, using the variational GENIUSH approach and close-coupling scattering (CC) theory.

| No. | $J = 0$ | | | No. | $J = 1$ | | | No. | $J = 2$ | | |
|---|---|---|---|---|---|---|---|---|---|---|---|
| | GENIUSH | | CC | | GENIUSH | | CC | | GENIUSH | | CC |
| | 2D | 3D | | | 5D | 6D | | | 5D | 6D | |
| 1 | 96.66 | 1278.24 | | 1 | 0.20 | 0.20 | 0.20 | 1 | 0.59 | 0.59 | 0.59 |
| 2 | 78.24 | 78.53 | 78.54 | 2 | 2.48 | 2.48 | 2.48 | 2 | 2.86 | 2.87 | 2.86 |
| 3 | 95.94 | 96.80 | 96.81 | 3 | 2.48 | 2.48 | 2.48 | 3 | 2.88 | 2.88 | 2.88 |
| 4 | 151.29 | 152.29 | 152.25 | 4 | 78.43 | 78.72 | 78.73 | 4 | 9.72 | 9.72 | 9.71 |
| 5 | 158.86 | 160.12 | 160.14 | 5 | 80.84 | 81.14 | 81.14 | 5 | 9.72 | 9.72 | 9.71 |
| 6 | 178.59 | 179.63 | 179.62 | 6 | 80.85 | 81.14 | 81.15 | 6 | 78.81 | 79.10 | 79.11 |
| 7 | 213.03 | 214.69 | 214.62 | 7 | 96.13 | 96.99 | 97.00 | 7 | 81.22 | 81.51 | 81.52 |
| 8 | 222.09 | 223.14 | 223.09 | 8 | 98.31 | 99.17 | 99.17 | 8 | 81.24 | 81.53 | 81.54 |
| 9 | 233.30 | 234.65 | 234.64 | 9 | 98.32 | 99.17 | 99.18 | 9 | 88.46 | 88.75 | 88.75 |
| 10 | 254.37 | 255.54 | 255.52 | 10 | 151.48 | 152.47 | 152.44 | 10 | 88.46 | 88.75 | 88.75 |
| 11 | 270.19 | 271.66 | 271.63 | 11 | 154.02 | 155.03 | 154.99 | 11 | 96.52 | 97.38 | 97.38 |
| 12 | 283.98 | 285.47 | 285.37 | 12 | 154.03 | 155.04 | 155.00 | 12 | 98.69 | 99.55 | 99.55 |
| 13 | 288.82 | 290.01 | 289.95 | 13 | 159.05 | 160.30 | 160.33 | 13 | 98.71 | 99.56 | 99.57 |
| 14 | 302.37 | 303.81 | 303.77 | 14 | 161.39 | 162.62 | 162.65 | 14 | 105.24 | 106.08 | 106.08 |
| 15 | 321.79 | 323.10 | 323.07 | 15 | 161.40 | 162.63 | 162.65 | 15 | 105.24 | 106.08 | 106.08 |
| 186 | 876.99 | 879.63 | 879.47 | 536 | 880.92 | 883.74 | 883.53 | 845 | 881.93 | 884.55 | 884.40 |
| 187 | 878.01 | 880.36 | 880.20 | 537 | 881.45 | 884.28 | 884.08 | 846 | 882.21 | 884.56 | 884.41 |
| 188 | 878.49 | 880.96 | 880.80 | 538 | 881.83 | 884.44 | 884.19 | 847 | 882.26 | 884.85 | 884.70 |
| 189 | 879.54 | 882.12 | 881.96 | 539 | 881.84 | 884.75 | 884.60 | 848 | 882.33 | 884.86 | 884.71 |
| 190 | 879.58 | 882.47 | 882.31 | 540 | 882.05 | 884.76 | 884.61 | 849 | 882.33 | 885.09 | 884.93 |
| 191 | 879.83 | 882.76 | 882.60 | 541 | 882.21 | 885.22 | 885.11 | 850 | 882.64 | 885.09 | 884.93 |
| 192 | 880.88 | 883.69 | 883.49 | 542 | 882.53 | 885.47 | 885.37 | 851 | 882.99 | 885.27 | 885.19 |
| 193 | 881.41 | 884.24 | 884.05 | 543 | 882.96 | 885.74 | 885.78 | 852 | 883.20 | 885.55 | 885.44 |
| 194 | 881.97 | 884.39 | 884.13 | 544 | 883.23 | 885.97 | 885.90 | 853 | 883.21 | 885.79 | 885.83 |
| 195 | 882.19 | 885.20 | 885.08 | 545 | 883.24 | 886.01 | 885.95 | 854 | 883.33 | 886.09 | 886.03 |
| 196 | 882.49 | 885.44 | 885.35 | 546 | 883.40 | 886.09 | 886.08 | 855 | 883.34 | 886.16 | 886.05 |
| 197 | 882.94 | 885.91 | 886.14 | 547 | 883.73 | 886.13 | 886.42 | 856 | 883.43 | 886.19 | 886.43 |
| 198 | 883.39 | 886.29 | 886.78 | 548 | 884.06 | 886.40 | | 857 | 883.76 | 886.43 | 886.66 |
| 199 | 883.72 | 886.57 | | 549 | 884.11 | 886.66 | | 858 | 884.11 | 886.48 | |
| 200 | 884.08 | 886.84 | | 550 | 884.11 | 886.90 | | 859 | 884.16 | 886.78 | |

## 4.3 Bound rovibrational states of Ar·NO$^+$

### 4.3.1 Computational results in full and reduced dimensions

Bound vibrational ($J = 0$) and rovibrational ($J = 1$ and 2) energy levels of the Ar·NO$^+$ complex have been determined by employing both the variational GENIUSH and the Newmat scattering protocols. GENIUSH computations were performed in reduced dimensions, *i.e.*, using a one- or two-dimensional Hamiltonian, as well.

Comparison of selected bound-state energies, obtained in both 3D and 2D, is shown in Table 4.1. The agreement between the bound-state energies of the two fundamentally different approaches, GENIUSH and CC, is very good. For the lowest states, *e.g.* up to 200 cm$^{-1}$, only a few 0.01 cm$^{-1}$ deviation is observed, which increases as the energy approaches $D_0$. Near dissociation the two methods yield very slightly different results. It can also be seen from Table 4.1 that the energy levels become rather dense as the energy approaches the dissociation limit.

The $J = 1$ and 2 rovibrational energies reveal that while the Ar·NO$^+$ complex is characterized by two large-amplitude, significantly mixed vibrational motions, the complex rotates basically as a rigid rotor. This is due to the large masses of the nuclei, resulting in rotational constants of $A_\mathrm{e} = 2.4$ and $B_\mathrm{e} \approx C_\mathrm{e} = 0.1$ cm$^{-1}$, about two orders of magnitude smaller than the first vibrational excitation energy at 78.5 cm$^{-1}$.

As to the reduced-dimensional models, 2D rovibrational energies obtained from GENIUSH computations using the so-called rigid monomer approximation (RMA), *i.e.*, where the intramonomer distance $r$ is frozen to its equilibrium value, are also compared to their full-dimensional counterparts in Table 4.1. It is obvious that the 2D results capture more than the essential physics of the nuclear dynamics of Ar·NO$^+$, the deviations between the 2D and 3D energies are between 1 and 3 cm$^{-1}$, never larger than 3 cm$^{-1}$ up to 500 cm$^{-1}$. Nearer to dissociation, elimination of the NO$^+$ stretching motion from the dynamical computation seems to cause more significant differences. Thus, as expected, the energies increase upon extension from a 2D to a 3D treatment of the vibrations, which is the result of the coupling with the NO$^+$ stretching

fundamental, occurring at about 2340 $cm^{-1}$, well above the first dissociation limit of $Ar{\cdot}NO^+$ (see Table 4.2), neglected in the 2D model. In conclusion, the RMA model works very well, *i.e.*, the 2D results are almost of spectroscopic accuracy, defined as 1 $cm^{-1}$.

Table 4.2: GENIUSH vibrational energies corresponding to the $NO^+$ stretching motion from 1D ($R$ and $\theta$ are fixed to their equilibrium values) and 3D models, in $cm^{-1}$. (No. = 2036 refers to the 2036th eigenvalue.)

| 1D | | 3D | |
|---|---|---|---|
| No. | Value | No. | Value |
| 2 | 2337.1 | 2036 | 2338.2 |
| 3 | 4641.6 | 5170 | 4643.4 |
| 4 | 6912.8 | 8410 | 6914.9 |
| 5 | 9156.5 | 11726 | 9158.5 |

1D computations have also been carried out where only the $r$ coordinate is active (the $R$ and $\theta$ coordinates are held fixed at their equilibrium values), yielding the bound states of the 1D problem of the $NO^+$-stretching motion. Also, further 3D computations (as part of applying the stabilization method to this system) were performed, providing eigenvalues high above the $D_0$ dissociation limit. Inspecting Table 4.2, one can notice, that the 1D model can reproduce very accurately the 3D counterparts of the $NO^+$ stretching modes, embedded in the continuum. Identification of these 3D states is based on the analysis of their wave function plots, which are presented in Figure 4.1. As it is seen in Figure 4.1, the first and second excited states of the $NO^+$-stretching motion feature localized and clearly-structured wave functions, in contrast to those of the neighboring continuum states, showing chaotic structures.

The zero-point vibrational energy (ZPVE) of $Ar{\cdot}NO^+$ is 1278.2 $cm^{-1}$, while it is 1181.1 $cm^{-1}$ in the 1D $NO^+$ model. This means (as expected) that most of the ZPVE is in the diatomic fragment, while the other two, large-amplitude motions contribute less than 100 $cm^{-1}$ to the ZPVE of the $Ar{\cdot}NO^+$ complex. The ZPVE of the 2D RMA model is 96.7 $cm^{-1}$, showing the almost perfect 1D + 2D additivity of the 3D ZPVE.

Thus, the results of the 1D model prove once again the power of the RMA model for such a weakly-bound complex, *i.e*, that large-amplitude intermonomer vibrations can

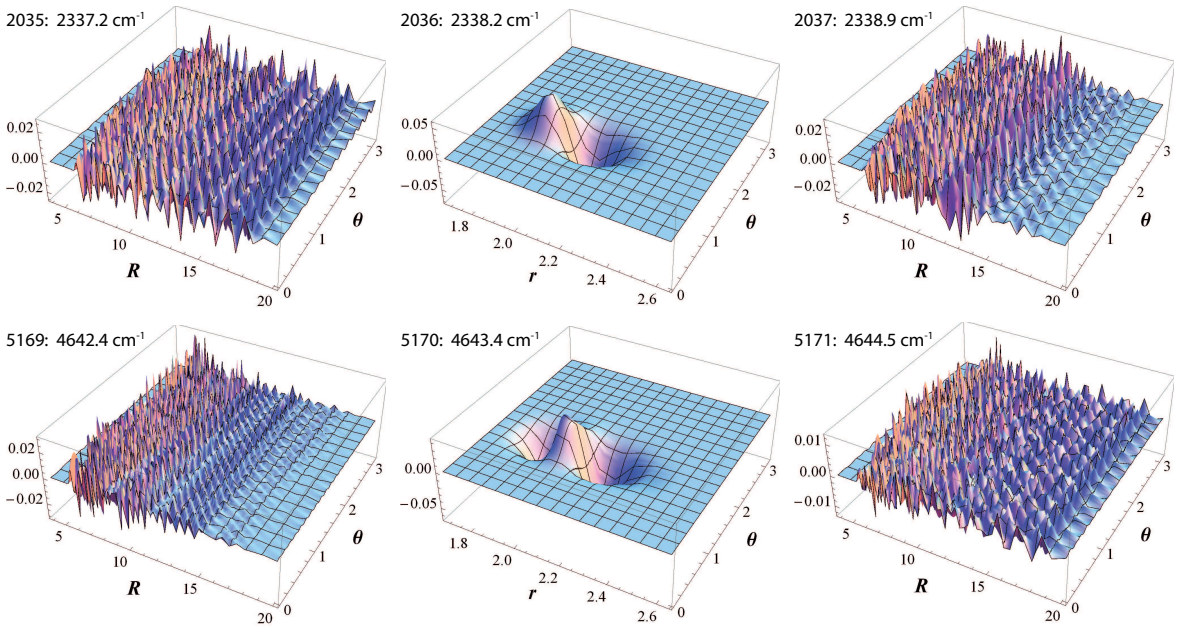


Figure 4.1: Plots of the full-dimensional eigenfunctions of the $NO^+$ stretching fundamental and its first overtone (in the middle of the figure, $r - \theta$ cuts), as well as the preceding and subsequent wave functions of the system ($R - \theta$ cuts). The two $NO^+$ stretching states can be obtained as eigenstates stabilized at energies of 2338.2 and 4643.4 $cm^{-1}$.

be almost adiabatically separated from the high-frequency intramonomer vibration.

### 4.3.2 Comparison with experiment

Vibrational progressions revealing bound-state energies of the Ar·$NO^+$ complex have been measured in the $[0, 400]$ and $[330, 720]$ $cm^{-1}$ intervals by Takahashi[134] and Bush *et al.*,[141] respectively. Comparison of these energy levels with some of the computed ones is presented in Table 4.3.

Quantum number assignments are only given in Table 4.3 for the experimental results, taken from the original references.[134;141] Quantum numbers could be assigned to the bound vibrational states via the node-counting technique I employed, however, the states show considerable mixing of the intermonomer modes, *i.e.*, the stretching $R$ and the bending $\theta$ coordinates. Assigning stretching ($n_s$) and bending ($n_b$) quantum numbers to the computed states is thus rather ambiguous in almost all cases. Furthermore, the stretching and bending progressions "established" experimentally cannot be clearly followed. Nevertheless, pairing of experimental and computed energy levels is based

Table 4.3: Experimental (expt) vibrational energy levels of Ar·$NO^+$ and their computed counterparts, in $cm^{-1}$, obtained with the GENIUSH (GEN) and the close coupling scattering (CC) techniques in reduced (2D) and full (3D) dimensions, relative to the ZPVE. $n_s$ and $n_b$ denote the experimentally determined stretching and bending quantum numbers, respectively.[134;141]

| No. | 2D | 3D | | Experiment | |
|---|---|---|---|---|---|
| | $E_{GEN}$ | $E_{CC}$ | $E_{GEN}$ | $E_{expt}$ | $n_s$ $n_b$ |
| 1 | 0.0 | 0.0 | 0.0 | 0.0 | 0 0 |
| 2 | 78.1 | 78.5 | 78.5 | 79 ± 2 | 0 1 |
| 3 | 95.9 | 96.8 | 96.8 | 94 ± 2 | 1 0 |
| 4 | 151.3 | 152.3 | 152.3 | 155 ± 2 | 0 2 |
| 6 | 178.6 | 179.6 | 179.6 | 178 ± 2 | 2 0 |
| 9 | 233.3 | 234.6 | 234.7 | 230 ± 2 | 0 3 |
| 10 | 254.4 | 255.5 | 255.5 | 256 ± 2 | 3 0 |
| 16 | 327.5 | 328.8 | 328.9 | 328 ± 2 | 4 0 |
| 23 | 396.0 | 397.4 | 397.4 | 391 ± 2 | 5 0 |
| 29 | 439.6 | 441.0 | 441.1 | 440 ± 2 | 0 6 |
| 30 | 445.3 | 446.6 | 446.7 | 451 ± 2 | 6 0 |
| 38 | 488.8 | 490.3 | 490.4 | 484 ± 2 | 1 5 |
| 40 | 502.5 | 503.7 | 503.7 | 500 ± 2 | 0 7 |
| 41 | 504.1 | 505.5 | 505.6 | 509 ± 2 | 7 0 |
| 47 | 536.9 | 538.3 | 538.4 | 531 ± 2 | 6 1 |
| 49 | 544.6 | 546.1 | 546.2 | 541 ± 2 | 1 6 |
| 51 | 556.8 | 557.9 | 558.0 | 558 ± 2 | 0 8 |
| 58 | 585.8 | 587.2 | 587.3 | 583 ± 2 | 7 1 |
| 61 | 597.1 | 598.8 | 598.9 | 596 ± 2 | 1 7 |
| 64 | 610.0 | 611.4 | 611.5 | 609 ± 2 | 0 9 |
| 70 | 631.7 | 633.1 | 633.2 | 631 ± 2 | 8 1 |
| 78 | 660.3 | 661.9 | 661.9 | 656 ± 2 | 10 0 |
| 85 | 683.0 | 684.8 | 684.9 | 680 ± 2 | 9 1 |
| 92 | 705.9 | 707.3 | 707.5 | 700 ± 2 | 11 0 |
| 97 | 718.5 | 720.0 | 720.1 | 722 ± 2 | 10 1 |

mainly on the structure of the wave functions plotted along the two intermonomer coordinates. They show, in most cases, a somewhat clearer excitation pattern regarding the pure excitations along either the $R$ or the $\theta$ coordinate, that is when either of the intermonomer stretching or bending quantum numbers have zero value.

Thus, while a qualitative interpretation of the measured progressions appears to be challenging, the computed vibrational energies do support the observed transitions in a quantitative way, see Table 4.3.

## 4.4 Resonance states of the Ar·NO$^+$ complex

### 4.4.1 Quasi-bound states high above the first dissociation limit

In this Section a text-book example of Feshbach resonances, introduced in Section 2.3.1, is presented. As discussed in Section 2.3.1, Feshbach resonances occur when the bound states of a system, characterized by an unperturbed Hamiltonian operator, are embedded in the continuum part of the spectrum of this operator, and due to coupling with this continuum, *i.e.*, a "perturbation", they become metastable. Let us present, how this is realized in the case of a weakly-bound van der Waals complex.

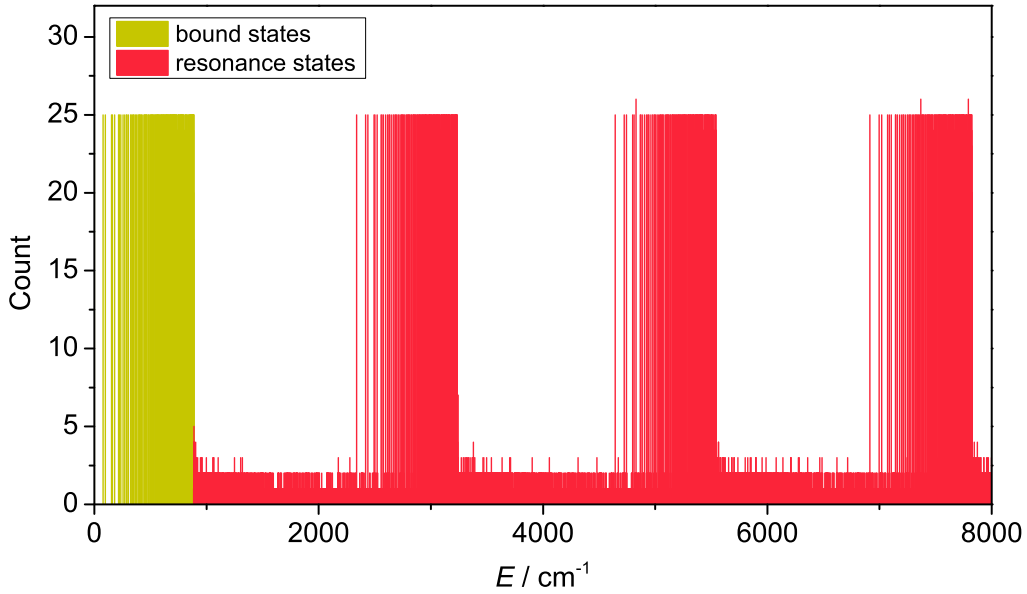


Figure 4.2: Overview of the stabilization-method histogram in the 0–8000 cm$^{-1}$ energy interval based on 25 individual GENIUSH computations.

Stabilization computations for Ar·NO$^+$ reveal an interesting repetitive pattern well above the first dissociation threshold of the complex. The overview of the stabilization

histogram, based on 25 individual GENIUSH computations and binned using a bin size of 0.001 $cm^{-1}$, covering the $[0-8000]$ $cm^{-1}$ interval is shown in Figure 4.2. Green color denotes bound states, while red refers to resonance states. The green stack, consisting of bound states, has a well-defined upper limit, corresponding to $D_0$. The three further stacks between $2300-3200$, $4600-5500$, and $6900-7800$ $cm^{-1}$ exhibit pronounced similarity with the stack corresponding to the bound states. They start at the first, second, and third excited $NO^+$ stretching states and the width of the stacks is approximately $D_0$. As we have seen above, the excited $NO^+$ stretching modes could be precisely identified by their localized and informative wave functions among the continuum states in 3D GENIUSH computations (see Figure 4.1 and Table 4.2).

Thus, the reason for these states emerging clearly above the first dissociation limit, with maximal count numbers in the stabilization histogram meaning that in all individual computations the corresponding energy falls into a 0.001 $cm^{-1}$-wide bin, is that they resemble very much to the bound states of the complex shifted by the excitation energies of the $NO^+$-stretching mode. This is also supported by their localized nature in the interaction region of the potential.

Consequently, one is invited to notice, that these states are the bound states of the unperturbed Hamiltonian describing the stretching motion of the $NO^+$ diatomic molecule, and the vibrations along the $R$ and $\theta$ coordinates. Due to the perturbation terms in the full Hamiltonian, *i.e.*, the intermonomer-interaction and the kinetic energy terms corresponding to the relative motion of the monomers, they become coupled to the surrounding continuum, and so they become metastable. In fact, the discrete states with $NO^+$ in $v = 1$, where $v$ is the vibrational quantum number of the $NO^+$ diatom, and the intermonomer modes in a specific bound vibrational state are coupled to the continuum states of the intermonomer modes with $NO^+$ being in $v = 0$. In other words, the coupling to the intermonomer vibrations makes possible the decaying of these states in time, due to the opening of a decaying channel at the first dissociation energy of the Ar·$NO^+$ complex, which is much lower than that of $NO^+$. This new channel allows for the excess energy stored in the $NO^+$-vibration to "leak" through this coupling, thus forcing the $NO^+$-stretching states (and the states corresponding to intermonomer excitations superimposed on them) to have finite lifetimes.

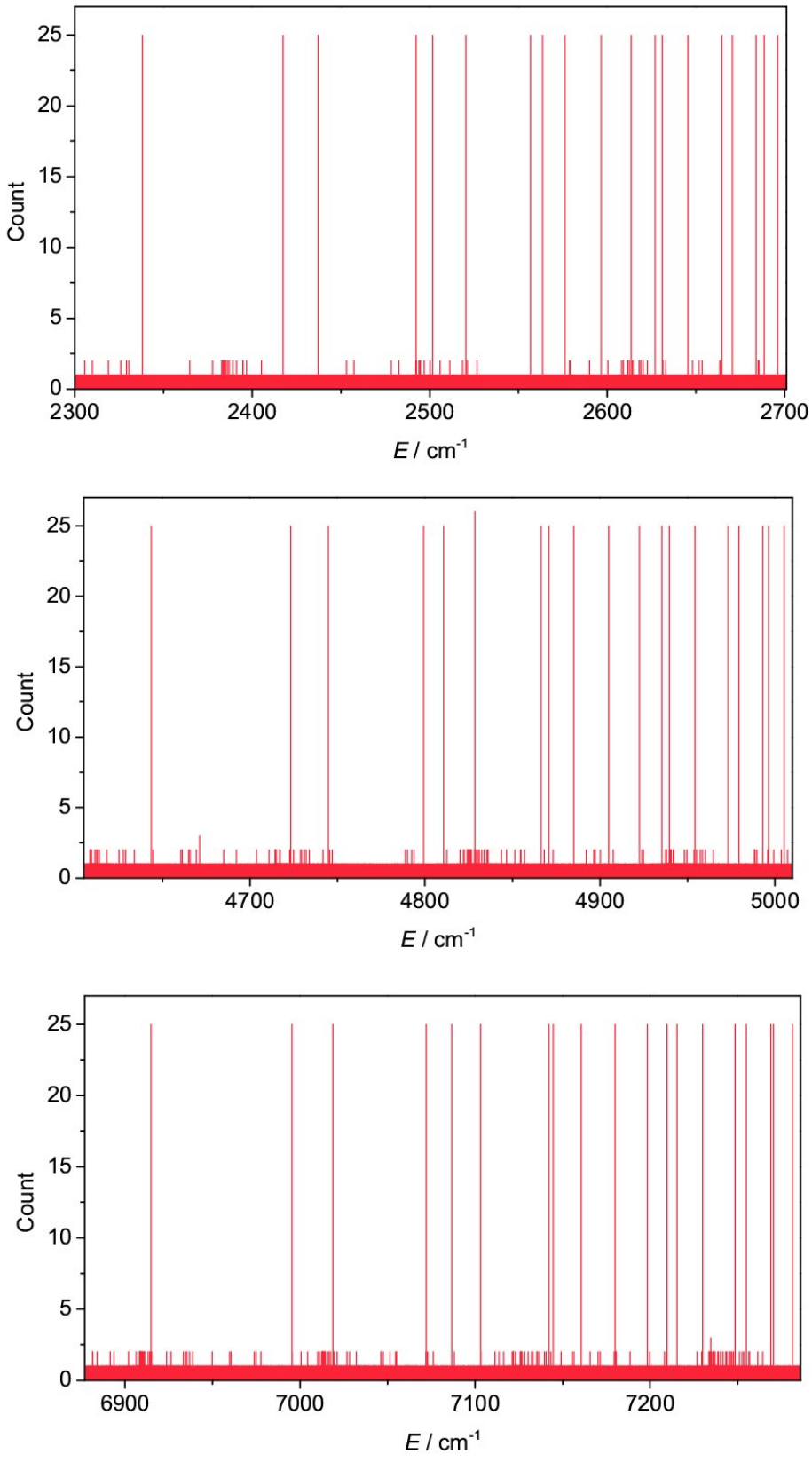


Figure 4.3: Stabilization-method histograms covering 400 $cm^{-1}$ above the $NO^+$-stretching fundamental (top panel) and its first (middle panel) and second (bottom panel) overtones, obtained from 25 GENIUSH computations. All three panels show 19 long-lived resonances.

Since, as seen above, the coupling is very weak between the small-amplitude $NO^+$-stretching and the large-amplitude intermonomer motions, these bound states are only slightly "perturbed", and as such turn into very long-lived resonance states.

If we zoom into the stacks located above the dissociation threshold, see Figure 4.3, a very similar pattern of long-lived resonance states appear at the beginning of each stack, starting with the first, second and third excited $NO^+$-stretching state. The wave functions of the states on top of the $NO^+$-excited levels feature exactly the same intermonomer stretching and bending excitation patterns as the corresponding bound states, in line with the intuitive assumption described above. As an illustration, Figure 4.3 shows the first 19 resonances superimposed on the excited $NO^+$ levels, all covering a 400 $cm^{-1}$ interval.

In summary, the stabilization method has been very successful in identifying the characteristic energy pattern of long-lived Feshbach resonance states of the Ar·$NO^+$ complex. Such a clear pattern could be formed because of the adiabatic separation of the intramonomer motion from the other internal degrees of freedom of the system. It is emphasized that in the case of such a weakly-bound complex, the stabilization method can yield accurate resonance energy levels high above the first dissociation threshold.

### 4.4.2 Low-lying vibrational resonances

In order to compare the GENIUSH-CAP results to those of scattering resonance computations, a suitable energy range, *i.e.*, the $[D_0, D_0 + 20]$ $cm^{-1}$ window, has been chosen. Since the close coupling (CC) cross sections proved to be very complicated due to the very rich and overlapping resonance structure of the Ar·$NO^+$ complex at higher energies, and also because of the subtility of the GENIUSH-CAP trajectories in those regions, the energy interval just above the first dissociation limit seemed to be a convenient choice for comparison.

For an adequate comparison one has to find the common language between the two different methods. It should be kept in mind that the GENIUSH-CAP computations provide energies for a given value of $J$, which is the total angular momentum quantum

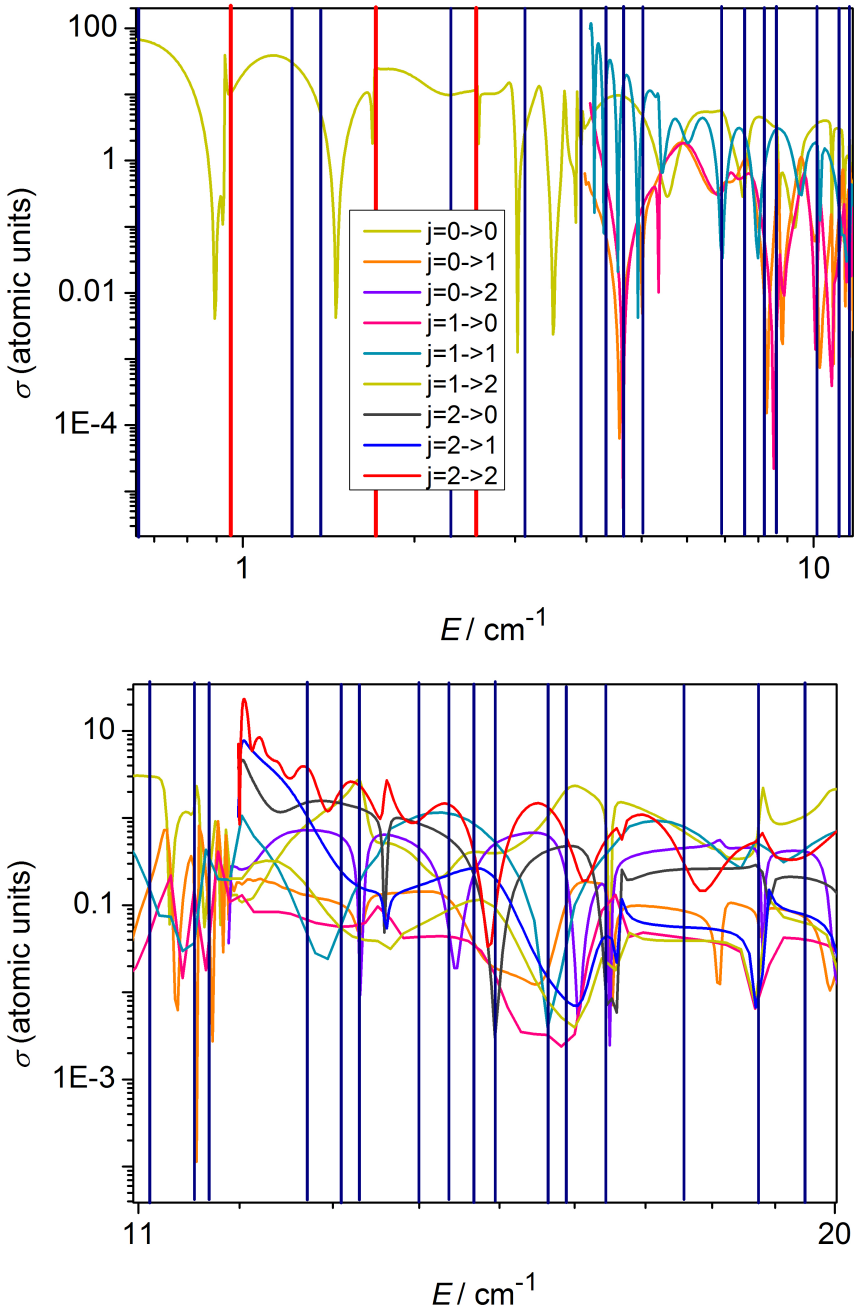


Figure 4.4: $J = 0$ component of the $j = 0, 1, 2 \rightarrow j' = 0, 1, 2$ cross sections as a function of the total energy on a logarithmic scale. Blue vertical lines denote energies at which resonances are found in GENIUSH-CAP computations. The red vertical lines emphasize the large peaks of the stabilization method histogram of Fig. 4.6. The zero of energy is taken for Ar far from $NO^+(v = 0, j = 0)$.

number, however, these computations include all the possible values of $j$ and $l$ as $|j - l| \leq J \leq j + l$, where $j$ is the rotational quantum number of the $NO^+$ unit, while $l$ characterizes the relative rotation of the two monomers in the complex. In contrast, in CC computations the state-to-state cross sections, characterized by initial and final

states corresponding to given $j$ and $l$ values, are obtained for all the transitions between the populated ro-vibrational states of $NO^+$, including several $J$ values. Thus, the $J = 0$ components of these cross sections should be compared to GENUSH-CAP results, as it is illustrated for the low-lying resonances of the Ar·$NO^+$ complex in Figure 4.4.

In the $J = 0$ case, if one chooses a given initial rotational state of $NO^+$, $j$, one also fixes the value of $l$, which thus must equal $j$. Thus, the resonances appearing on the $J = 0$ component of the inelastic cross sections starting from the rotational state $j = 0$ of $NO^+$ are associated with $l = 0$ and are then Feshbach resonances, in a sense that in such cases no rotational excitation occurs either in the $NO^+$ unit or in relative orientation of the monomers.

With the above considerations in mind, Figure 4.4 shows $j = 0, 1, 2 \rightarrow j' = 0, 1, 2$ cross sections, since the $j = 1$ and $j = 2$ rotational states open in the $[D_0 - 20]$ $cm^{-1}$ energy interval. In Figure 4.4 the resonance positions obtained from GENIUSH-CAP are denoted by vertical blue and red lines, while the energy positions and widths of the peaks in the state-to-state cross sections drawn as a function of energy define roughly the CC resonance energies and widths. As it can be seen from Figure 4.4 all significant CC peaks can be paired with GENIUSH-CAP resonance energies within a few 0.1 $cm^{-1}$. With GENIUSH-CAP the resonance states at 3.9 and 11.6 $cm^{-1}$ have been successfully identified to be related to the opening of the $j = 1$ and 2 channels, which occur at 3.9 and 11.9 $cm^{-1}$ in the cross sections. Due to the logarithmic scale, at very low energies even extremely small shifts can be observed. If one fitted, *e.g.*, the Breit-Wigner formula to a single cross section curve, the obtained resonance properties would slightly differ from the positions and width of the different curves shown in Figure 4.4. However, because of the complicated resonance structure of Ar·$NO^+$ this task has not been carried out. Taking into account the complex dynamical behavior of the system studied and the fundamental differences of the two techniques, it is the expected quality of the agreement between the results of the two approaches. To the best of my knowledge, such a comparison, apart from this work,[22] has not yet been published in the literature.

To further complement the comparison between the GENIUSH-CAP and the CC resonance computations, lifetimes of resonance states obtained from the two ap-

proaches were also paired, as presented in Figure 4.5. As can be seen in Figure 4.5, the positions of the longer-lived resonances are in good agreement. GENIUSH-CAP resonance energies and lifetimes are listed in Table 4.4, where the longest-lived resonances are boldfaced.

Table 4.4: Resonance energies ($E$, in $cm^{-1}$) and lifetimes (in ns) obtained from GENIUSH-CAP computations. These resonance energies are denoted with blue and red lines in Fig. 4.4.

| $E$ | Lifetime | $E$ | Lifetime | $E$ | Lifetime |
|---|---|---|---|---|---|
| 0.5 | 0.43 | 5.1 | 0.51 | 13.3 | 0.02 |
| 0.7 | 0.41 | 7.0 | 0.02 | 14.0 | 0.02 |
| **1.0** | **11.19** | 7.6 | 0.09 | 14.4 | 0.01 |
| 1.3 | 0.03 | 8.2 | 0.01 | 14.7 | 0.01 |
| 1.4 | 0.03 | 8.7 | 0.55 | 15.0 | 0.01 |
| **1.7** | **2.35** | 10.2 | 0.55 | 15.7 | 0.05 |
| 2.4 | 0.02 | 11.1 | 0.23 | 15.9 | 0.04 |
| **2.6** | **33.61** | 11.6 | 0.30 | 16.5 | 0.25 |
| 3.2 | 0.05 | 11.7 | 0.08 | 17.6 | 0.31 |
| 4.3 | 0.08 | 12.8 | 0.04 | 18.8 | 0.37 |
| 4.7 | 0.27 | 13.1 | 0.08 | 19.5 | 0.09 |

To explore more thoroughly the $[D_0, D_0 + 20]$ $cm^{-1}$ energy window chosen to investigate low-lying resonance states of Ar·$NO^+$, we also inspected the stabilization histogram of this region. Histograms were constructed in this energy interval by employing a 0.01 $cm^{-1}$ bin size, shown in Figure 4.6. A "higher resolution" of 0.001

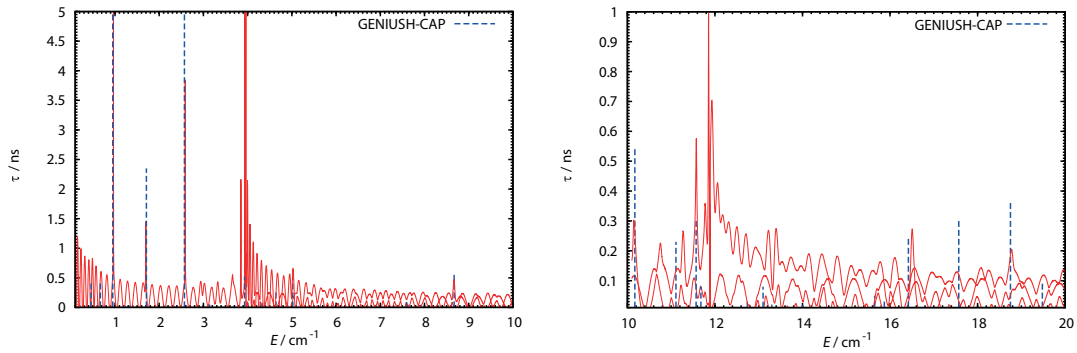


Figure 4.5: Comparison between the $J = 0$ resonance energies and lifetimes determined with the GENIUSH-CAP method and those obtained from the close coupling computations. The zero of energy is taken for Ar far from $NO^+(v = 0, j = 0)$.

$cm^{-1}$ bin size did not provide any valuable insights. In Figure 4.6 one can spot three significant peaks, which correspond to long-lived resonances in this region. These resonance states have been confirmed by both the CC ad GENIUSH-CAP computations, as seen in Figure 4.5. These are the three longest-lived states in this region, according to GENIUSH-CAP, see data in Table 4.4. The corresponding resonance energies are highlighted as red lines in Figure 4.4.

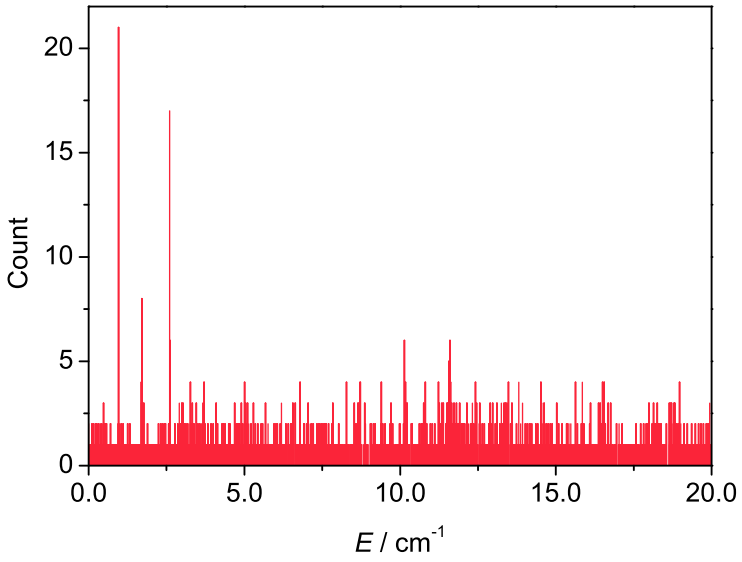


Figure 4.6: Stabilization-method histogram, bin size of 0.01 $cm^{-1}$ , of the energy range 20 $cm^{-1}$ above the first dissociation limit, $D_0$. Eigenvalues are obtained from 25 GENIUSH computations.

## 4.5 Concluding remarks

Studying the internal dynamics of the Ar·$NO^+$ van der Waals complex has revealed several interesting features of this system. Ar·$NO^+$ was chosen to compare scattering and variational techniques, two fundamentally different approaches used to obtain stationary rovibrational states of a system. Comparison of the bound energy levels, computed with the two techniques, showed excellent agreement. Reduced-dimensional computations revealed the almost perfect separation of the large-amplitude intermolecular vibrations from the small-amplitude stretching vibration of $NO^+$. The agreement between the computed bound vibrational energies with the limited experimental information available was also good.

Then, I investigated the resonance structure of $Ar{\cdot}NO^+$ in detail. First, with the Hermitian stabilization method, which revealed an interesting pattern of energy levels high above the first dissociation threshold of the complex. These states have been assigned as Feshbach resonances, *i.e.*, originally bound states embedded in the continuum. Such a clear pattern in the stabilization histogram further proved the adiabatic separation of the intra- and intermonomer vibrations.

The low-lying vibrational resonances of the $Ar{\cdot}NO^+$ complex have been studied in a variety of ways: with the close coupling scattering technique and with the variational GENIUSH-CAP and stabilization methods. All three complementary methods provided results in good agreement. Long-lived resonance states have been identified with all three methods, and several shorter-lived ones have also been found with the scattering and the variational GENIUSH-CAP techniques.

# Chapter 5

# The resonance-state structure of $H_2He^+$

## 5.1 The $H_2He^+$ molecule

Our choice of the $H_2He^+$ system was inspired by its astrophysical importance and the widespread interest of such weakly-bound triatomic molecules. H and He are the most abundant elements of the universe, and as such their complexes of various stoichiometry are of wide interest in studying chemical processes that may occur in space.[155–157] $H_2He^+$ is also known to be an important collisional complex during the reactive scattering processes of $H_2^+$ + He, $H_2$ + $He^+$ and $HHe^+$ + H. Being a stable molecule in the primordial gas and in the interstellar medium,[158–160] even more stable than $HeH^+$,[161] means that $H_2He^+$ is a potential precursor in the formation of H, $H^+$, He, $He^+$, $H_2^+$ and $HeH^+$.[161]

Light-induced dynamics of $H_2He^+$, also of great relevance in astrochemistry, have recently been investigated in detail,[29;30] and the significance of the resonance states in the deexcitation processes has been revealed.[29] Therefore, detailed knowledge of the resonance states of $H_2He^+$ is of fundamental importance. Such quasi-bound states also play an important role in the barrierless reaction H + $HeH^+ \rightarrow H_2^+$ + He.[162;163]

Compared to the Ar·$NO^+$ complex studied in the previous chapter, one can also be

curious if a more "quantum-like" system, *i.e.*, consisting of much lighter atoms such as $H_2He^+$, features a similar, almost adiabatic decoupling of the intra- and intermonomer degrees of freedom.

## 5.2 Computational details

### 5.2.1 The potential energy surface

The nuclear motions of the $H_2He^+$ complex can be well represented by the orthogonal Jacobi coordinates, where $r$ denotes the distance between the two H atoms, $R$ refers to the distance between the center of mass of the H atoms and the He atom, and $\theta$ is the included angle of the two vectors. For the nuclear motion computations on $H_2He^+$ the PES of Ref. 164 was employed. This PES has dissociation thresholds of $D_e = 2733.66$ cm$^{-1}$ and $D_0 = 1775.32$ cm$^{-1}$, and it supports 16 vibrational states below $D_0$. The equilibrium structure of the $H_2He^+$ complex is linear, with $r_{eq} = 2.07792$ bohr and $R_{eq} = 2.96596$ bohr.

### 5.2.2 Details of the GENIUSH-CAP computations

I have found and analyzed several resonance states of the $H_2He^+$ system employing the GENIUSH-CAP program. Prior to the GENIUSH-CAP computations, GENIUSH bound states had to be computed. In the GENIUSH vibrational bound-state computations 40 and 200 scaled Laguerre-DVR points were used along the $r$ and $R$ coordinates in the ranges of $[1.0, 5.0]$ and $[0.5, 40.0]$ bohr, respectively. On the angular coordinate 40 unscaled Legendre-DVR points were employed in the interval of $(0.0, 180.0)^\circ$. The convergence of the bound-state energies, presented in Table 5.2, see below, is better than 0.01 cm$^{-1}$ with respect to the number of basis functions being increased by 20 % on each coordinate. During the nuclear-motion computations the following atomic masses were used: $m_H = 1.00727647$ u and $m_{He} = 4.00234755$ u.

For the GENIUSH-CAP computations 400 vibrational GENIUSH eigenvectors were used as a basis. During these computations the interval of $R$, where the CAP is

switched on, *i.e.*, the CAP-active interval, was taken to be either [10,40], [20,40] or [30,40] bohr. Further GENIUSH-CAP computations were carried out using the GENIUSH eigenvectors obtained during the stabilization method calculations, see Section 5.2.4, with the maximum $R$ value of 50 bohr. In this case, the CAP-active interval was changed between 10 and 50 bohr, using the same step size of 10 bohr, and 1500 GENIUSH eigenvectors were used as basis for CAP computations. The $\eta$ CAP-strength parameter was varied through many orders of magnitude, *i.e.* from $10^{-9} - 10^{-2}$

. The results presented were obtained utilizing the highest order polynomial of Ref. 111 as the functional form of the CAP. The resonance eigenvalues, both their real and imaginary parts, are usually converged within a few 0.1 $cm^{-1}$; however, this convergence strongly depends on the given resonance.

### 5.2.3 D$^2$FOPI-CCS computations

The D$^2$FOPI-CCS[5] technique employs the complex coordinate scaling method linked to the D$^2$FOPI triatomic bound-state-computing program.[72] As being necessary for D$^2$FOPI-CCS computations, bound vibrational states of the $H_2He^+$ system were also computed with the D$^2$FOPI code. For these computations 40 potential-optimized (PO) spherical-DVR basis functions[72] along the $r$ coordinate, 180 PO spherical-DVR basis functions along the $R$ coordinate, and 40 Legendre functions along the $\theta$ coordinate were employed. The coordinate ranges used in the computations are (0.0, 5.0) bohr for $r$, (0.0, 40.0) bohr for $R$, and (0.0, 180.0)° for $\theta$. The bound states obtained with GENIUSH and with D$^2$FOPI are the same within numerical accuracy.

In the D$^2$FOPI-CCS computations, resonance eigenstates were obtained by diagonalizing the complex-coordinate-scaled rovibrational Hamiltonian using 40 different values for the scaling parameter, which changed from 0 to 0.8 with a step size of 0.02. To find resonance states, cusps were identified in the resulting complex eigenvalue trajectories. Details of this approach can be found in Ref. 5. For constructing the matrix representation of the CCS Hamiltonian, 500 vibrational D$^2$FOPI eigenvectors were used. The convergence of D$^2$FOPI-CCS resonance eigenvalues is between 0.01 $cm^{-1}$ and 1 $cm^{-1}$, depending on the resonance state. D$^2$FOPI and D$^2$FOPI-CCS

computations were carried out by Dr. Tamás Szidarovszky.

### 5.2.4 Stabilization computations

In order to further study the resonance states of the $H_2He^+$ molecule, two sets of stabilization computations were performed with GENIUSH. In the first set, the range of the $R$ coordinate, $[0.5, R_{\max}]$ bohr, was changed in the interval of $R_{\max} \in [32.0, 38.0]$ bohr, applying a step size of 0.5 bohr and a proportional change in the number of basis functions between 146 and 174 along $R$; thus, in this first set 13 individual computations were performed determining 1500 eigenvalues. All other parameters were the same as in the other GENIUSH bound-state computations, see Section 5.2.2.

In the second set of stabilization computations the $R$ interval was enlarged and the $R_{\max} \in [49.0, 51.0]$ bohr range was chosen with a step size of 0.1 bohr and 1 basis function starting with 190 basis functions along $R$. This way 21 computations were performed, and 2000 eigenvalues, covering the same energy range as in the previous set, were determined.

The results of these computations were depicted on stabilization histograms, which were generated using a bin size of 0.05 $cm^{-1}$ for both of the above sets. In these histograms outstanding peaks refer to converged eigenvalues above dissociation, and therefore to resonance energies.[96;107]

## 5.3 Comparison of non-Hermitian techniques

Since the complex coordinate scaling method does not involve approximations (apart from utilizing a finite basis) regarding the resonance energy,[1] it is a perfect test to compare its results to those of the CAP technique. Thus, I have carried out this comparison between resonance energies and lifetimes of the $H_2He^+$ system with the corresponding results provided by the $D^2$FOPI-CCS program.

Resonance eigenvalues, both the real and imaginary parts, obtained from the two different methods show remarkably good agreement, as it is transparent from Table 5.1.

Table 5.1: Long-lived GENIUSH-CAP resonance energies, both real ($\mathrm{Re}(E_{\mathrm{res}})$) and imaginary ($\mathrm{Im}(E_{\mathrm{res}})$) parts ($\mathrm{cm}^{-1}$), and lifetimes (ps) paired with those obtained from D$^2$FOPI-CCS computations up to 3000 $\mathrm{cm}^{-1}$.

| GENIUSH-CAP | | | D$^2$FOPI-CCS | | |
|---|---|---|---|---|---|
| $\mathrm{Re}(E_{\mathrm{res}})$ | $\mathrm{Im}(E_{\mathrm{res}})$ | lifetime | $\mathrm{Re}(E_{\mathrm{res}})$ | $\mathrm{Im}(E_{\mathrm{res}})$ | lifetime |
| 1775.8 | −0.05 | 311.5 | 1775.9 | $> -0.005^a$ | $> 3335.6$ |
| 1776.7 | −0.20 | 82.6 | 1777.0 | −0.13 | 128.3 |
| 1778.3 | −0.41 | 40.7 | 1779.8 | −0.43 | 38.8 |
| 1809.0 | −0.00 | 112357.9 | 1809.0 | $> -0.0001^a$ | $> 166781.7$ |
| 1822.6 | −0.06 | 278.0 | 1822.6 | −0.06 | 273.4 |
| 1832.0 | −0.00 | 26685.1 | 1832.0 | $>0^a$ | |
| 1834.2 | −0.07 | 252.3 | 1834.2 | $> -0.04^a$ | $> 417.0$ |
| 1835.2 | −0.21 | 78.5 | 1835.5 | −0.13 | 128.3 |
| 1838.6 | −0.40 | 41.7 | 1838.1 | −0.40 | 41.7 |
| 1950.4 | −0.08 | 198.1 | 1950.7 | $> -0.02^a$ | $> 833.9$ |
| 1951.4 | −0.22 | 76.2 | 1951.8 | −0.23 | 72.5 |
| 1954.7 | −0.61 | 27.5 | 1954.3 | −0.72 | 23.2 |
| 2123.7 | −0.12 | 140.5 | 2123.6 | −0.13 | 128.3 |
| 2124.8 | −0.25 | 65.7 | 2125.6 | −0.22 | 77.6 |
| 2128.1 | −0.62 | 26.7 | 2127.8 | −0.55 | 30.3 |
| 2352.5 | −0.16 | 104.2 | 2352.0 | $> -0.22^a$ | $> 75.8$ |
| 2353.9 | −0.31 | 53.8 | 2354.8 | −0.38 | 43.9 |
| 2491.9 | −0.91 | 18.3 | 2491.9 | −1.11 | 15.0 |
| 2602.8 | −0.72 | 23.2 | 2602.9 | −0.87 | 19.3 |
| 2635.1 | −0.21 | 79.4 | 2635.1 | −0.36 | 47.0 |
| 2636.7 | −0.38 | 43.9 | 2638.0 | −0.45 | 37.1 |
| 2642.4 | −0.54 | 30.9 | 2642.2 | −0.58 | 28.8 |
| 2969.6 | −0.27 | 61.8 | 2969.5 | $> -0.50^a$ | $> 33.4$ |
| 2973.3 | −0.66 | 25.2 | 2972.9 | −0.50 | 33.4 |
| 2978.3 | −0.56 | 29.8 | 2978.3 | −0.80 | 20.8 |

[a] To find the position of the resonance eigenvalue more exactly was not feasible.

Table 5.1 lists all the long-lived resonance eigenvalues, *i.e.* those having an imaginary part greater than $-1$ $\mathrm{cm}^{-1}$, of $H_2He^+$ in the energy interval $[D_0, 3000]$ $\mathrm{cm}^{-1}$. The two methods usually yield resonance energies within a few 0.1 $\mathrm{cm}^{-1}$, and even the obtained lifetime values, which are usually very difficult to converge, are in the same order of magnitude.

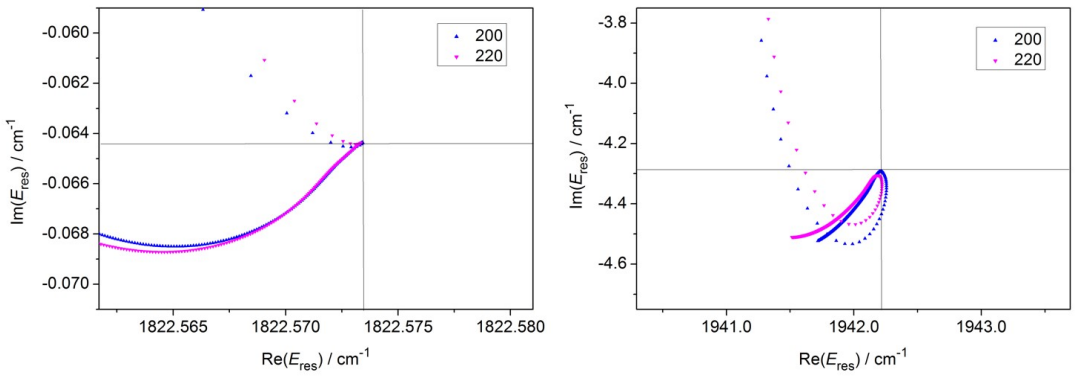


Figure 5.1: GENIUSH-CAP eigenvalue trajectories of two selected resonance states of the $H_2He^+$ system, corresponding to the wave function plots of Figure 5.2. Blue and pink triangles refer to 200 and 220 basis functions along the $R$ dissociation coordinate in the GENIUSH bound-state computations, respectively.

Overall, the excellent agreement of the GENIUSH-CAP and D$^2$FOPI-CCS results prove the correctness of the implementation of the CAP technique within GENIUSH.

## 5.4 Characterizing resonance states

Figure 5.1 presents two selected GENIUSH-CAP eigenvalue trajectories, with different colors referring to different basis set sizes, 200 and 220 DVR points, used along the $R$ dissociation coordinate in the GENIUSH bound-state computations. The left panel of Figure 5.1 reveals that the cusp in the CAP eigenvalue trajectory covers a very narrow energy range; thus, both the lifetime and the energy of this resonance state can be determined very precisely. In contrast, the right panel of Figure 5.1 shows a cusp covering a broader energy range, that is a few 0.1 cm$^{-1}$, which allows for a somewhat lower precision. This behavior is probably closely related to the localized or delocalized nature of the resonance states, as discussed below.

A powerful analysis tool I have developed and linked to GENIUSH-CAP is the automatic visualization of the resonance wave functions, obtained by plotting the square of the absolute values of the complex eigenvectors of the CAP-modified Hamiltonian, corresponding to the cusp energies.

Figure 5.2 shows the 2D cuts of the wave functions of the two resonance states presented in Figure 5.1. In each case the third coordinate is held fixed at its equilibrium

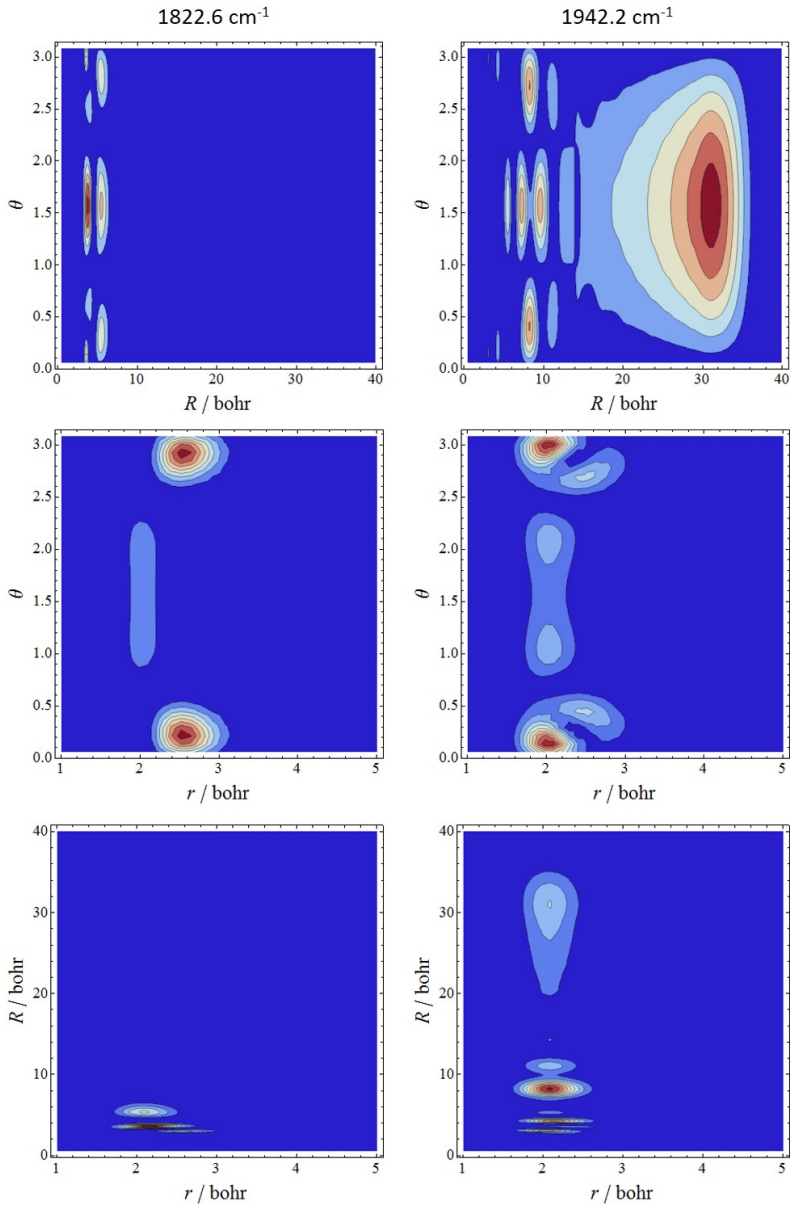


Figure 5.2: 2D GENIUSH-CAP wave function plots (the third coordinate is held fixed at its equilibrium value) of two resonance states of $H_2He^+$ corresponding to the resonance energies of Figure 5.1. In both cases the CAP is switched on between 35-40 bohr along the $R$ dissociation coordinate. $r$ and $R$ coordinates are given in bohr, $\theta$ is given in radian.

value. The left panels of Figure 5.2 reveal that the wave function of the resonance state at the energy of 1822.6 $cm^{-1}$ is localized in the potential well along the $R$ dissociation coordinate. This is supported by the fact that this resonance could be identified even when the CAP was switched on, and thereby the resonance wave function was damped, in the 20-40 bohr range along $R$. In contrast, the dominant part of the wave function corresponding to the resonance state at 1942.2 $cm^{-1}$ is extended along the $R$-coordinate until it is damped by the CAP, at 35 bohr. Due to this delocalized nature,

the $L^2$ expansion of this resonance state is less effective than that of the previous one. This is probably the reason why its trajectory features a less "sharp" cusp. Also, the dominance of the wave function in the asymptotic region indicates that this resonance is a "less bound" state, which is also reflected by its shorter lifetime when compared to the resonance state at 1822.6 $cm^{-1}$. Due to its shorter lifetime (having an imaginary part $-$ 4.3 $cm^{-1}$, and therefore a lifetime of 4 ps) this state is not listed in Table 5.1.

Inspecting further the wave functions of Figure 5.2 reveals that neither resonance states is excited in the HH-stretching motion (they show no nodes along the $r$ coordinate); however, both feature excitations in the intermolecular bending motion. The $R$ intermolecular stretching mode is only doubly excited in the interaction region for the state at 1822.6 $cm^{-1}$, but, not surprisingly, it is highly excited for the resonance with the energy of 1942.2 $cm^{-1}$.

## 5.5 Patterns in the resonance energy-level structure of $H_2He^+$

### 5.5.1 Bound states as resonances

In Table 5.1 two extremely long-lived states can be spotted at the resonance energies of 1809.0 and 1832.0 $cm^{-1}$. These states have lifetimes several orders of magnitude longer than the other resonances in the region. The stabilization histograms, presented in Figure 5.4 and analyzed later in detail, also show two peaks with large count numbers at these energies. Inspecting the wave functions of the two long-lived states, shown in the upper two panels of Figure 5.3, obtained from a GENIUSH computation with $R_{\max} = 50$ bohr, reveals that they are antisymmetric in the $\theta$ coordinate. Therefore these states correspond to the $B_2$ irreducible representation of the $C_{2v}$(M) molecular symmetry group. Such symmetry classifications reflect the behavior of the spatial part of the wave functions with respect to the exchange of the two identical atoms. For example, wave functions of $B_2$ symmetry change sign upon the exchange of the two H atoms, while wave functions of $A_1$ symmetry do not.

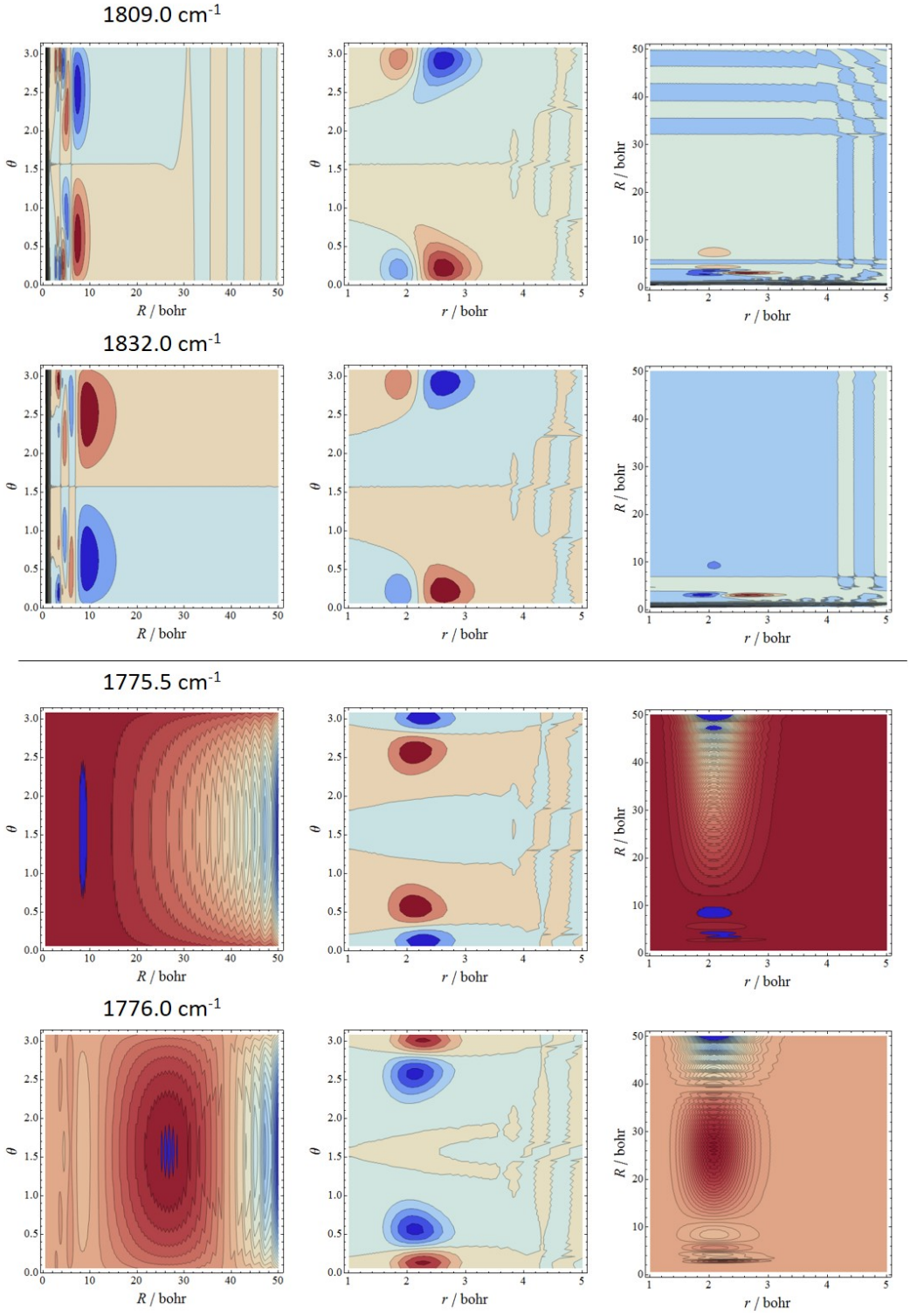


Figure 5.3: 2D GENIUSH wave function plots of four long-lived resonance states of the $H_2He^+$ molecular ion at the energies of 1809.0, 1832.0, 1775.5, and 1776.0 $cm^{-1}$, obtained from the stabilization computation utilizing $R_{max} = 50$ bohr. The wave functions of the upper two panels transform according to $B_2$ symmetry, as reflected by the antisymmetry of their wave functions along the $\theta$ Jacobi coordinate. The wave functions shown in the lower two panels transform according to $A_1$ symmetry. The third coordinate is held fixed at its equilibrium value in all cuts. $r$ and $R$ coordinates are given in bohr, $\theta$ is given in radian.

It is known that molecular states can only dissociate through dissociation channels where the product states reflect the symmetry of the wave function in the interaction region. Thus, symmetry properties only allow the resonance states at 1809.0 and 1832.0 $cm^{-1}$ to dissociate into the second lowest dissociation channel, whereby the $H_2^+$ product is in its first excited $j = 1$ rotational state, where $j$ is the rotational quantum number of the $H_2^+$ diatom. The rotational wave function of the $j = 1$ state, and all the wave functions of $H_2^+$ corresponding rotational states excited by odd quanta, are antisymmetric with respect to the exchange of the two H atoms. The $j = 1$ dissociation channel is estimated, within the rigid rotor approximation, to be around 60 $cm^{-1}$ higher than the first dissociation limit corresponding to the $j = 0$ state of $H_2^+$.[165] Thus, the resonance sates with energies of 1809.0 and 1832.0 $cm^{-1}$ are actually bound states, located below the second lowest dissociation channel which is the first available dissocation channel for states with $B_2$ symmetry. This assertion is supported by the extremely long lifetimes of these states. (The 60 $cm^{-1}$ difference between the opening of the two lowest dissociation channels of $H_2He^+$ can also be observed in Figure 5.5 of Section 5.5.3.)

In the stabilization method histograms of Figure 5.4 two further significant peaks, with large count numbers, appear at energies 1775.5 and 1776.0 $cm^{-1}$. These states have much shorter lifetimes than the two extremely long-lived, actually bound, states at 1809.0 and 1832.0 $cm^{-1}$. From the wave functions of the two states at about 1776 $cm^{-1}$, shown in the two lower panels of Figure 5.3, it is seen that they correspond to $A_1$ symmetry, *i.e.*, their wave functions are symmetric in the $\theta$ coordinate. Thus, the states at 1775.5 and 1776.0 $cm^{-1}$ are indeed resonances, since they are located just above the first dissociation channel, opening at 1775.32 $cm^{-1}$ and corresponding to $A_1$ symmetry, where the $H_2^+$ product is in its $j = 0$ rotational state. The large count number of the states at 1775.5 and 1776.0 $cm^{-1}$ in the stabilization histograms can be explained by the fact that their wave functions are mainly localized in the interaction region of the potential. Nevertheless, the wave functions of these two states in the asymptotic region can be described by large-wavelength continuum waves. The large wavelength reflects the low relative kinetic energy of the products resulting from the fact that these resonances lie just above the first dissociation threshold. This phenomenon will be further discussed in detail in Section 5.5.3.

Table 5.2: Bound vibrational energy levels ($cm^{-1}$) of the $H_2He^+$ complex obtained with GENIUSH in 3D and 2D (the $r$ coordinate is fixed at its equilibrium value), relative to the zero-point vibrational energies 2107.00 and 1113.32 $cm^{-1}$, respectively.

| No. | 3D | 2D | No. | 3D | 2D |
|---|---|---|---|---|---|
| 1 | 2107.00 | 1113.32 | 9 | 1502.70 | 1428.42 |
| 2 | 0.00 | 0.00 | 10 | 1546.34 | 1472.70 |
| 3 | 733.75 | 692.81 | 11 | 1589.90 | 1505.67 |
| 4 | 733.77 | 692.84 | 12 | 1620.93 | 1550.93 |
| 5 | 1150.13 | 1143.90 | 13 | 1682.05 | 1597.39 |
| 6 | 1151.83 | 1146.63 | 14 | 1731.67 | 1647.39 |
| 7 | 1263.65 | 1201.85 | 15 | 1738.34 | 1649.71 |
| 8 | 1264.25 | 1202.44 | 16 | 1771.83 | 1684.44 |

As can also be deduced from the first row of Figure 5.3, the bound state, of $B_2$ symmetry, at 1809.0 $cm^{-1}$ corresponds to the first excited state of the HH-stretching motion, *i.e.*, a node appears in the $r$ coordinate. However, higher excitations of this motion cannot be seen as clearly in the stabilization histograms as in the case of the $NO^+$-stretching motion of the Ar·$NO^+$ complex, detailed in Section 4.4.1. The absence of a clear pattern is probably due to the considerable coupling between the intra- and intermonomer degrees of freedom in the case of the $H_2He^+$ complex, as reveled by 2-dimensional GENIUSH bound-state computations. In these computations the $r$ coordinate is fixed at its equilibrium value. The results of 2D bound vibrational energy computations are listed in Table 5.2. From Table 5.2 it is obvious that in the case of $H_2He^+$ the energy levels obtained from the 2D model differ considerably from their 3D counterparts, this difference reaches 90 $cm^{-1}$ near dissociation. Quasi-degeneracy of the energy levels can also be observed, originating from the double-well PES, on which two equivalent minima reflect the linear structure of $H_2He^+$ with the He atom lying either at one or at the other edge of the $H_2^+$ molecular ion. The coupling between the HH-stretching mode and the intermonomer vibrations, mainly the intermonomer stretching motion, makes possible the efficient "leakage" of the energy from the intramonomer vibration to the $R$ coordinate, through which dissociation proceeds.

### 5.5.2 Relation between the CAP and the stabilization methods

Stabilization method histograms of the $H_2He^+$ system covering the $[0-5000]$ $cm^{-1}$ energy range are presented in Figure 5.4. The upper histogram is based on 13 individual GENIUSH computations, with the maximum value of the dissociation coordinate, $R_{max}$, distributed evenly between 32 and 38 bohr. The histogram shown in the lower part of Figure 5.4 is based on a much larger $R$ interval, where $R_{max} \in [49, 51]$, and is based on 25 computations. Both histograms are generated using a bin size of 0.05 bohr. In contrast to the very clear patterns of the stabilization histogram of $Ar{\cdot}NO^+$, where a 0.001 $cm^{-1}$ bin size was sufficient to obtain peaks of long-lived resonances with maximal count numbers, the stabilization histograms of $H_2He^+$ require the use of a considerably larger bin size. This is due to the stronger coupling between the intra- and intermonomer motions in the case of $H_2He^+$, resulting in the delocalization of the wave functions along $R$, leading to somewhat less converged resonance eigenvalues.

At first glance one can notice that in the upper panel of Figure 5.4, where a shorter $R$ interval is used, only a few significant peaks appear above the dissociation threshold. In contrast, when extending the range along the $R$ coordinate, numerous further peaks emerge. The peaks of the stabilization histogram based on the extended $R$ interval are compared to CAP results in Table 5.3. The correlation between the CAP-active interval, *i.e.*, the range of the $R$ coordinate where the CAP is switched on, of the corresponding GENIUSH-CAP computation and the appearance of a given resonance in the stabilization histogram is also analyzed in Table 5.3.

The relation between the stabilization method and the complex absorbing potential technique is interesting: if one approaches the limit of $\eta = 0$ and narrows the CAP active interval, one approaches the case of a standard bound-state computation. As it is known, resonance eigenvalues can be obtained as converged stable eigenvalues from stabilization computations, and also as cusps in CAP-trajectories on the complex plane. However, as mentioned in Section 2.4.3, in calculations with a CAP (at least) two errors are present: one is due to the damping of the resonance wave function, which also changes the resonance eigenvalues, while the other is due to the use of a

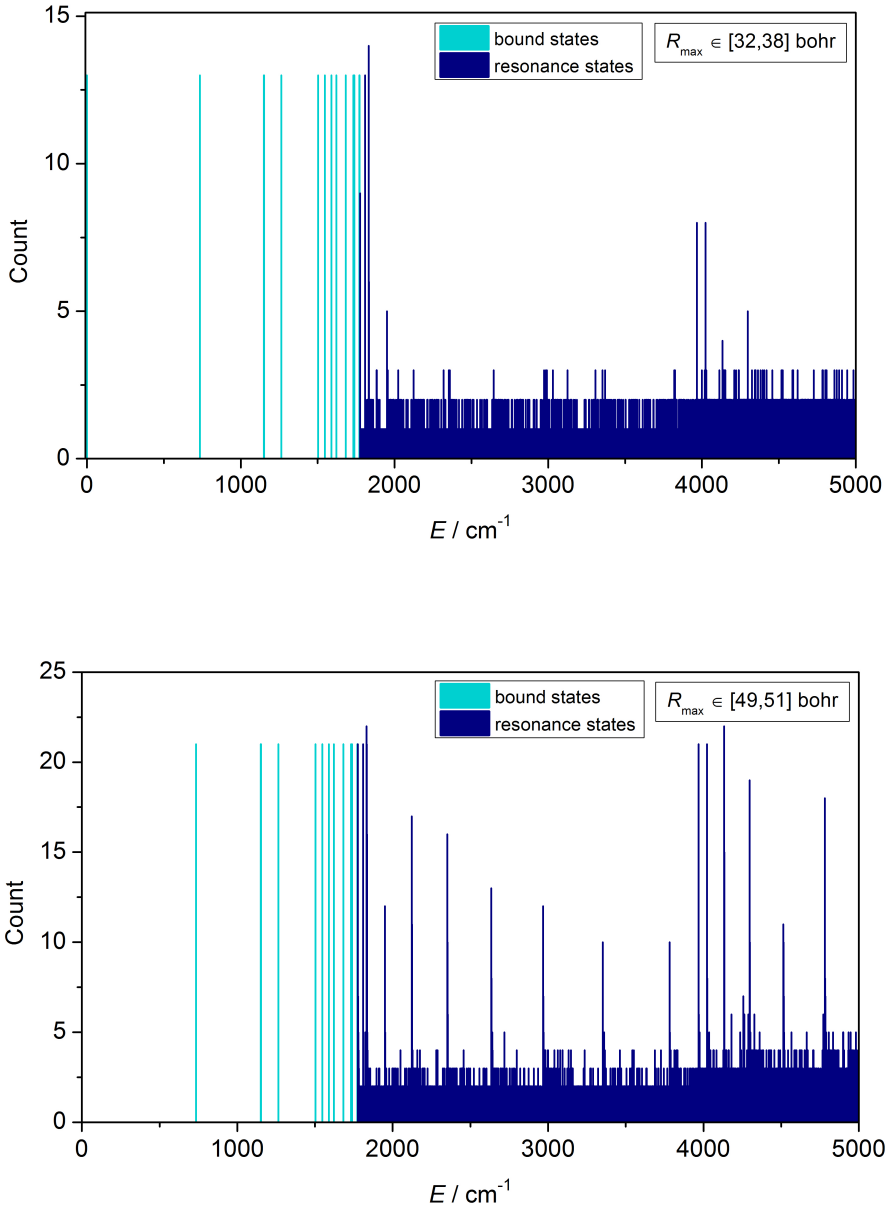


Figure 5.4: Stabilization histogram of the $H_2He^+$ complex using the [32.0,38.0] (13 GENIUSH computations) and the [49.0,51.0] (21 GENIUSH computations) bohr intervals for the $R_{\max}$ values (see the text for details). A bin size of 0.05 cm$^{-1}$ is applied.

finite basis. Thus, if one compares the stabilization method results, whose convergence might also vary, with those of the CAP method, one can obtain the same resonance eigenvalues only within a margin of error, as it is seen in Table 5.3.

Table 5.3 and Figure 5.4 reveal a clear correspondence between the length of the CAP-active interval necessary for finding a given resonance and the peaks appearing

Table 5.3: Stable eigenvalues ($cm^{-1}$) from GENIUSH stabilization computations with extended $R$-range, $R_{max} \in [49, 51]$, and their count numbers (corresponding to a bin size of 0.05 $cm^{-1}$) paired with resonance energies ($cm^{-1}$) and lifetimes (ps), obtained from GENIUSH-CAP computations based on a bound-state computation with $R_{max} = 50$ bohr. The last four columns show the CAP-active $R$ intervals, whereby the given resonance states could be found with the CAP technique. Only resonances that feature peaks in the stabilization histograms with a count number greater than or equal to 10 in the $[D_0, 5000]$ $cm^{-1}$ energy interval are listed.

| Stabilization method | | CAP | | | | | |
|---|---|---|---|---|---|---|---|
| $E_{stab}$ | Count | $E^a_{CAP}$ | lifetime | 10-50 | 20-50 | 30-50 | 40-50 |
| 1775.50 | 21 | 1775.75 | 310 | - | ✓ | ✓ | ✓ |
| 1776.00 | 16 | 1776.72 | 80 | - | - | - | ✓ |
| 1809.00 | 21 | 1809.00[a] | 112360[a] | | | | |
| 1832.00 | 22 | 1831.98 | 26690 | - | ✓ | ✓ | - |
| 1833.80 | 21 | 1834.15 | 250 | - | ✓ | ✓ | ✓ |
| 1834.40 | 16 | 1835.15 | 80 | - | - | ✓ | ✓ |
| 1949.95 | 12 | 1950.41 | 200 | - | - | ✓ | ✓ |
| 2123.05 | 17 | 2123.65 | 140 | - | - | ✓ | ✓ |
| 2123.95 | 11 | 2124.81 | 70 | - | - | - | ✓ |
| 2351.75 | 16 | 2352.48 | 100 | - | - | ✓ | ✓ |
| 2352.80 | 10 | 2353.85 | 50 | - | - | - | ✓ |
| 2634.25 | 13 | 2635.14 | 80 | - | - | - | ✓ |
| 2968.45 | 12 | 2969.55 | 60 | - | - | - | ✓ |
| 3352.00 | 10 | 3353.30 | 50 | - | - | - | ✓ |
| 3352.05 | 10 | 3355.25 | 30 | - | - | - | ✓ |
| 3782.25 | 10 | 3783.73 | 40 | - | - | - | ✓ |
| 3967.90 | 21 | 3968.15 | 330 | - | ✓ | ✓ | ✓ |
| 3968.40 | 16 | 3969.09 | 90 | - | - | - | ✓ |
| 4023.15 | 21 | 4023.48 | 280 | - | ✓ | ✓ | ✓ |
| 4133.25 | 22 | 4133.67 | 210 | - | - | ✓ | ✓ |
| 4133.95 | 15 | 4134.65 | 90 | - | - | ✓ | ✓ |
| 4297.25 | 19 | 4297.84 | 140 | - | - | ✓ | ✓ |
| 4298.15 | 10 | 4299.02 | 70 | - | - | - | ✓ |
| 4513.90 | 11 | 4514.67 | 100 | - | - | - | ✓ |
| 4513.95 | 10 | 4516.03 | 50 | - | - | - | ✓ |
| 4515.00 | 10 | 4516.33 | 830 | - | - | - | ✓ |
| 4781.55 | 18 | 4782.47 | 80 | - | - | - | ✓ |

[a] This resonance state could only be found with $R_{max} = 30$ bohr and with a 10-30 bohr CAP-active interval.

in the stabilization histograms: peaks emerging only in the stabilization histogram based on the extended $R$-range can be found only at smaller CAP-active intervals, *e.g.*, $[30-50]$ or $[40-50]$ bohr, when their wave functions are only damped at the edge of the $R$ interval. In contrast, peaks present in the stabilization histogram based on a smaller $R$ range can be identified even when the CAP is switched on at 20 bohr. GENIUSH-CAP resonance wave functions corresponding to peaks of the stabilization histogram will be presented and analyzed in Section 5.5.3. As can also be seen from Table 5.3, the significant peaks of the stabilization histograms refer to resonances having very long lifetimes; however, not as long as the lifetimes of the (actually bound) states of $B_2$ symmetry at 1809.0 and 1832.0 $cm^{-1}$. It can also be observed that peaks having larger count numbers in the stabilization histograms usually correspond to longer-lived resonance states.

### 5.5.3 Opening of new dissociation channels

By inspecting the complex eigenvalue trajectories of the complex scaled Hamiltonian, computed with the D$^2$FOPI-CCS program and presented graphically in Figure 5.5, one can immediately notice a clear pattern. In the vicinity of specific energy values on the real axis, an increasing density of points can be observed. Also, rotated bands of continuum states appear at these specific energies. These continuum states, corresponding to new dissociation channels, result in branch cuts of the scattering matrix and are rotated by $2\vartheta$ due to complex scaling, where $\vartheta$ is the scaling parameter. As discussed in Section 2.4.2, complex resonance eigenvalues corresponding to the given dissociation channel are located between the rotated continuum and the real axis of the complex plane. The increased density of complex eigenvalues near the real axis at the opening of a new channel refers to many long-lived resonances appearing just above the given dissociation threshold.

If one takes a closer look at the stabilization method histogram generated with the extended $R$ range, presented in the lower panel of Figure 5.4, it can be noticed that the peaks of this histogram coincide with the energy thresholds of the new dissociation channels, clearly visible in Figure 5.5. (Since the current implementation of GENIUSH, employed during this study, does not exploit symmetry, resonance states corresponding

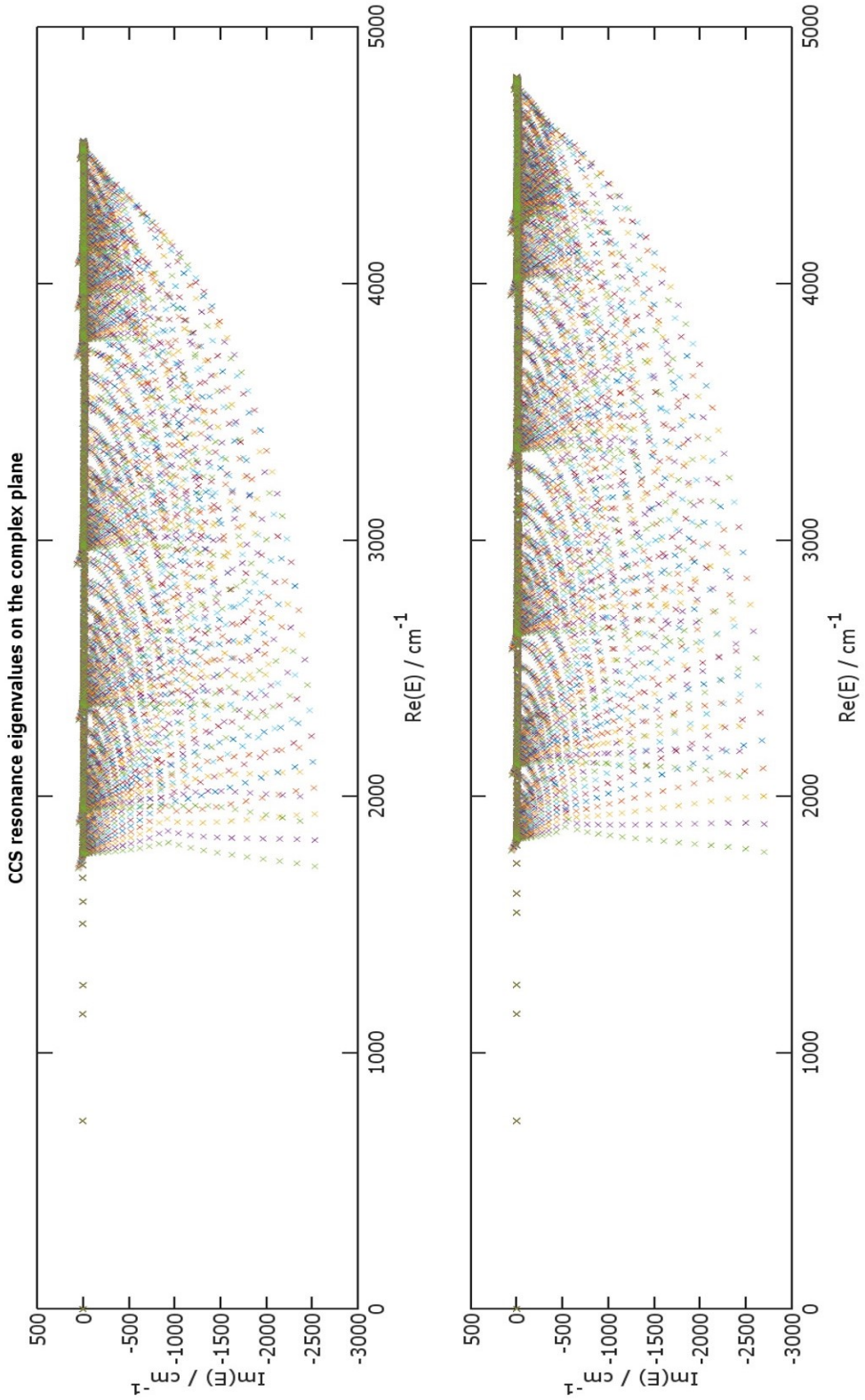


Figure 5.5: Resonance eigenvalues of $A_1$(left panel) and $B_2$ (right panel) symmetry, obtained from D$^2$FOPI-CCS computations performed at 40 different scaling parameter values, in the energy range of $[0 - 4800]$ cm$^{-1}$.

Table 5.4: Rotational energies of $H_2^+$, estimated within the rigid rotor approximation with first-order correction due to centrifugal distortion, relative to the first dissociation limit at 1775 $cm^{-1}$. $B = 30.2\ cm^{-1}$ denotes the rotational constant[165] of $H_2^+$, $D = 0.018$ $cm^{-1}$ is the quartic centrifugal distortion constant,[165] and $j$ is the rotational quantum number of $H_2^+$. Symmetries are denoted by the $A_1$ and $B_2$ irreducible representations of the $C_{2v}$(M) group, which, within the rigid rotor approximation, correlate with the $\Sigma^+$ and $\Sigma^-$ irreducible representations of the $D_\infty$ rotational group characterizing $H_2^+$, respectively.

| Symmetry | $E_{\text{diss}}$ | $j$ | $Bj(j+1) - Dj^2(j+1)^2$ |
|---|---|---|---|
| $A_1$ | 0 | 0 | 0 |
| $B_2$ | 58 | 1 | 60 |
| $A_1$ | 175 | 2 | 181 |
| $B_2$ | 348 | 3 | 360 |
| $A_1$ | 577 | 4 | 597 |
| $B_2$ | 860 | 5 | 890 |

to both $A_1$ or $B_2$ symmetry appear in the stabilization histograms.) In Table 5.3, resonance states with long lifetimes appearing just above the dissociation thresholds highlight the opening of the new channels.

If one estimates, within the rigid rotor approximation, augmented with a centrifugal distortion correction,[165] the rotational energies of the $H_2^+$ molecule at different values of the diatomic rotational quantum number $j$, as listed in Table 5.4, it can be observed that these energies coincide with the energies corresponding to the opening of the new dissociation channels, given relative to the first dissociation limit of $H_2He^+$.

The resonance wave functions in the asymptotic region reflect the symmetries and rotational excitations of the corresponding $H_2^+$ product states: even $j$ quantum numbers correspond to $A_1$ symmetry, while channels characterized by odd $j$ values correspond to $B_2$ symmetry.

$R - \theta$ cuts of GENIUSH-CAP resonance wave function plots corresponding to the first three resonances of each new dissociation channel are shown in Figure 5.6. Each row of Figure 5.6 corresponds to one dissociation channel and contains wave functions with the same nodal structure in the $\theta$ coordinate. That is, the resonance wave functions of the 1$^{\text{st}}$ row feature no nodes along the $\theta$ coordinate. Starting from the second row, wave functions of each row feature $1, 2, 3$ and 4 nodes, *i.e.*, single, double, triple,

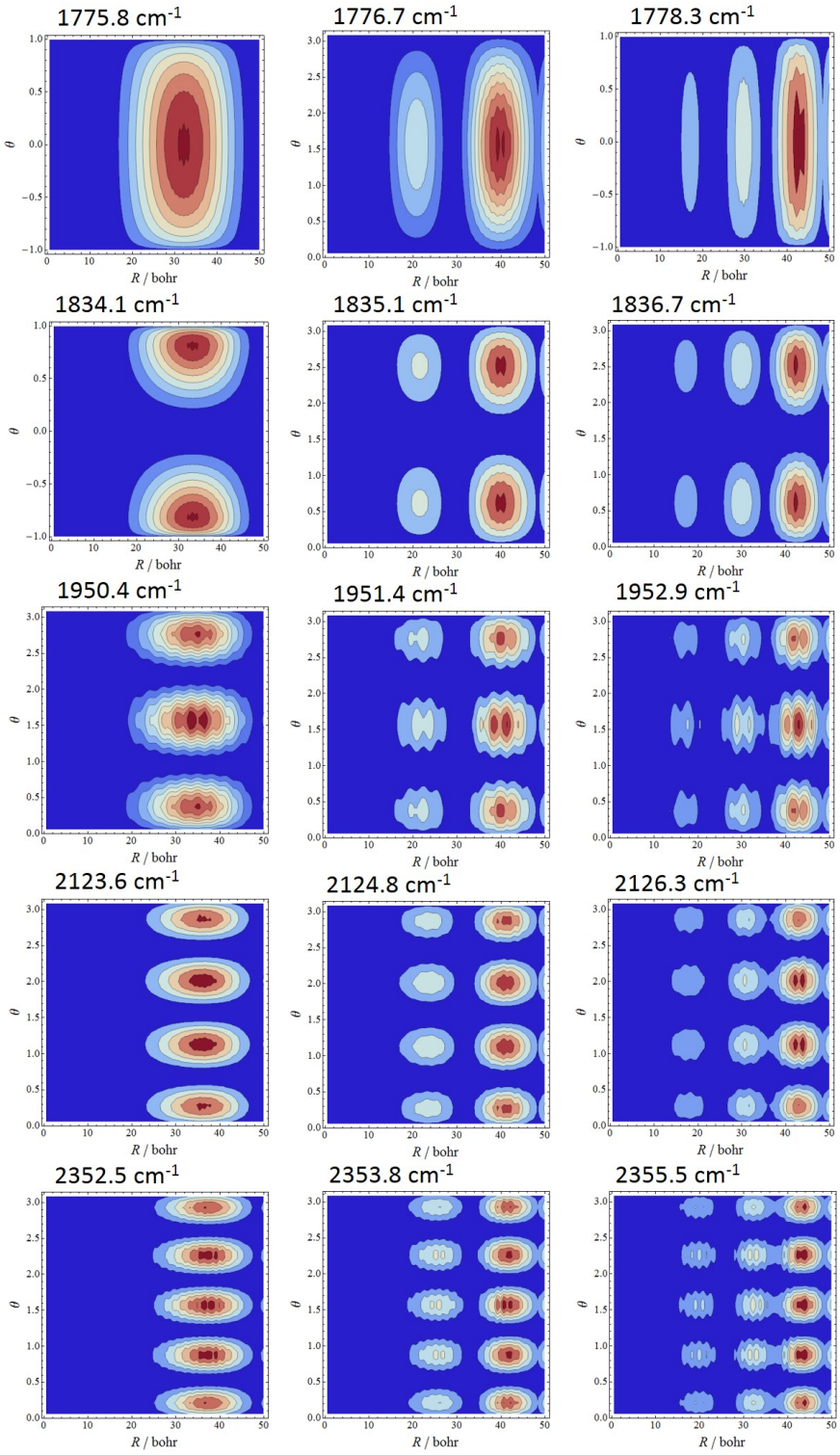


Figure 5.6: $R-\theta$ wave function cuts of three resonances states (their absolute values are plotted) of $H_2He^+$ emerging just above the first five new dissociation channels corresponding to rotational excitations of $H_2^+$, *i.e.*, $j = 0, 1, 2, 3$, and 4. These resonances are obtained from GENIUSH-CAP computations carried out utilizing the $R_{\max} = 50$ bohr GENIUSH stabilization computation. The CAP is switched on between 40-50 bohr along the $R$ dissociation coordinate. The $R$ coordinate is given in bohr, $\theta$ is given in radian.

and quadruple excitations of the intermonomer bending motion, respectively. Due to the $J = 0$ constraint, this bending motion can be associated with the rotational motion of $H_2^+$, characterized by the $j$ quantum number. Thus, each dissociation channel (each row of Figure 5.6) corresponds to the rotational excitations of the $H_2^+$ product, *i.e.*, $j = 0, 1, 2, 3$, and 4 for the first five channels. The relative energies of the dissociation channel openings are in good agreement with the rotational energies of $H_2^+$ listed in Table 5.4. Note that the opening of further dissociation channels characterized by larger $j$ quantum numbers can also be observed at higher energies.

As Figure 5.5 shows, the first dissociation channel corresponding to $B_2$ symmetry (right panel of Figure 5.5) opens about 60 $cm^{-1}$ above the first dissociation threshold, of $A_1$ symmetry (left panel), giving rise for $B_2$ symmetry bound states above the lowest dissociation limit of the $H_2He^+$ molecule, as discussed in Section 5.5.1.

The third resonance states of the rows of Figure 5.6, *i.e.*, the third resonances above the newly opened dissociation thresholds, are not seen in Table 5.3, since their count number in the stabilization histogram based on the extended $R$ range do not reach 10. This is because their wave functions are localized mainly in the asymptotic region. In contrast, the first resonances appearing just above the dissociation energies (first plot of each row in Figure 5.6) have significant peaks in the stabilization histogram. The second lowest resonance states above the channel openings (middle plots of the rows of Figure 5.6) are usually also indicated by stabilization histogram peaks, although with lower count numbers, due to the fact that their wave functions extend more into the asymptotic region.

Going from left to right in a given row of Figure 5.6, an increasing number of nodes in the $R$ coordinate can also be observed. This observation refers to the increasing relative kinetic energy of the products above the given dissociation channel, which results in a decrease in the wavelength of the continuum wave describing the wave function at the asymptotic region of the PES. Later in this thesis a similar phenomenon will also be discussed in the case of the $H_2$·CO complex.

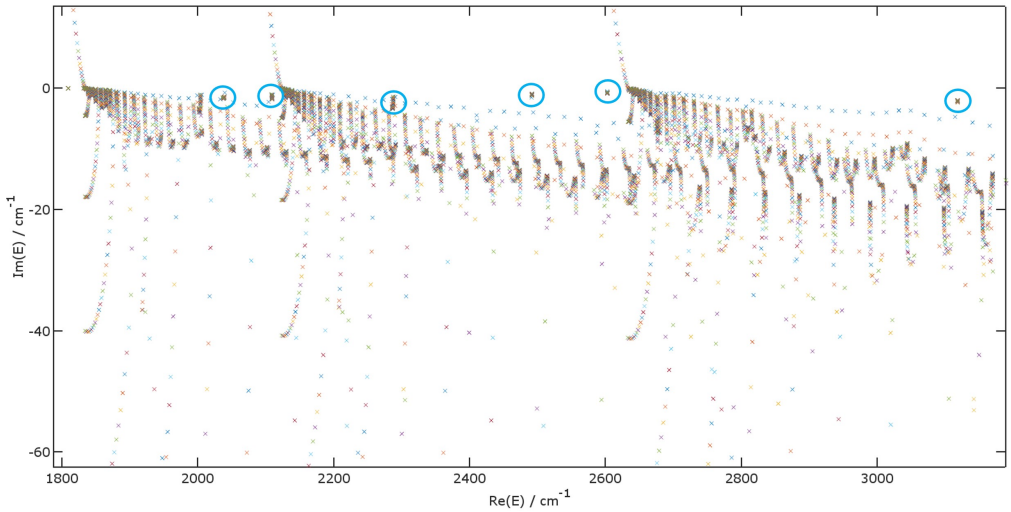


Figure 5.7: Complex coordinate scaling resonance eigenvalues of $B_2$ symmetry obtained at 40 different values of the scaling parameter, zooming in the energy range of $[1800, 3200]$ cm$^{-1}$, while the imaginary part of the resonance eigenvalues is restricted between $[-60, 0]$ cm$^{-1}$. Blue circles highlight long-lived, isolated resonances, corresponding to strong coupling of the intramonomer-stretching and intermonomer-bending motions.

### 5.5.4 Resonances due to strong internal-motion coupling

Closer inspection of D$^2$FOPI-CCS complex eigenvalues of $H_2He^+$ on the complex plane, presented in Figure 5.5, reveals several isolated eigenvalue trajectories, highlighted by blue circles in Figure 5.7. Figure 5.7 only shows resonance eigenvalues corresponding to $B_2$ symmetry, however, similar isolated states of $A_1$ symmetry were also found. The complex coordinate scaling trajectories corresponding to these isolated resonance states cover a very narrow energy range, and they always occur at imaginary parts between $-1$ and $-4$ cm$^{-1}$. These imaginary parts indicate somewhat shorter lifetimes for these resonances than the lifetimes of the resonance states corresponding to the opening of new dissociation channels.

I have successfully identified these isolated resonances with GENIUSH-CAP, as well (in the stabilization histograms they could not be found, probably due to their relatively short lifetimes), where they are also featured by localized eigenvalue trajectories on the complex plane. Plots of the wave functions of five selected isolated resonances are shown in Figure 5.8. In Figure 5.8 at energies of 2038.6, 2109.0, and 2286.8 cm$^{-1}$ resonance wave functions transforming according to $B_2$ symmetry are

seen. The wave functions, also shown in Figure 5.8, of the resonance states at energies of 2321.6 and 2929.7 $cm^{-1}$ correspond to $A_1$ symmetry. Symmetry properties of these isolated resonances are known from both analyzing the resonance wave function plots and from $D^2$FOPI-CCS computations.

What is common in all of the resonance states of Figure 5.8 corresponding to $B_2$ symmetry, is the excitation pattern seen in all $r-\theta$ cuts of their wave functions. This pattern of five nodes in the $\theta$ coordinate corresponds to a quintuple excitation of the intermonomer bending motion. It is known that in the case of $J=0$, where $|j|=|l|$, this motion can be associated both with the rotational motion of the He atom around the $H_2^+$ unit, characterized by the $l$ quantum number, and with the rotational motion of the $H_2^+$ diatom.

From the wave function plots of Figure 5.8 it is clear that the HH stretching and the intermonomer bending motions become very strongly coupled, *i.e.*, for different values of $\theta$ the distribution of the wave function along the $r$ coordinate changes considerably.

In the case of resonance states of Figure 5.8 transforming according to $A_1$ symmetry, in the $r-\theta$ cuts of their wave functions four nodes can be observed. This four nodes refer to quadruple excitation of the intermonomer bending motion of $H_2He^+$. The isolated resonance states of $A_1$ symmetry, similarly to the isolated $B_2$ resonance states, also feature a motion corresponding to the strong coupling of the intermonomer-bending and the intramonomer-stretching motions in $H_2He^+$.

From the relatively long lifetimes of these isolated resonance states it seems that energy leakage to the dissociation coordinate from the coupled intermonomer-bending and intramonomer-stretching motions is small. These kind of resonance states are perfect examples of Feshbach resonances. In Figure 5.8 one can see that the quintuple ($B_2$ symmetry) and quadruple ($A_1$ symmetry) excitations of the bending motion can only be observed in the interaction region of the PES for all the wave functions. On the other hand, the nodal structure along the $\theta$ coordinate in the asymptotic parts of the wave functions of these Feshbach resonances reveals that these states dissociate into the nearest lower-lying dissociation channels.

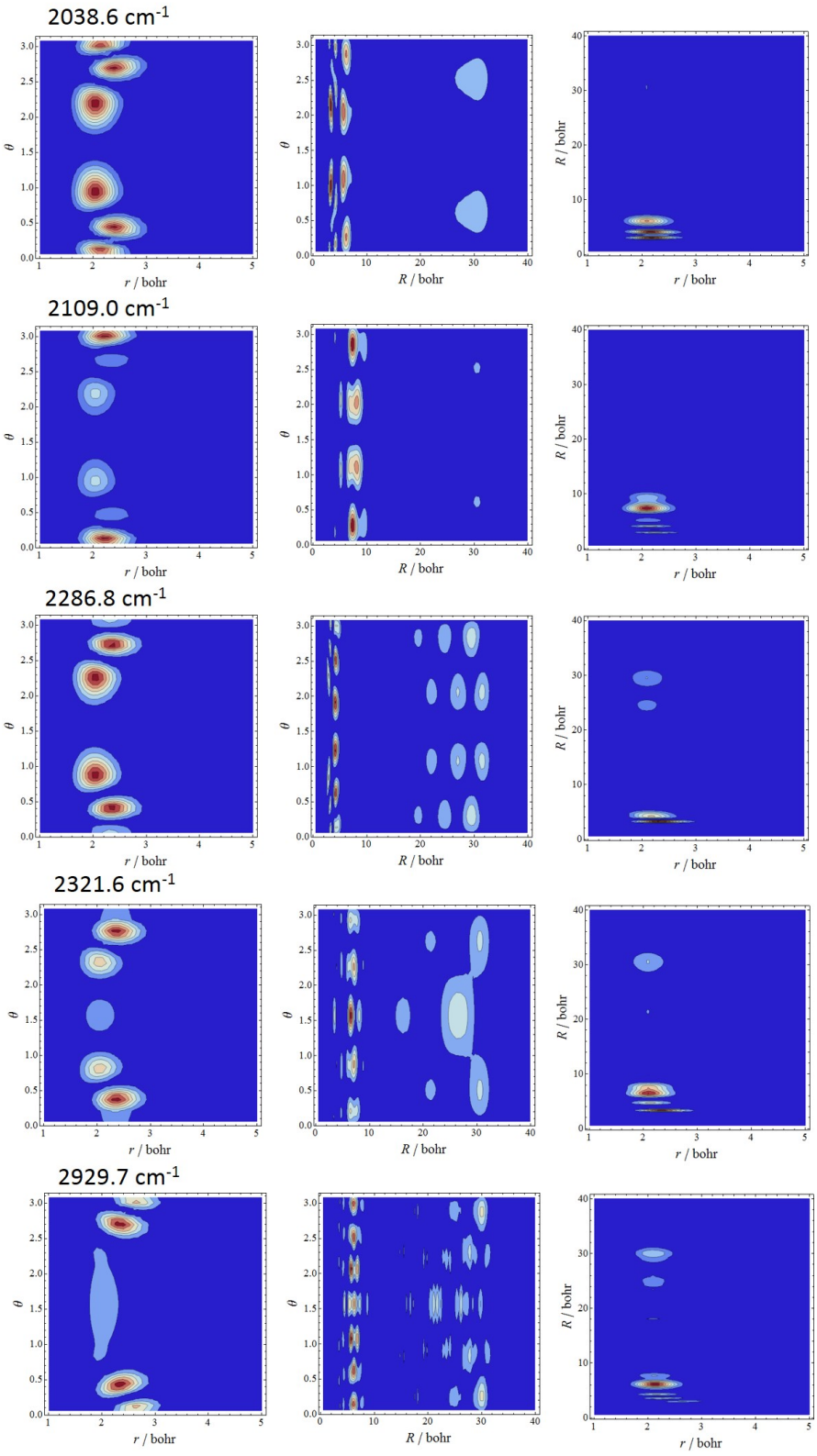


Figure 5.8: 2D GENIUSH-CAP cuts of the absolute values of selected resonance wave functions of $H_2He^+$, corresponding to isolated $D^2$FOPI-CCS and GENIUSH-CAP eigenvalue trajectories. These resonance states are found at energies of $2038.6, 2109.0, 2286.8, 2321.6$ and $2929.7$ cm$^{-1}$.

## 5.6 Concluding remarks

Besides testing of the new code, I have identified several resonance states of the $H_2He^+$ complex, important from an astrophysical point of view. The GENIUSH-CAP code has been validated by comparing the resonance energies and lifetimes of $H_2He^+$ with those obtained from complex coordinate scaling computations, employing the D$^2$FOPI-CCS code, developed in our group.[5] The comparison shows excellent agreement: resonance energies agree within a few 0.1 cm$^{-1}$, while the lifetimes of the resonance states are computed within the same order of magnitude. Inspection of resonance wave functions has been shown to provide useful qualitative information about the nature of the resonance states.

Furthermore, GENIUSH-CAP, D$^2$FOPI-CCS, and stabilization method computations have revealed interesting features of the resonance states of $H_2He^+$. These features have been resolved by analyzing resonance wave functions provided by GENIUSH-CAP. Based on a wave-function analysis and also on rigid-rotor energies, opening of new dissociation channels could be assigned to the rotational excitations of $H_2^+$. Because the second lowest dissociation channel, corresponding to $B_2$ symmetry, opens approximately 60 cm$^{-1}$ above the first one, of $A_1$ symmetry, $B_2$ bound states could be found as extremely long-lived resonances above the first dissociation threshold of the complex.

In addition, several isolated Feshbach resonance states have been identified, which appear due to strong intramonomer-stretching and intermonomer-bending coupling. Based on this observation, and also on 2D GENIUSH computations, it seems that in $H_2He^+$, unlike in Ar·NO$^+$, the internal degrees of freedom are considerably coupled.

# Chapter 6

# Resonance states of the $H_2$·CO complex

## 6.1 Introduction to the $H_2$·CO complex

The $H_2$·CO complex serves as a benchmark system for those who study weakly-bound molecular complexes. The $H_2$·CO complex also has astrophysical importance, as $H_2$ and CO are the first and second most abundant molecules in space, respectively. While $H_2$ cannot be observed at low temperatures, CO is very easy to detect in interstellar space. Therefore, CO is used for tracing $H_2$ in low-temperature regions, through its rotational excitation or deexcitation due to collisions with $H_2$.[11] In cross-beam experiments, Chefdeville and co-workers[10] investigated the inelastic collisions of $H_2$ and CO in detail, and for the first time they have resolved the resonance structure of these processes.

Among the three nuclei forming the $H_2^{12}C^{16}O$ complex, only protons have non-zero nuclear spins. In what follows $H_2$·CO always means the $H_2^{12}C^{16}O$ complex. Thus, depending on the coupling of the nuclear spins of the H nuclei, the $H_2$·CO complex can be either in an so-called *ortho* or in a *para* state. *Ortho*-$H_2$·CO has a symmetric nuclear spin wave function, and *para*-$H_2$·CO has an antisymmetric one. The total molecular wave function must be antisymmetric since the H nucleus is a fermion; therefore, the rovibrational wave function of *ortho*-$H_2$·CO must be antisymmetric with respect to the

permutation of the protons. Naturally, the reverse holds for *para*-$H_2$·CO. This implies that only odd rotational quantum numbers are allowed for $H_2$ in *ortho*-$H_2$·CO, while in *para*-$H_2$·CO $H_2$ can exist only in states described by an even rotational quantum number $j_1$.

The infrared (IR) spectrum of $H_2$·CO has been measured in 1998, and transitions corresponding to *para*-$H_2$·CO were successfully identified.[166] The IR spectrum of *ortho*-$H_2$·CO has not been possible to fully assign until a very accurate PES was developed by Jankowski and Szalewicz,[6;167] using state-of-the-art electronic structure theory and a procedure averaging over the monomer vibrations. This PES meant a significant correction to previous PESs,[168;169] which could reproduce experimental transitions of *para*-$H_2$·CO, but failed in the case of *ortho*-$H_2$·CO. A full-dimensional PES was developed later for $H_2$·CO.[170]

Both the *para* and the *ortho* forms of $H_2$·CO have quite low dissociation thresholds and thus they possess only a few bound states. Thus, it is worth investigating the resonance states of this complex as they may have an important role in the chemistry of $H_2$·CO. Using the different PESs developed for $H_2$·CO,[6;167–170] several attempts have been made to understand the resonance structure of this complex. These studies[10;12;171] showed that resonance states of $H_2$·CO play an important role in inelastic collisions of $H_2$ and CO, as well as in resolving the IR spectrum of the complex.

Employing GENIUSH-CAP, I have determined numerous resonance states of the $H_2$·CO complex and analyzed them in detail. This is the first case, to the best of my knowledge, when a four-atomic system is subjected to a non-Hermitian variational resonance computation.

## 6.2 Computational details

### 6.2.1 The potential energy surface

The nuclear motion computations of the $H_2$·CO complex employed a 4D PES. The PES, taken from Ref. 167, is averaged over the intramonomer vibrations, corresponding

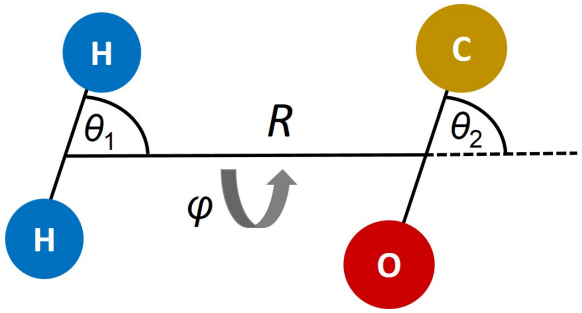


Figure 6.1: A coordinate system describing the intermolecular degrees of freedom of $H_2$·CO, used in the reduced-dimensional GENIUSH computations of this study.

to the $v = 0$ states of CO and $H_2$. The first dissociation limit of $H_2$·CO corresponds to the dissociation of the *para*-$H_2$·CO complex, with threshold energies of $D_{e,para} = 94.096$ $cm^{-1}$ and $D_{0,para} = 19.440$ $cm^{-1}$.[6;167] Naturally, in this case the $H_2$ product is in its ground rotational state ($j_1 = 0$). The dissociation limit corresponding to *ortho*-$H_2$·CO, $D_{0,ortho}$, where the $H_2$ product is in its first-excited rotational state ($j_1 = 1$) is $2B$ above the *para* dissociation energy (within the rigid rotor approximation), where $B$ refers to the rotational constant of the $H_2$ molecule. In the case of GENIUSH-CAP computations, one obtains both the *para*- and the *ortho*-$H_2$·CO states in the same computation. The 4D model implies that the $B$ rotational constant corresponds to the frozen bond length, 1.449 bohr, proposed in Ref. 167 for the $H_2$ monomer; thus, $B_{4D} = 56.919$ $cm^{-1}$. This is 2.403 $cm^{-1}$ lower than the experimental value[172] of $B_{expt} = 59.322$ $cm^{-1}$. Therefore, the *ortho* dissociation energy obtained from the reduced-dimensional model, 113.838 $cm^{-1}$ relative to the *para* dissociation limit, is 4.806 $cm^{-1}$ lower than the experimental value of the *ortho* dissociation energy, 118.644 $cm^{-1}$. Thus, we expect to obtain *ortho*-$H_2$·CO energy levels approximately 5 $cm^{-1}$ lower (the convergence of certain states may vary) than the absolute energies obtained from experiments.

### 6.2.2 Computation of resonance states

During the nuclear motion computations generalized Jacobi coordinates were employed to represent the intermolecular motions of $H_2$·CO. These coordinates are sketched in Figure 6.1. The equilibrium structure of the complex is characterized by $R_{eq} = 7.9145$ bohr, $\theta_{1,eq} = 0°$, $\theta_{2,eq} = 180°$, and $\phi_{eq} = 0°$. The intramonomer

vibrations are kept frozen during the GENIUSH bound-state computations. In these computations the following intervals and basis sets are used for the active coordinates: $R \in [5.0, 40.0]$ bohr with 200 scaled Laguerre-DVR points, $\theta_1$ and $\theta_2 \in (0.0, 180.0)^\circ$ with 30 and 30 unscaled Legendre-DVR points, respectively, and $\phi \in [0.0, 360.0]^\circ$ with 51 scaled Fourier-DVR points. The intramonomer distances were fixed at 1.449 and 2.140 bohr for $H_2$ and CO, respectively.[167] The following masses were used during these computations: $m_H = 1.007825035$ u, $m_C = 12.00000000$ u, and $m_O = 15.99491463$ u.

During the GENIUSH-CAP computations the $R$ interval where the CAP was switched on was changed between 20 and 40 bohr, with the starting value of $R$ (20 bohr) being increased by a step size of 5 bohr. 220 vibrational GENIUSH eigenvectors were used as a basis for the CAP computations. Convergence of resonance states, varying between $0.1 - 1$ cm$^{-1}$ for a given resonance, was tested by changing the number of basis functions on each coordinate by 10 %. All the resonance energies in this Chapter are given relative to the *para*-$H_2$·CO zero-point energy (ZPE), which is 74.66 cm$^{-1}$ (the value of the PES is 0.00 cm$^{-1}$ at the global minimum). All three bound vibrational states of *para*-$H_2$·CO obtained with GENIUSH agree well, within 0.03 cm$^{-1}$, with those reported in Ref. 6.

## 6.3 The *ortho*-$H_2$·CO bound states

I have determined several vibrational resonance states of the $H_2$·CO complex employing the GENIUSH-CAP program. Since the first dissociation limit of $H_2$·CO, as mentioned above, is $D_{0,para} = 19.440$ cm$^{-1}$, in GENIUSH-CAP computations one obtains all the states that have higher energy then $D_{0,para}$ as resonance states. The dissociation limit corresponding to the *ortho*-$H_2$·CO complex, 113.838 cm$^{-1}$ relative to the *para* dissociation limit and 133.278 cm$^{-1}$ relative to the *para*-$H_2$·CO ZPE in the 4D model, lies much higher than $D_{0,para}$. The ZPE of the *ortho*-$H_2$·CO complex is 97.97 cm$^{-1}$ relative to the *para* dissociation limit.[6] Thus, all the bound states corresponding to the *ortho*-$H_2$·CO complex are expected to be obtained as resonance states with GENIUSH-CAP. In line with this, I found seven extremely long-lived resonances below the dissociation energy of *ortho*-$H_2$·CO in my GENIUSH-CAP computations.

Energies and lifetimes of these *ortho* states are listed in Table 6.1.

Table 6.1: Resonance energies ($cm^{-1}$) relative to the *para*-$H_2$·CO zero-point (*p*-ZPE) energy (1st column), lifetimes (ns), and resonance energies relative to the *ortho*-$H_2$·CO zero-point energy (*o*-ZPE) (3rd column) of extremely long-lived resonance states of the *ortho*-$H_2$·CO complex, obtained from GENIUSH-CAP computations. Bound energy levels ($cm^{-1}$) relative to *p*-ZPE (4th column), and relative to *o*-ZPE (5th column) taken from Ref. 6. The last column contains the differences between the GENIUSH-CAP resonance energies and the bound-state energies of Ref. 6, both relative to *p*-ZPE. Bound and resonance energies, relative to *o*-ZPE are in good agreement and are boldfaced.

| GENIUSH-CAP | | | Ref. 6 | | difference |
|---|---|---|---|---|---|
| $E_{res}$ rel. to *p*-ZPE | lifetime | $E_{res}$ rel. to *o*-ZPE* | $E_{bound}$ rel. to *p*-ZPE | $E_{bound}$ rel. to *o*-ZPE | $E_{bound} - E_{res}$ rel. to *p*-ZPE |
| 112.9 | 43.9 | **0.4** | 117.8 | **0.4** | 4.8 |
| 113.6 | 9.2 | **1.1** | 118.6 | **1.2** | 4.9 |
| 116.9 | 23.3 | **4.3** | 121.7 | **4.3** | 4.9 |
| 118.1 | 6.5 | **5.6** | 123.1 | **5.7** | 5.0 |
| 125.6 | 21.8 | **13.0** | 130.5 | **13.1** | 4.9 |
| 131.3 | 24.9 | **18.7** | 136.3 | **18.9** | 5.0 |
| 131.3 | 14.4 | **18.8** | 136.4 | **19.0** | 5.1 |

*Assuming that the lowest $J = 0$ states are the same.

In the joint experimental and theoretical work of Ref. 6 also seven vibrational bound-state energies have been reported for *ortho*-$H_2$·CO. However, the energy levels reported in Ref. 6 were obtained from separate computations for *para*- and *ortho*-$H_2$·CO, and the *ortho*-$H_2$·CO bound-state energies were shifted later with the experimental value of $D_{0,ortho}$, 118.644 $cm^{-1}$ with respect to the *para* dissociation. The GENIUSH-CAP *ortho*-$H_2$·CO energy levels therefore deviate by approximately 5 $cm^{-1}$ from the results of Ref. 6. This is the difference between the experimental and the reduced-dimensional theoretical $D_{0,ortho}$ values.

Apart from the 5 $cm^{-1}$ absolute difference, the transitions of the measured infrared spectrum agree very well, within $0.1 - 0.2$ $cm^{-1}$, with their GENIUSH-CAP counterparts. This good agreement is highlighted by the boldfaced numbers in Table 6.1, corresponding to GENIUSH-CAP relative energies (3rd column of Table 6.1) and relative energies computed (and also determined experimentally) in Ref. 6 (5th column of Table 6.1). These relative energies are measured from the ZPE of *ortho*-$H_2$·CO. In

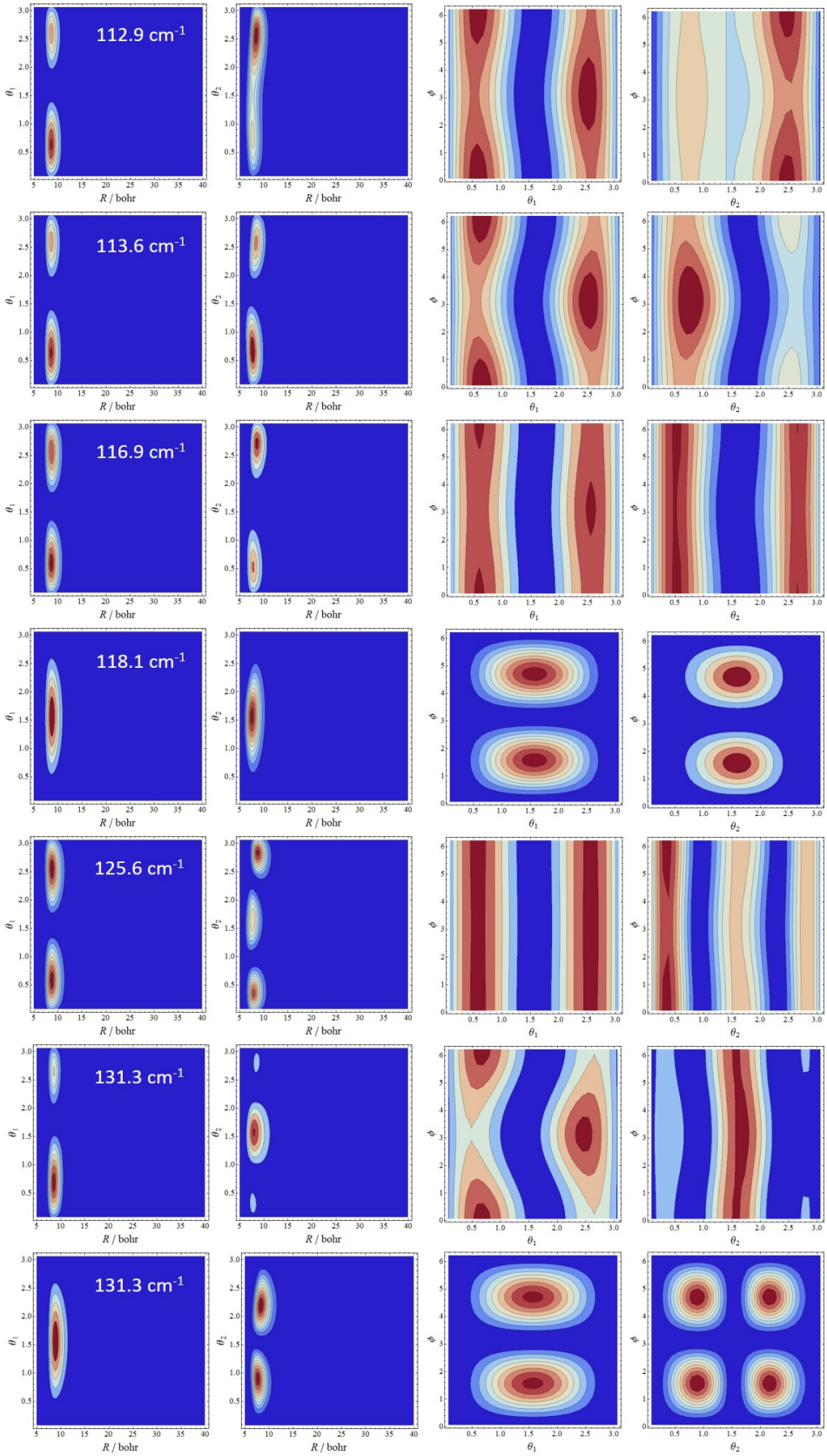


Figure 6.2: Selected GENIUSH-CAP resonance wave-function cuts of extremely long-lived resonance states corresponding to the bound states of the *ortho*-$H_2$·CO complex.

$J = 0$ GENIUSH-CAP computations, where $J$ is the total rotational quantum number of the system, the rovibrational ground state of *ortho*-$H_2$·CO does not appear, since it is found in the $J = 1$ manifold. This indicates that $H_2$·CO belongs to the group of molecules featuring negative rotational energies.[173;174] However, from Ref. 6 it is known that the *ortho*-$H_2$·CO ZPE is 0.39 $cm^{-1}$ lower than the lowest $J = 0$ state. Thus, to compare energy differences between the seven extremely long-lived resonance states of *ortho*-$H_2$·CO obtained from GENIUSH-CAP and between the bound vibrational *ortho*-$H_2$·CO states computed in Ref. 6, it was assumed that the lowest $J = 0$ states of the *ortho*-$H_2$·CO complex are the same in the two computations.

GENIUSH-CAP resonance wave function plots of the seven extremely long-lived resonances are presented in Figure 6.2. All of the GENIUSH-CAP eigenvalue trajectories of these states cover a very narrow energy range, and the corresponding eigenvalues could be converged to within 0.1 $cm^{-1}$. Thus, not surprisingly, the wave-function plots of these high-lying resonance states reveal that these states are perfectly localized in the potential well along the $R$ coordinate. The wave functions show a very clear structure implying intermonomer bending excitations, which structure also support the fact that they correspond to the bound states of the *ortho*-$H_2$·CO complex. Assignments proposed for the *ortho*-$H_2$·CO bound states in Ref. 6 are supported by the corresponding GENIUSH-CAP resonance wave-function plots. Note that the appearance of the *ortho*-$H_2$·CO bound states as resonances with finite lifetimes is due only to the utilization of the CAP.

## 6.4 Vibrational resonances of *para*-$H_2$·CO

I have also identified several resonances appearing in the energy region $[D_{0,para}, 50]$ $cm^{-1}$. Energies and lifetimes of these resonance states, having an imaginary part greater than $-1.0$ $cm^{-1}$, are listed in Table 6.2. In Figure 6.3 the GENIUSH-CAP eigenvalue trajectories corresponding to two selected resonance states of *para*-$H_2$·CO, those with energies of 19.5 $cm^{-1}$ and 24.2 $cm^{-1}$, are shown. In Figure 6.4 the resonance wave functions of these two resonances are presented. The resonance state at 19.5 $cm^{-1}$ (left panels of Figure 6.4) is just above the $D_{0,para}$ limit, with a lifetime as large as

Table 6.2: Resonance energies and lifetimes of the *para*-$H_2$·CO complex computed with GENIUSH-CAP. 1st and 2nd columns show all resonance positions and lifetimes, respectively, in the range of $[D_{0,para}, 50]$ $cm^{-1}$, having an imaginary part greater than $-1.0$ $cm^{-1}$. The 3rd and 4th columns show energies of the resonance states relative to the first resonance state, and to the new dissociation channels characterized by the rotational energies of CO, respectively. The 5th column shows assignments (see the text for details) of the resonances listed in columns 1 and 2. Resonance positions are given in $cm^{-1}$, while lifetimes are given in ps. The meaning of boldfaced numbers is discussed in the text.

| $\mathrm{Re}(E_{\mathrm{res}})$ | lifetime | $E_{rel,j_2=0}$ | $E_{rel,j_2}$ | $j_2$ $n$ |
|---|---|---|---|---|
| 19.5 | 1810 | 0.0 | 0.0 | 0 0 |
| 20.3 | 175 | 0.8 | **0.8** | 0 1 |
| 21.8 | 67 | 2.4 | **2.4** | 0 2 |
| 23.3 | 515 | **3.8** | 0.0 | 1 0 |
| 24.0 | 46 | 4.5 | 0.7 | 0 3 |
| 24.2 | 96 | 4.7 | **0.9** | 1 1 |
| 25.7 | 63 | 6.2 | **2.4** | 1 2 |
| 26.8 | 25 | 7.3 | 3.5 | |
| 27.8 | 42 | 8.3 | **4.5** | 1 3 |
| 29.6 | 48 | 10.1 | 6.3 | |
| 31.5 | 124 | **12.0** | 0.0 | 2 0 |
| 31.8 | 55 | 12.3 | 0.3 | |
| 32.3 | 77 | 12.8 | **0.8** | 2 1 |
| 32.3 | 74 | 12.8 | 0.8 | |
| 33.7 | 43 | 14.2 | **2.2** | 2 2 |
| 36.1 | 30 | 16.6 | **4.6** | 2 3 |
| 43.2 | 85 | 23.7 | 11.7 | |
| 43.4 | 239 | **23.9** | 0.0 | 3 0 |
| 44.2 | 62 | 24.7 | 0.8 | |
| 44.4 | 96 | 24.9 | **1.0** | 3 1 |
| 45.8 | 52 | 26.3 | **2.4** | 3 2 |
| 47.8 | 29 | 28.3 | **4.4** | 3 3 |

1810 ps, and its wave function is localized mainly at 8-9 bohr and further at 15-25 bohr. Inspection of the right panels of Figure 6.4 reveals that the shorter-lived (96 ps) resonance state at 24.2 $cm^{-1}$ features a more extended wave function along $R$, mainly localized at the asymptotic region of the PES.

In Table 6.2 assignments are proposed for some of the resonance states of *para*-$H_2$·CO. In Figure 6.5, the $R - \theta_2$ cuts of the resonance wave functions of selected *para*-$H_2$·CO states are plotted. In different rows of Figure 6.5 different number of nodes along the $\theta_2$ coordinate appear in the resonance wave functions, which can be

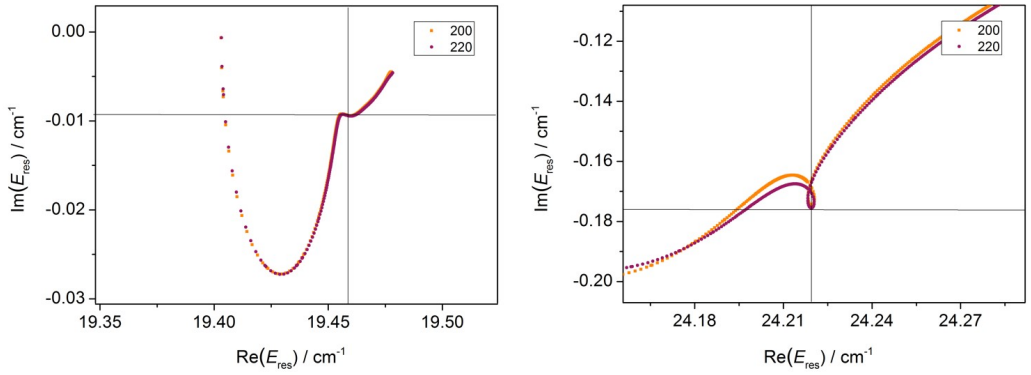


Figure 6.3: GENIUSH-CAP eigenvalue trajectories of two selected resonance states of the *para*-$H_2$·CO complex, with resonance energies 19.5 and 24.2 cm$^{-1}$, corresponding to the wave function plots of Figure 6.4. Orange and purple dots refer to 200 and 220 basis functions along the $R$ dissociation coordinate in the GENIUSH bound-state computations, respectively.

associated with increasing rotational excitation of the CO monomer, characterized by the $j_2$ quantum number. The rotational energies of the CO molecule, estimated within the rigid rotor approximation using the rotational constant $B_{\mathrm{CO}} = 1.9$ cm$^{-1}$, are 3.8, 11.4, and 22.8 cm$^{-1}$ for $j_2 = 1, 2$, and 3, respectively. The energies of the leftmost resonances in the rows of Figure 6.5, given relative to the energy of the first resonance above $D_{0,para}$, are boldfaced in the third column of Table 6.2. These energies coincide with the rigid rotor energies of CO. These resonances also exhibit long lifetimes. Thus, similarly to the case of $H_2He^+$, detailed in Section 5.5.3, for the $H_2$·CO complex opening of new dissociation channels can also be related to the rotational excitation of one of the monomers, here the CO molecule.

Resonance states above the dissociation energy of a given channel characterized by $j_2$, shown within the rows of Figure 6.5, feature an increasing number of nodes in the $R$ coordinate. These nodes, as in the case of the $H_2He^+$ molecular ion, refer to increasing relative kinetic energy of the monomers, which manifests in smaller- and smaller-wavelength continuum waves describing the asymptotic parts of the resonance wave functions along the $R$ coordinate. The resonance states corresponding to a given dissociation channel (a given row of Figure 6.5) can be labeled with the $n$ sequential "quantum number" starting from zero for each new $j_2$ state. The fourth and fifth columns of Table 6.2 reveal that the energies of the resonances, labeled with $n = 1, 2$ and 3 corresponding to a given $j_2$ quantum number, increases approximately with 0.8,

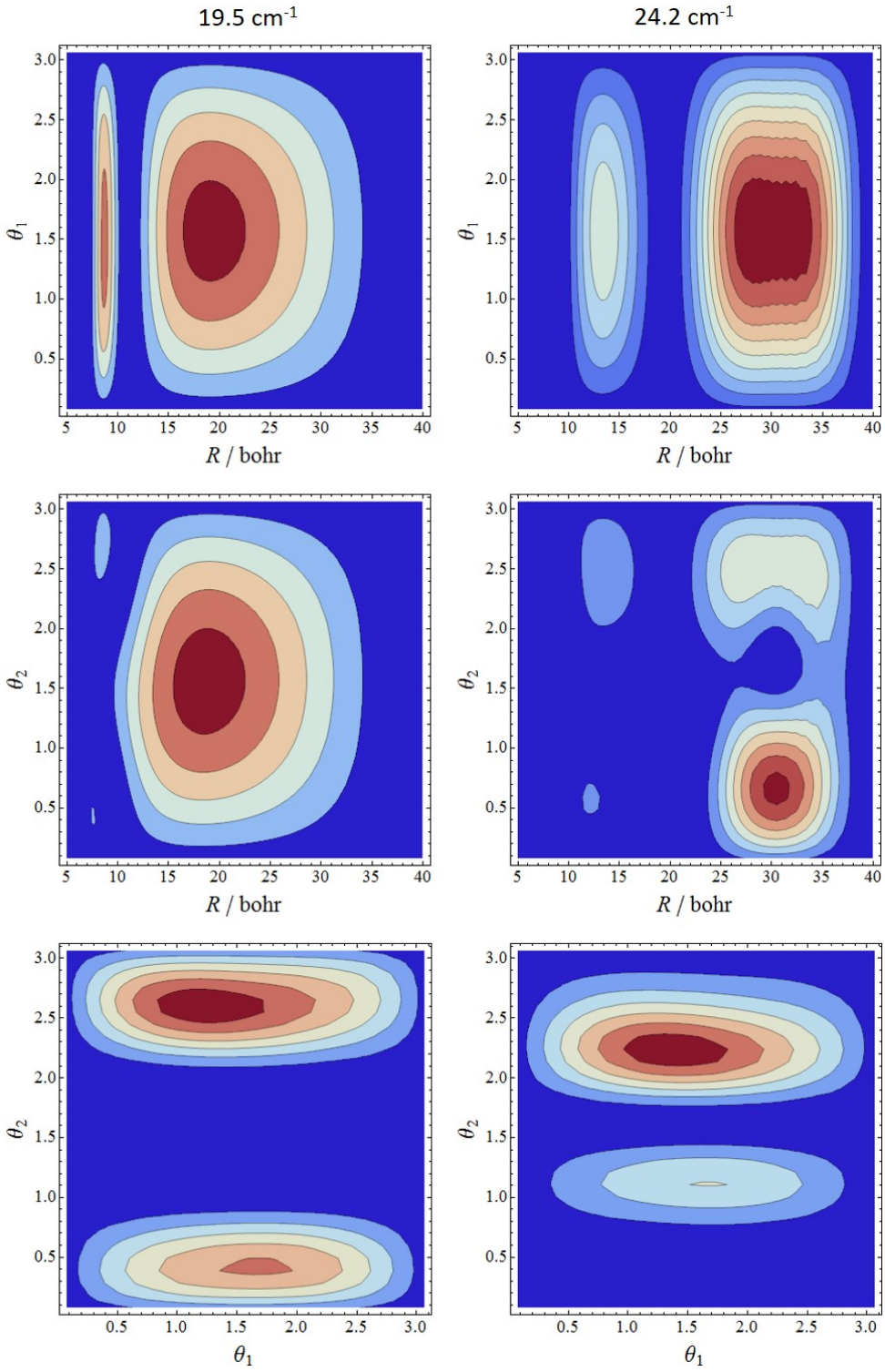


Figure 6.4: 2D GENIUSH-CAP wave function plots (the other coordinates are held fixed at their equilibrium values), depicting the square of the absolute value of the complex resonance eigenvectors, of two selected resonance states of the $H_2$·CO complex, with resonance energies 19.5 and 24.2 $cm^{-1}$. The CAP is switched on between 35-40 bohr along the $R$ dissociation coordinate. The $R$ coordinate is given in bohr, $\theta_1$ and $\theta_2$ are given in radian.

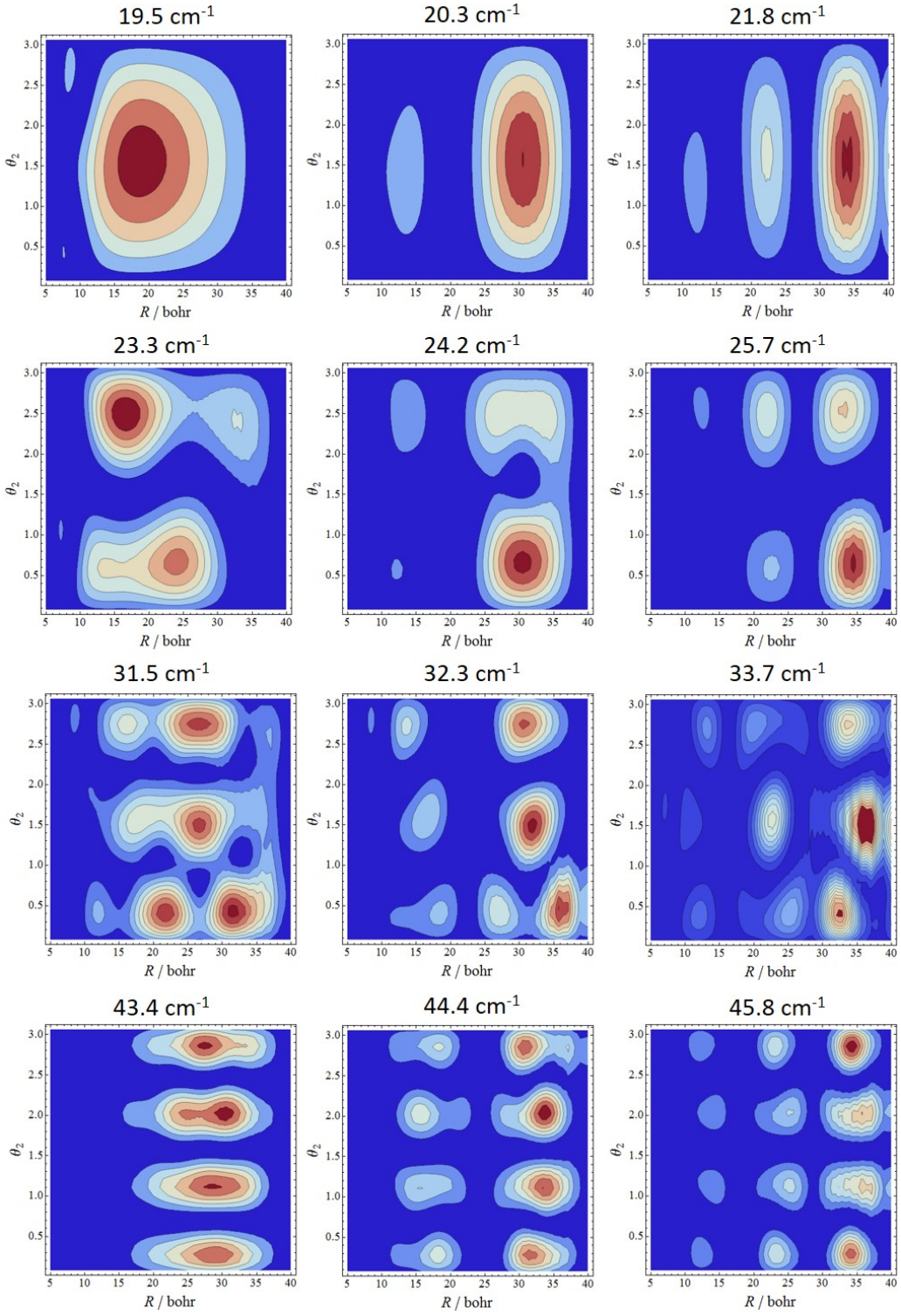


Figure 6.5: 2D $R-\theta_2$ GENIUSH-CAP wave function plots (the other coordinates are held fixed at their equilibrium values), depicting the square of the absolute value of the complex resonance eigenvectors, of 12 selected resonance states of the $H_2$·CO complex, with resonance energies 19.5, 20.3, 21.8, 23.3, 24.2, 25.7, 31.5, 32.3, 33.7, 43.4, 44.4 and 45.8 $cm^{-1}$. The CAP is switched on between 35-40 bohr along the $R$ dissociation coordinate. The $R$ coordinate is given in bohr, $\theta_2$ is given in radian.

2.4 and 4.5 $cm^{-1}$ relative to the energy of the $n = 0, j_2$ state, respectively. Table 6.2 also shows that the lifetimes of the resonance states decrease with increasing $n$, in line with the delocalization of their wave functions along $R$.

## 6.5 Vibrational resonances of *ortho*-$H_2$·CO

Table 6.3: Resonance energies ($cm^{-1}$) and lifetimes (ps) computed for *ortho*-$H_2$·CO with GENIUSH-CAP in the range of $[D_{0,ortho}, 150]$ $cm^{-1}$ having an imaginary part greater than $-1.0$ $cm^{-1}$.

| $Re(E_{res})$ | lifetime | $Re(E_{res})$ | lifetime |
|---|---|---|---|
| 136.2 | 4128 | 139.3 | 86 |
| 136.9[a] | 3877 | 139.8 | 77 |
| 137.0 | 3663 | 140.7 | 25 |
| 137.5 | 300 | 141.1 | 45 |
| 137.7 | 224 | 141.2 | 52 |
| 137.9 | 38 | 141.9 | 37 |
| 137.9 | 190 | 143.7 | 29 |
| 138.6 | 125 | 143.8 | 44 |
| 139.2 | 82 | 144.6 | 678 |

[a]This resonance state was also reported in Ref. 6

I have also found several resonance states in the $[D_{0,ortho} - 150]$ $cm^{-1}$ energy interval, they are listed in Table 6.3. Just above the $D_{0,ortho}$ threshold, between $136 - 137$ $cm^{-1}$, three very long-lived resonance states were identified (see Table 6.3). The corresponding three resonance wave functions are presented in Figure 6.6. Interestingly, these wave-function plots suggest that all three of these resonance states correspond to the *ortho*-$H_2$·CO complex, where both the $H_2$ and the CO moieties are in their first rotationally excited states, *i.e.*, $j_1 = 1$ and $j_2 = 1$, respectively.

However, $j_1$ and $j_2$ are only approximate quantum numbers, and this is why these states split according to the $m_1$ and $m_2$ quantum numbers, which are related to the projection of $\hat{j}_1$ and $\hat{j}_2$ onto the intermolecular axis connecting the centers of masses of the $H_2$ and CO units. Hence, $m_1$ and $m_2$ quantum numbers are also related to excitations along $\theta_1$ and $\theta_2$, respectively. However, due to the $J = 0$ constraint not all the $3 \times 3 = 9$ possible combinations of $m_1$ and $m_2$ can be seen in our computations. The following combinations are feasible (the signs are not assigned): $m_1 = \pm 1$ with

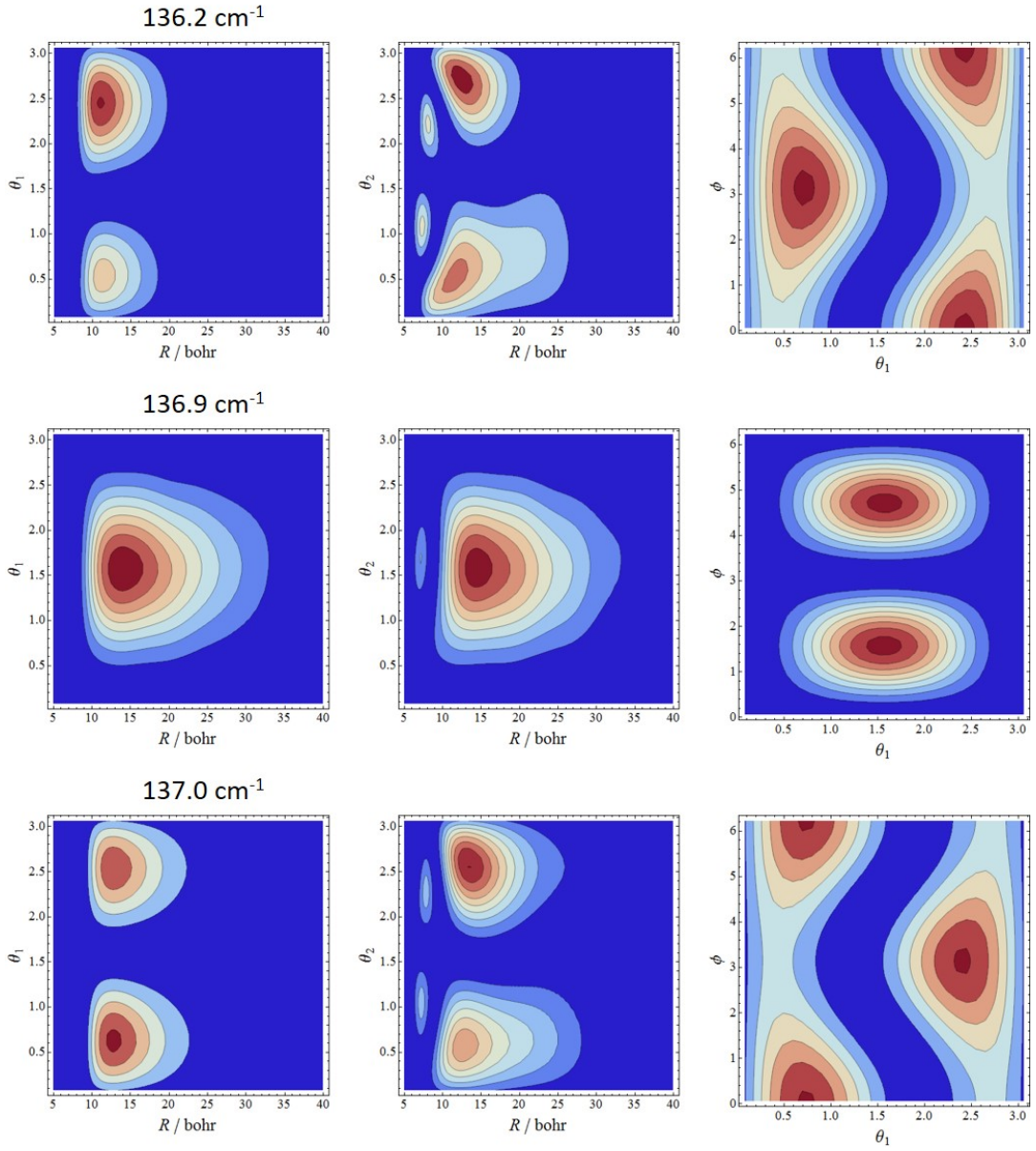


Figure 6.6: Selected 2D cuts of the GENIUSH-CAP wave function plots (the other coordinates are held fixed at their equilibrium values), depicting the square of the absolute value of the complex resonance eigenvectors, of the three longest-lived resonance states of $H_2$·CO above $D_{0,ortho}$, with resonance energies 136.2, 136.9 and 137.0 $cm^{-1}$. The CAP is switched on between 35-40 bohr along the $R$ dissociation coordinate. The $R$ coordinate is given in bohr, $\theta_1, \theta_2$ and $\phi$ are given in radian

$m_2 = \mp 1$, $m_1 = m_2 = 0$, and $m_1 = \mp 1$ with $m_2 = \pm 1$. The first three long-lived *ortho*-$H_2$·CO resonances, presented in Table 6.3, most probably belong to these three types of combinations of $m_1$ and $m_2$.

The *ortho*-$H_2$·CO resonance state corresponding to the opening of the $j_2 = 2$ channel, where the rotational motion of CO is doubly excited, at 144.6 $cm^{-1}$ could also be

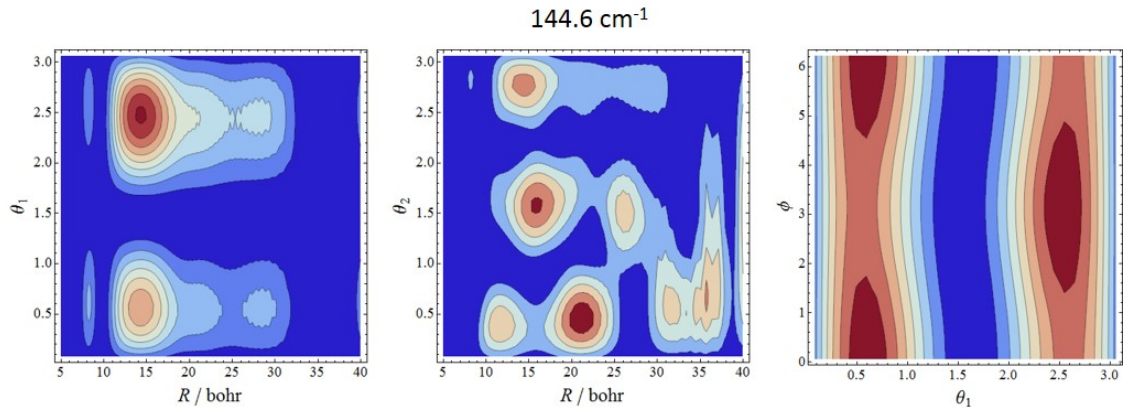


Figure 6.7: 2D GENIUSH-CAP wave function plots (the other coordinates are held fixed at their equilibrium values), depicting the square of the absolute value of the complex resonance eigenvector, of the *ortho*-$H_2$·CO resonance state with energy 144.6 $cm^{-1}$ (relative to the zero-point energy of *para*-$H_2$·CO). The CAP is switched on between 35-40 bohr along the $R$ dissociation coordinate. The $R$ coordinate is given in bohr, $\theta_1, \theta_2$ and $\phi$ are given in radian.

identified with a long lifetime; the corresponding resonance wave function is presented in Figure 6.7. These wave function plots show considerable delocalization along the dissociation coordinate along with a clear double excitation along the $\theta_2$ coordinate.

## 6.6 Concluding remarks

Using the newly-developed GENIUSH-CAP code, I have determined several resonance states of the weakly-bound $H_2$·CO complex, which are the first resonances of a four-atomic system determined by using a variational non-Hermitian technique. In our computations a reduced-dimensional model was employed describing the intermonomer motions. The bound states of *ortho*-$H_2$·CO could be identified as extremely long-lived resonance states well above the first dissociation limit corresponding to *para*-$H_2$·CO. This identification is supported by the good agreement between the energy differences extracted from the experimental IR spectrum of $H_2$·CO and the energy differences of the long-lived resonance states computed with GENIUSH-CAP. The analysis of the corresponding resonance wave functions also strengthened the identification.

Furthermore, I have identified numerous resonance states of the *para*-$H_2$·CO complex and assigned them, based on the analysis of their resonance wave function plots, to

different dissociation channels corresponding to rotational excitations of CO. Numerous resonances of *ortho*-$H_2$·CO were also found. The three lowest-lying *ortho*-$H_2$·CO resonances seem to correspond to rotational excitations of the monomers.

# Chapter 7

# Summary and conclusions

During my PhD years I have developed a general code based on the variational principle for computing rovibrational resonance states of polyatomic molecules. I applied the new code successfully for the Ar·$NO^+$, $H_2He^+$, and $H_2$·CO weakly-bound complexes.

I have linked the non-Hermitian complex absorbing potential (CAP) technique, a popular method used to determine resonance states, to GENIUSH, an in-house, general quasi-variational program capable of computing bound rovibrational states of polyatomic molecules. The new resonance-computing code is named GENIUSH-CAP. Besides having an effective implementation, GENIUSH-CAP also exploits all the advantages of GENIUSH, which are as follows: the possibility of using an arbitrary, suitably defined internal coordinate system, reduced-dimensional models, which can be defined with relative ease, and treating, in principle, arbitrary-sized molecules. The GENIUSH-CAP code has been tested and validated by comparing its results, *i.e.*, resonance energies and lifetimes, with those obtained from the triatomic $D^2$FOPI-CCS code, also developed in our group, using the $H_2He^+$ molecule as a test system. Resonance energies always agreed within a few 0.1 $cm^{-1}$, while lifetimes were always computed in the same order of magnitude by the two different methods, confirming the correctness of the implementation of GENIUSH-CAP.

After augmenting the GENIUSH-CAP and $D^2$FOPI-CCS results with those obtained from stabilization computations, I have identified several dissociation channels

of the $H_2He^+$ molecular ion corresponding to different rotational excitations of the $H_2^+$ diatom. Isolated resonances of $H_2He^+$, forming due to the strong coupling between the intermonomer bending and intramonomer stretching motions, have also been found. Resonance wave function plots, obtained from GENIUSH-CAP computations, provided essential information employed during this analysis.

I have employed GENIUSH-CAP, along with the stabilization method, to explore the resonance states of the Ar·$NO^+$ complex. Stabilization computations revealed an interesting repetitive pattern of resonance states of Ar·$NO^+$ at energies much above the first dissociation threshold of the complex. It turned out that the resonance states forming this pattern are long-lived Feshbach-resonances, in which the complete set of intermonomer stretching and bending motions are recognizable for each vibrational excitation of the $NO^+$ moiety. Furthermore, GENIUSH-CAP results were compared to those of close-coupling scattering computations for the low-lying vibrational resonances of Ar·$NO^+$. The two fundamentally different methods provide resonance energies and lifetimes in good agreement. To the best of my knowledge, a detailed comparison of the two techniques, apart from our work, has not been reported in the literature.

A four-atomic system, namely the $H_2$·CO complex, has also been subjected to GENIUSH-CAP computations. Exploiting the possibility of the simple definition of reduced-dimensional models in GENIUSH, 4D computations (fixing the two monomeric stretches) were carried out for $H_2$·CO. Bound vibrational states of *ortho*-$H_2$·CO with energies well above the complex's first dissociation limit have been identified as extremely long-lived resonances. This identification is also supported by the experimental IR spectrum of $H_2$·CO. Furthermore, several resonance states corresponding to both the *para*- and the *ortho*-$H_2$·CO complex have been found and assigned, based on the analysis of their wave functions. Investigation of *para*-$H_2$·CO resonances revealed the opening of dissociation channels corresponding to increasing rotational excitations of the CO monomer. Three long-lived resonances of *ortho*-$H_2$·CO are found to correspond to the rotational excitations of the two monomers. To the best of my knowledge, these are the first variational resonances, determined with a non-Hermitian quantum chemical method, of a system containing more than three atoms.

In summary, I have developed a general code, called GENIUSH-CAP, capable of

determining resonance states of arbitrary-sized semirigid and flexible molecules. Employing the new GENIUSH-CAP program, complemented with stabilization and complex coordinate scaling computations, revealed interesting features of weakly-bound molecular complexes slightly and also well above their first dissociation thresholds. The results obtained augment significantly our qualitative understanding of the dynamical behavior of van der Waals systems of fundamental chemical importance.

# Chapter 8

# Összefoglalás

Doktori munkám során egy olyan kvantumkémiai programot fejlesztettem ki, amely variációs alapon határozza meg tetszőleges méretű, flexibilis molekulák rezgési-forgási rezonancia állapotait. Az újonnan fejlesztett programot sikeresen alkalmaztam az $Ar{\cdot}NO^+$, a $H_2He^+$, és a $H_2{\cdot}CO$ gyengén kötött molekulakomplexek esetében.

Módszerfejlesztési munkám során hozzáillesztettem a komplex elnyelő potenciál (*complex absorbing potential*, CAP) módszert a csoportunkban kidolgozott, variációs alapú kvantummechanikai GENIUSH programhoz. A GENIUSH egy általános, program, amely félmerev és flexibilis, többatomos molekulák kötött rezgési-forgási állapotainak számítására használható. A CAP módszer hatékony implementációja lehetővé teszi, hogy kihasználjuk a GENIUSH program által kínált összes előnyt: a GENIUSH-ban lehetőség van tetszőleges, a rezgési-forgási probléma leírására legmegfelelőbb koordináta-rendszer alkalmazására, valamint redukált dimenziós modellek is egyszerűen definiálhatók. A GENIUSH-CAP program validálását a $H_2He^+$ teszt rendszer segítségével végeztem el, úgy, hogy a GENIUSH-CAP program segítségével számított rezonancia energiákat és élettartamokat összehasonlítottam a háromatomos molekulák kezelésére alkalmas, komplex koordináta skálázást (*complex coordinate scaling*, CCS) alkalmazó, a csoportunkban kifejlesztett $D^2$FOPI-CCS programmal számított rezonancia energiákkal és élettartamokkal. A két különböző programmal számított rezonancia energiák általában néhány tized $cm^{-1}$-en belül egyeztek meg, míg a rezonancia állapotok számított élettartama mindig ugyanabba a nagyságrendbe esett.

A GENIUSH-CAP számításokat az ún. stabilizációs módszerrel és a $D^2$FOPI-CCS programmal számított eredményekkel kiegészítve a $H_2He^+$ molekulaion esetében több, a $H_2^+$ monomer forgási gerjesztéseihez tartozó disszociációs csatorna létezésére mutattam rá. Továbbá számos, a molekula belső mozgásainak erős csatolódásából adódó rezonancia állapotot is sikerült azonosítanom. A kvalitatív elemzések alapjául a GENIUSH-CAP segítségével előállított rezonancia hullámfüggvények szolgáltak.

A GENIUSH-CAP program és a stabilizációs módszer segítségével az $Ar{\cdot}NO^+$ komplex rezonancia állapotait is vizsgáltam. A stabilizációs számítások az $Ar{\cdot}NO^+$ rezonancia állapotainak egy érdekes, jóval az első disszociációs energia felett is ismétlődő szerkezetére mutattak rá. Ezt a szerkezetet hosszú élettartamú Feshbach rezonanciák alkotják: az $NO^+$ monomer rezgésileg gerjesztett állapotaira rakódó, az intermonomer mozgások gerjesztéseihez tartozó állapotok. A GENIUSH-CAP eredményeket szórási számításokkal is összehasonlítottam az első disszociációs határhoz közeli rezgési rezonanciák esetében. A két alapvetően különböző módszerből nyert rezonancia energiák és élettartamok jó egyezést mutattak. Ilyen jellegű összehasonlítást, a mi munkánkon kívül, még nem publikáltak az irodalomban.

Végül egy négyatomos rendszer, a $H_2{\cdot}CO$ molekulakomplex rezonancia állapotait is vizsgáltam a GENIUSH-CAP módszer segítségével. Ez esetben az *orto*-$H_2{\cdot}CO$ komplex kötött állapotait hosszú élettartamú rezonancia állapotokként sikerült azonosítanom, jóval az első, a *para*-$H_2{\cdot}CO$-hoz tartozó disszociációs határ felett. Ezt az asszignációt a $H_2{\cdot}CO$ komplex kísérleti infravörös színképéből nyert információk is megerősítik. Számos további rezonancia állapotot azonosítottam mind az *orto*-, mind a *para*-$H_2{\cdot}CO$ komplex esetében. A *para*-$H_2{\cdot}CO$ komplex első disszociációs energiája felett több disszociációs csatornát is találtam, amelyek a CO monomer különböző forgási gerjesztéseihez tartoznak. Három hosszú élettartamú *ortho*-$H_2{\cdot}CO$ rezonanciát is a monomerek forgási gerjesztéseihez tudtam rendelni. Tudomásom szerint a $H_2{\cdot}CO$ komplex az első négyatomos rendszer, amelynek a rezonancia állapotait nem-Hermitikus, variációs alapú módszerekkel sikerült azonosítani.

Doktori munkám fő eredménye a GENIUSH-CAP program kifejlesztése, amely egy általános variációs kód többatomos, félmerev és flexibilis molekulák rezgési-forgási rezonancia állapotainak meghatározására. A GENIUSH-CAP program, valamint a

stabilizációs és a komplex koordináta skálázás módszerek segítségével gyengén kötött molekulakomplexek számos érdekes tulajdonságára mutattam rá a disszociációs határ felett. Ezek az új ismeretek nagyban hozzájárulnak e kémiai szempontból alapvető fontosságú molekuláris rendszerek viselkedésének mélyebb megértéséhez.

# Bibliography


[1] N. Moiseyev. In Non-Hermitian Quantum Mechanics. Cambridge University Press, 2011.

[2] A. Carrington, I. R. Mcnab, and Y. D. West. J. Chem. Phys., 98(2):1073–1092, 1993.

[3] M. Grechko, P. Maksyutenko, T. R. Rizzo, and O. V. Boyarkin. J. Chem. Phys., 133:8, 2010.

[4] N. F. Zobov, S. V. Shirin, L. Lodi, B. C. Silva, J. Tennyson, A. G. Császár, and O. L. Polyansky. Chem. Phys. Lett., 507(1-3):48–51, 2011.

[5] T. Szidarovszky and A. G. Császár. Mol. Phys., 111(14-15, SI):2131–2146, 2013.

[6] P. Jankowski, A. R. W. McKellar, and K. Szalewicz. Science, 336(6085):1147–1150, 2012.

[7] P. Courteille, R. S. Freeland, D. J. Heinzen, F. A. Van Abeelen, and B. J. Verhaar. Phys. Rev. Lett., 81(1):69, 1998.

[8] M. Theis, G. Thalhammer, K. Winkler, M. Hellwig, G. Ruff, R. Grimm, and J. Hecker Denschlag. Phys. Rev. Lett., 93(12):123001, 2004.

[9] S. Knoop, F. Ferlaino, M. Mark, M. Berninger, H. Schöbel, H.-C. Nägerl, and R. Grimm. Nature Phys., 5(3):227–230, 2009.

[10] S. Chefdeville, T. Stoecklin, A. Bergeat, K. M. Hickson, C. Naulin, and M. Costes. Phys. Rev. Lett., 109:2, 2012.

[11] S. Chefdeville, T. Stoecklin, C. Naulin, P. Jankowski, K. Szalewicz, A. Faure, M. Costes, and A. Bergeat. Astrophys. J. Lett., 799(1):L9, 2015.

[12] B. Yang, N. Balakrishnan, P. Zhang, X. Wang, J. M. Bowman, R. C. Forrey, and P. C. Stancil. J. Chem. Phys., 145:3, 2016.

[13] W. Shiu, J. J. Lin, and K. P. Liu. Phys. Rev. Lett., 92:10, 2004.

[14] Q. Wang, Z. T. Cai, and D. C. Feng. J. Mol. Struct. Theochem, 759(1-3):31–34, 2006.

[15] B. L. Zhang and K. P. Liu. J. Chem. Phys., 122:10, 2005.

[16] R. Otto, J. Ma, A. W. Ray, J. S. Daluz, J. Li, H. Guo, and R. E. Continetti. Science, 343(6169):396–399, 2014.

[17] T. Yang, J. Chen, L. Huang, T. Wang, C. Xiao, Z. Sun, D. Dai, X. Yang, and D. H. Zhang. Science, 347(6217):60–63, 2015.

[18] A. Klein, Y. Shagam, W. Skomorowski, P. S. Zuchowski, M. Pawlak, M. C. Janssen, N. Moiseyev, S. Y. T. van de Meerakker, A. van der Avoird, C. P. Koch, and E. Narevicius. Nature Phys., 2016.

[19] D. Papp, Szidarovszky T., and A. G. Császár. accepted for publication, 2017.

[20] E. Mátyus, G. Czakó, and A. G. Császár. J. Chem. Phys., 130:134112, 2009.

[21] C. Fábri, E. Mátyus, and A. G. Császár. J. Chem. Phys., 134:074105, 2011.

[22] D. Papp, J. Sarka, T. Szidarovszky, A. G. Császár, E. Mátyus, M. Hochlaf, and T. Stoecklin. Phys. Chem. Chem. Phys., 19(12):8123–8622, 2017.

[23] D. Papp, A. G. Császár, K. Yamanouchi, and Szidarovszky T. manuscript in preparation, 2017.

[24] D. Papp, P. Rovó, I. Jákli, A. G. Császár, and A. Perczel. J. Comp. Chem., 2017.

[25] M. Born and R. Oppenheimer. Annalen der Physik, 389(20):457–484, 1927.

[26] R.-F. Lu, P.-Y. Zhang, and K.-L. Han. Phys. Rev. E, 77(6):066701, 2008.

[27] I. Goychuk and P. Hänggi. Adv. Phys., 54(6-7):525–584, 2005.

[28] J. S. Prauzner-Bechcicki, K. Sacha, B. Eckhardt, and J. Zakrzewski. Phys. Rev. Lett., 98(20):203002, 2007.

[29] T. Szidarovszky and K. Yamanouchi. Phys. Rev. A, 94:6, 2016.

[30] T. Szidarovszky and K. Yamanouchi. Molecular Physics, pages 1–11, 2017.

[31] D. H. Zhang and J. Z. H. Zhang. J. Chem. Phys., 101(5):3671–3678, 1994.

[32] N. Balakrishnan, C. Kalyanaraman, and N. Sathyamurthy. Phys. Rep., 280(2):79–144, 1997.

[33] D. Neuhauser, M. Baer, R. S. Judson, and D. J. Kouri. Comp. Phys. Comm., 63(1-3):460–481, 1991.

[34] G. G. Balint-Kurti, F. Gögtas, S. P. Mort, A. R. Offer, A. Laganà, and O. Gervasi. J. Chem. Phys., 99(12):9567–9584, 1993.

[35] M. H. Beck, A. Jäckle, G. A. Worth, and H.-D. Meyer. Phys. Rep., 324(1):1–105, 2000.

[36] D. H. Zhang and J. Z. H. Zhang. J. Chem. Phys., 101(2):1146–1156, 1994.

[37] M. Yang, S.-Y. Lee, and D. H. Zhang. J. Chem. Phys., 126(6):064303, 2007.

[38] S. Y. Lin, H. Guo, P. Honvault, and D. Xie. J. Chem. Phys. B, 110(47):23641–23643, 2006.

[39] F. A. de Saavedra, E. Buendıa, F. J. Gálvez, and A. Sarsa. Eur. Phys. J. D, 13(2):201–206, 2001.

[40] M. M. Cassar and G. W. F. Drake. J. Phys. B, 37(12):2485, 2004.

[41] L. Wolniewicz. Canadian J. Phys., 54(6):672–679, 1976.

[42] M. Stanke, D. Kędziera, M. Molski, S. Bubin, M. Barysz, and L. Adamowicz. Phys. Rev. Lett., 96(23):233002, 2006.

[43] M. Cafiero and L. Adamowicz. Chem. Phys. Lett., 387(1):136–141, 2004.

[44] H. H. Nielsen. Rev. Modern Phys., 23(2):90, 1951.

[45] I. M Mills. Mol. Spectr.: modern research, 1:115, 1972.

[46] B. T. Sutcliffe and J. Tennyson. Int. J. Quant. Chem., 39(2):183–196, 1991.

[47] R. N. Zare. Angular momentum: Understanding spatial aspects in physics and chemistry. Wiley, New York, 1988.

[48] C.G.J. Jacobi. C. R. Hebd. Seances Acad. Sci., 15:236–255, 1842.

[49] R. Radau. Sur une transformation des équations différentielles de la dynamique. 1868.

[50] E. A. Hylleraas. Zeitschrift für Physik A Hadrons and Nuclei, 54(5):347–366, 1929.

[51] C. L. Pekeris. Phys. Rev., 112(5):1649, 1958.

[52] A. G. Császár and N. C. Handy. Mol. Phys., 86(5):959–979, 1995.

[53] A. G. Császár and N. C. Handy. J. Chem. Phys., 102(10):3962–3967, 1995.

[54] C. Lanczos. Applied analysis. Courier Corporation, 1988.

[55] D. O. Harris, G. G Engerholm, and W. D. Gwinn. J. Chem. Phys., 43(5):1515–1517, 1965.

[56] A. S. Dickinson and P. R. Certain. J. Chem. Phys., 49(9):4209–4211, 1968.

[57] J. C. Light and T. Carrington. Adv. Chem. Phys., 114:263–310, 2000.

[58] V. Szalay. J. Chem. Phys., 99(3):1978–1984, 1993.

[59] V. Szalay, G Czakó, A. Nagy, T. Furtenbacher, and A. G. Császár. J. Chem. Phys., 119(20):10512–10518, 2003.

[60] C. Lanczos. An iteration method for the solution of the eigenvalue problem of linear differential and integral operators. United States Governm. Press Office Los Angeles, CA, 1950.

[61] E. R. Davidson. J. Comp. Phys., 17(1):87–94, 1975.

[62] J. R. Taylor. Scattering theory: the quantum theory of nonrelativistic collisions. Courier Corporation, 2012.

[63] J. Tennyson and B. T. Sutcliffe. J. Chem. Phys., 77(8):4061–4072, 1982.

[64] M. H. Alexander and D. E. Manolopoulos. J. Chem. Phys., 86(4):2044–2050, 1987.

[65] A. T. Stelbovics. Phys. Rev. A, 41(5):2536, 1990.

[66] I. Bray and A. T. Stelbovics. Phys. Rev. A, 46(11):6995, 1992.

[67] J. M. Bowman, S. Carter, and X. Huang. Int. Rev. Phys. Chem., 22(3):533–549, 2003.

[68] E. Mátyus, G. Czakó, B. T. Sutcliffe, and A. G. Császár. J. Chem. Phys., 127(8):084102, 2007.

[69] J. Tennyson, J. R. Henderson, and N. G. Fulton. Comp. Phys. Comm., 86(1-2):175–198, 1995.

[70] J. Tennyson, M. A. Kostin, P. Barletta, G. J. Harris, O. L. Polyansky, J. Ramanlal, and N. F. Zobov. Comp. Phys. Comm., 163(2):85–116, 2004.

[71] G. Czakó, T. Furtenbacher, A. G. Császár, and V. Szalay. Mol. Phys., 102(23-24):2411–2423, 2004.

[72] T. Szidarovszky, A. G. Császár, and G. Czakó. Phys. Chem. Chem. Phys., 12(29):8373–8386, 2010.

[73] M. J. Bramley and T. Carrington. J. Chem. Phys., 99(11):8519–8541, 1993.

[74] M. Mladenović. J. Chem. Phys., 112(3):1070–1081, 2000.

[75] I. N. Kozin, M. M. Law, J. Tennyson, and J. M. Hutson. Comp. Phys. Comm., 163(2):117–131, 2004.

[76] H.-G. Yu. J. Mol. Spectr., 256(2):287–298, 2009.

[77] H.-G. Yu and J. T. Muckerman. J. Mol. Spectr., 214(1):11–20, 2002.

[78] B. Fehrensen, D. Luckhaus, and M. Quack. Zeitschrift für Physikalische Chemie, 209(1):1–19, 1999.

[79] B. Fehrensen, D. Luckhaus, and M. Quack. Chem. Phys. Lett., 300(3):312–320, 1999.

[80] D. Luckhaus. J. Chem. Phys., 113(4):1329–1347, 2000.

[81] D. Luckhaus. J. Chem. Phys., 118(19):8797–8806, 2003.

[82] D. Lauvergnat and A. Nauts. J. Chem. Phys., 116(19):8560–8570, 2002.

[83] D. Lauvergnat, E. Baloïtcha, G. Dive, and M. Desouter-Lecomte. Chem. Phys., 326(2):500–508, 2006.

[84] S. N. Yurchenko, W. Thiel, and P. Jensen. J. Mol. Spectr., 245(2):126–140, 2007.

[85] J. Makarewicz, P. Jensen, and P. R. Bunker, 2000.

[86] C. Fábri, E. Mátyus, and A. G. Császár. Spectrochim. Acta A, 119:84–89, 2014.

[87] B. Podolsky. Phys. Rev., 32(5):812, 1928.

[88] G. Gamow. Nature, 122:805–806, 1928.

[89] J. D. Tobiason, J. R. Dunlop, and E. A. Rohlfing. J. Chem. Phys., 103(4):1448–1469, 1995.

[90] S. A. Reid and H. Reisler. J. Phys. Chem., 100(2):474–487, 1996.

[91] H. Zhang and S. C. Smith. Phys. Chem. Comm., 6:12–20, 2003.

[92] E. F. Vandishoeck, M. C. Vanhemert, A. C. Allison, and A. Dalgarno. J. Chem. Phys., 81(12):5709–5724, 1984.

[93] L. Zhu, K. Suto, J. Fiss, R. Wada, T. Seideman, and R. J. Gordon. Phys. Rev. Lett., 79(21):4108–4111, 1997.

[94] A. L. Sobolewski and W. Domcke. J. Chem. Phys., 86(1):176–187, 1987.

[95] F. Meng, W. Yan, and D. Wang. Phys. Chem. Chem. Phys., 14(39):13656–13662, 2012.

[96] V. A. Mandelshtam, T. R. Ravuri, and H. S. Taylor. Phys. Rev. Lett., 70(13):1932–1935, 1993.

[97] V. Ryaboy and N. Moiseyev. J. Chem. Phys., 103(10):4061–4068, 1995.

[98] H. Y. Mussa and J. Tennyson. Chem. Phys. Lett., 366:449–457, 2002.

[99] L. D. Landau and E. M. Lifshitz. Quantum Mechanics. Pergamon Press, 1965.

[100] N. Moiseyev. Phys. Rep., 302(5):212–293, 1998.

[101] F. T. Smith. Phys. Rev., 118:349–356, 1960.

[102] U. Fano. Phys. Rev., 124(6):1866, 1961.

[103] U. V. Riss and H. D. Meyer. J. Phys. B, 26(23):4503–4536, 1993.

[104] J. G. Muga, J. P. Palao, B. Navarro, and I. L. Egusquiza. Phys. Rep. Rev. section of Phys. Lett., 395(6):357–426, 2004.

[105] S. Skokov, J. M. Bowman, and V. A. Mandelshtam. Phys. Chem. Chem. Phys., 1(6):1279–1282, 1999.

[106] N. Rom, N. Lipkin, and N. Moiseyev. Chem. Phys., 151(2):199–204, 1991.

[107] A. U. Hazi and H. S. Taylor. Phys. Rev. A, 1(4):1109–1120, 1970.

[108] J. Müller, X. Z. Yang, and J. Burgdorfer. Phys. Rev. A, 49(4):2470–2475, 1994.

[109] E. Mátyus, C. Fábri, T. Szidarovszky, Gábor Czakó, Wesley D. Allen, and A. G. Császár. J. Chem. Phys., 133:034113, 2010.

[110] http://math.nist.gov/lapack++/.

[111] B. Poirier and T. Carrington. J. Chem. Phys., 118(1):17–28, 2003.

[112] U. V. Riss and H. D. Meyer. J. Phys. B, 31(10):2279–2304, 1998.

[113] N. Halberstadt and K. C. Janda, editors. Dynamics of polyatomic van der Waals complexes, volume 227 of NATO ASI Series B. Plenum, New York, 1990.

[114] M. C. Heaven. Annu. Rev. Phys. Chem., 43:283, 1992.

[115] A. Rohrbacher, N. Halberstadt, and K. C. Janda. Ann. Rev. Phys. Chem., 51:405, 2000.

[116] D. S. Boucher and R. A. Loomis. Adv. Chem. Phys., 138:375, 2008.

[117] J. A. Beswick, N. Halberstadt, and K. C. Janda. Chem. Phys., 399:4, 2012.

[118] Goulven Q. and Paul S. J. Chem. Rev., 112(9):4949–5011, 2012.

[119] M. L. Dubernet, M. H. Alexander, Y. A. Ba, N. Balakrishnan, C. Balança, C. Ceccarelli, J. Cernicharo, F. Daniel, F. Dayou, M. Doronin, et al. Astron. Astrophys., 553:50, 2013.

[120] M. J. Barlow. Science, 342:1343, 2013.

[121] R. A. Theis, W. J. Morgan, and R. C. Fortenberry. Mon. Not. R. Astron. Soc., 446:195, 2015.

[122] H.-J. Werner, B. Follmeg, M. H. Alexander, and D. Lemoine. J. Chem. Phys., 91:5425, 1989.

[123] A. Bergeat, J. Onvlee, C. Naulin, A. van der Avoird, and M. Costes. Nature Chem., 7:349, 2015.

[124] J. Tennyson and B. T. Sutcliffe. J. Chem. Phys., 79:43, 1983.

[125] J. Tennyson and B. T. Sutcliffe. J. Chem. Phys., 77:4061, 1982.

[126] P. R. R. Langridge-Smith, E. M. Carrasquillo, and D. H. Levy. J. Chem. Phys., 74:6513, 1981.

[127] P. D. A. Mills, C. M. Western, and B. J. Howard. J. Phys. Chem., 90:3331, 1986.

[128] O. L. A. Monti, H. A. Cruse, T. P. Softley, and S. R. Mackenzie. Chem. Phys. Lett., 333:146, 2001.

[129] R. Prosmiti, P. Villarreal, and G. Delgado-Barrio. Chem. Phys. Lett., 359:473, 2002.

[130] A. Valdés, R. Prosmiti, P. Villarreal, G. Delgado-Barrio, D. Lemoine, and B. Lepetit. J. Chem. Phys., 126:244314, 2007.

[131] R. Prosmiti, C. Cunha, P. Villarreal, and G. Delgado-Barrio. J. Chem. Phys., 119:4216, 2003.

[132] W. D. Rellergert, S. T. Sullivan, S. J. Schowalter, S. Kotogichova, K. Chen, and E. R. Hudson. Nature, 495:490–494, 2013.

[133] T. Stoecklin, P. Halvick, M. A. Gannaouni, M. Hochlaf, S. Kotochigova, and E. R. Hudson. Nat. Comm., 7:11234, 2016.

[134] M. Takahashi. J. Chem. Phys., 96:2594–2599, 1992.

[135] J.-M. Robbe, M. Bencheikh, and J.-P. Flament. Chem. Phys. Lett., 210:170, 1993.

[136] K. Sato, Y. Achiba, and K. Kimura. J. Chem. Phys., 81:57, 1984.

[137] T. G. Wright, V. Špirko, and P. Hobza. J. Chem. Phys., 100:5403, 1994.

[138] I. Fourré and M. Raoult. Chem. Phys., 199:215, 1995.

[139] T. G. Wright. J. Chem. Phys., 105:7579, 1996.

[140] A. M. Bush, T. G. Wright, V. Špirko, and M. Juřek. J. Chem. Phys., 106:4531, 1997.

[141] A. M. Bush, J. M. Dyke, P. Mack, D. M. Smith, and T. G. Wright. J. Chem. Phys., 108:406, 1998.

[142] J. D. Barr, J. M. Dyke, P. Mack, D. M. Smith, and T. G. Wright. J. Electron Spectrosc. Relat. Phenom., 97:159, 1998.

[143] M. C. R. Cockett, K. Müller-Dethlefs, and T. G. Wright. Annu. Rep. Prog. Chem., Sect. C: Phys. Chem., 94:327, 1998.

[144] E. P. F. Lee, P. Soldán, and T. G. Wright. J. Phys. Chem. A, 102:6858, 1998.

[145] P. Halvick, T. Stoecklin, F. Lique, and M. Hochlaf. J. Chem. Phys., 135:044312, 2011.

[146] K. T. Giju, S. Roszak, and J. Leszczynski. J. Chem. Phys., 117:4803, 2002.

[147] T. Ritschel, P. J. Kuntz, and L. Zülicke. Eur. Phys. J. D, 44:93, 2007.

[148] D. T. Anderson, S. Davis, and D. J. Nesbitt. J. Chem. Phys., 107:1115, 1997.

[149] A. G. Császár. WIREs Comput. Mol. Sci., 2:273–289, 2012.

[150] T. Stoecklin, A. Voronin, and J. C. Rayez. Phys. Rev. A, 66(4):042703, 2002.

[151] D. E Manolopoulos. Close-coupling equations the log derivative approach to inelastic scattering, bound states and photofragmentation problems. PhD thesis, University of Cambridge, 1988.

[152] G. Guillon and T. Stoecklin. J. Chem. Phys., 130:144306, 2009.

[153] A. Riera. J. Phys. Chem., 97:1558–1565, 1993.

[154] E. Mátyus. J. Phys. Chem. A, 117:7195, 2013.

[155] J. H. Black. Astrophys. J., 222:125–131, 1978.

[156] W. Roberge and A. Dalgarno. Astrophys. J., 255:489–496, 1982.

[157] D. R. Flower and E. Roueff. Astronomy and Astrophysics, 72:361–366, 1979.

[158] T. Abel, P. Anninos, M. L. Norman, and Y. Zhang. Astrophys. J., 508(2):518, 1998.

[159] E. Herbst. Ann. Rev. Phys. Chem., 46(1):27–54, 1995.

[160] K. M Ferriere. Rev. Modern Phys., 73(4):1031, 2001.

[161] J. Tennyson and S. Miller. J. Chem. Phys., 87(11):6648–6652, 1987.

[162] D. De Fazio. Phys. Chem. Chem. Phys., 16(23):11662–11672, 2014.

[163] S. Bovino, M. Tacconi, and F. A. Gianturco. J. Phys. Chem. A, 115(29):8197–8203, 2011.

[164] D. De Fazio, M. de Castro-Vitores, A. Aguado, V Aquilanti, and S. Cavalli. J. Chem. Phys., 469:26–30, 2012.

[165] http://webbook.nist.gov/cgi/inchi?ID=C12184906&Mask=1000#Dia4.

[166] A. R. W. McKellar. J. Chem. Phys., 108(5):1811–1820, 1998.

[167] P. Jankowski, L. A. Surin, A. Potapov, S. Schlemmer, A. R. W. McKellar, and K. Szalewicz. J. Chem. Phys., 138:8, 2013.

[168] P. Jankowski and K. Szalewicz. J. Chem. Phys., 108(9):3554–3565, 1998.

[169] P. Jankowski and K. Szalewicz. J. Chem. Phys., 123(10):104301, 2005.

[170] B. Yang, P. Zhang, X. Wang, P. C. Stancil, J. M. Bowman, N. Balakrishnan, and R. C. Forrey. Nat. Commun., 6, 2015.

[171] T. Stoecklin, A. Faure, P. Jankowski, S. Chefdeville, A. Bergeat, C. Naulin, S. B. Morales, and M. Costes. Phys. Chem. Chem. Phys., 19(1):189–195, 2017.

[172] K. P. Huber and P. G. Herzberg. Molecular spectra and molecular structure: IV. Constants of diatomic molecules. Van Nostrand Reinhold, New York, 1979.

[173] J. Sarka, C. Fábri, T. Szidarovszky, A. G. Császár, Z. Lin, and A. B. McCoy. Mol. Phys., 113(13-14, SI):1873–1883, 2015.

[174] J. Sarka and A. G. Császár. J. Chem. Phys., 144(15), APR 21 2016.